

**Indirect studies of astrophysical
reaction rates through transfer
reactions**

Stephen Gillespie

Ph.D.

University of York

Physics

September 2016

Abstract

The work in this thesis describes two experiments which use transfer reactions to perform spectroscopic studies of nuclei in order to improve reaction rates in astrophysical environments.

The first experiment is an indirect study of the $^{34}\text{S}(p,\gamma)^{35}\text{Cl}$ reaction rate at energies relevant to classical novae temperatures. By reducing uncertainties in this reaction it may be possible to use $^{32}\text{S}/^{34}\text{S}$ isotopic ratio as a diagnostic tool to determine pre-solar grain paternity. A study of the $^{34}\text{S}(^3\text{He},d)^{35}\text{Cl}$ transfer reaction was performed to identify energy levels in the astrophysically relevant energy region and assign spin and parity to these new states. A new reaction rate has been calculated from this spectroscopic information and is the first experimental measurement of the $^{34}\text{S}(p,\gamma)^{35}\text{Cl}$ reaction rate. Using this new rate it was concluded that it is now possible to determine the paternity of pre-solar grains using the $^{32}\text{S}/^{34}\text{S}$ isotopic ratio.

The second experiment measured two proton transfer reactions, $(^3\text{He},d)$ and (α,t) , with the aim of making spin assignments of states above the neutron threshold in ^{27}Al . Combined with information from complementary experiments this information would be used to calculate new $^{26}\text{Al}(n,p/\alpha)$ reaction rates. Direct comparison of the two transfer reactions should allow for low and high spin states to be identified, however due to lower than expected cross sections useful information could not be extracted from the (α,t) reaction. The experimental resolution was insufficient to resolve individual states with the $(^3\text{He},d)$ reaction, however due to the selectivity of the reaction it appears that many of the previously known states show low spin behaviour and are likely not relevant to the reaction rate at astrophysical temperatures. In addition, the non-observation of 23 states known to exist in ^{27}Al may indicate they are high spin and further measurements of these states should be performed in order to calculate new $^{26}\text{Al}(n,p/\alpha)$ reaction rates.

Contents

Abstract	2
Contents	3
List of Figures	6
List of Tables	9
Acknowledgements	10
Declaration	12
1 Introduction	13
1.1 Astrophysical Sites	13
1.1.1 White Dwarf	14
1.1.2 Wolf-Rayet Star	14
1.1.3 Type II Supernova	15
1.1.4 Binary Systems	16
1.2 Astrophysical Motivation	17
1.2.1 Astrophysical Observables	17
1.2.2 Sensitivity Studies	18
1.2.3 Motivation $^{34}\text{S}(^3\text{He,d})^{35}\text{Cl}$	19
1.2.4 Motivation $^{26}\text{Mg}(^3\text{He,d})^{27}\text{Al}/^{26}\text{Mg}(\alpha,\text{t})^{27}\text{Al}$	21
2 Theory	26
2.1 Nuclear Reactions	26
2.1.1 Centre of Mass Frame	27
2.1.2 Cross Section	28
2.1.3 Direct Reactions	28

2.1.4	Compound Reactions	30
2.2	Reaction Theory	31
2.2.1	DWBA	32
2.2.2	FRESCO	34
2.3	Gamow Window	35
2.4	Thermonuclear Reaction Rates	37
2.4.1	Non-Resonant Reaction Rate	38
2.4.2	Resonant Reaction Rate	39
2.4.3	Statistical Models	42
2.4.4	Reverse Reaction Rate	43
2.4.5	Reaction Rates Involving Excited Nuclei	44
3	Munich Experimental Setup	45
3.1	Beam Production	45
3.2	Experiment Detectors	46
3.2.1	Munich Q3D Magnetic Spectrometer	46
3.2.2	Focal Plane Detectors	50
3.2.3	Particle Identification	53
3.2.4	Focal Plane Calibration	55
3.3	Experimental Details	56
3.3.1	Targets	56
4	$^{34}\text{S}(^3\text{He},\text{d})^{35}\text{Cl}$ Analysis and Results	58
4.1	Focal Plane Identification	58
4.2	Focal Plane Fitting	60
4.2.1	Peak Functions	63
4.2.2	Fitting Procedure	65
4.2.3	Focal Plane Fits	66
4.3	Focal Plane Calibration	72
4.4	Angular Distributions	73
4.4.1	DWBA Calculations	75
4.4.2	$^{32}\text{S}(^3\text{He},\text{d})^{33}\text{Cl}$ Angular Distributions	75
4.4.3	$^{34}\text{S}(^3\text{He},\text{d})^{35}\text{Cl}$ Angular Distributions	79
4.5	Thermonuclear Reaction Rate	82
4.6	Astrophysical Impact of the $^{34}\text{S}(p,\gamma)^{35}\text{Cl}$ Reaction Rate	88
5	$^{34}\text{S}(^3\text{He},\text{d})^{35}\text{Cl}$ Discussion	92

5.1	Discussion of the Spectroscopy of ^{35}Cl	93
5.2	Discussion of the $^{34}\text{S}(p,\gamma)^{35}\text{Cl}$ reaction rate and its role in classical novae	95
6	$^{26}\text{Mg}(^3\text{He},d)^{27}\text{Al}$ Analysis and Results	99
6.1	Focal Plane Identification	99
6.1.1	Background Subtraction	101
6.2	Focal Plane Calibration	106
6.3	Focal Plane Fitting	108
6.3.1	Focal Plane Fits	111
6.3.2	Observed ^{27}Al Energy Levels	113
6.4	Angular Distributions	120
6.4.1	Low Energy Angular distributions	120
6.4.2	^{27}Al Angular distributions	123
7	$^{26}\text{Mg}(\alpha,t)^{27}\text{Al}$ Analysis and Results	126
7.1	Focal Plane Identification	126
7.1.1	Background Contaminants	129
7.2	Focal Plane Calibration	130
8	Discussion of $^{26}\text{Mg}(^3\text{He},d)^{27}\text{Al}$ and $^{26}\text{Mg}(\alpha,t)^{27}\text{Al}$ results	134
8.1	Discussion of $^{26}\text{Mg}(^3\text{He},d)^{27}\text{Al}$ Results	135
8.2	Discussion of $^{26}\text{Mg}(\alpha,t)^{27}\text{Al}$ Results	137
9	Conclusions and Future Work	139
A	DWBA Calculations	141
A.1	Optical Potential Parameters.	141
A.2	$^{22}\text{Ne}(^3\text{He},d)^{23}\text{Na}$ Angular distributions	143
B	Example Calculations	146
B.1	Differential Cross Section Calculation	146
B.2	$\omega\gamma$ Calculation	147
	Bibliography	150

List of Figures

1.1	Schematic Diagram showing the structure of a pre-supernova star. . .	15
1.2	Factor change $X_i=X_{rec}$ in final isotopic abundance as a result of varying the $^{34}\text{S}(p,\gamma)^{35}\text{Cl}$ reaction rate	20
1.3	Galactic ^{26}Al emission map as observed by the INTEGRAL satellite .	22
1.4	Reactions involved in the MgAl cycle.	23
2.1	Scattering in the centre of mass and laboratory frames.	27
2.2	Diagram for the definition of differential cross section.	29
2.3	Dependence of the reaction cross section for charged particles as a function of energy (arbitrary units)	37
2.4	Graph showing a neutron resonance in a potential well in ^{27}Al	39
3.1	Ion optical layout of the Q3D spectrometer.	46
3.2	Diagram showing trajectory of charged particles through a dipole magnet.	48
3.3	Diagram showing idealised magnetic field lines produced by a quadrupole magnet.	48
3.4	Side view schematic of the Q3D focal plane detectors.	50
3.5	Basic elements of a Photomultiplier tube.	51
3.6	A schematic diagram of MWPC2.	52
3.7	A schematic showing how focal-plane position of reaction products is determined using MWPC2	53
3.8	MWPC1 Anode charge versus MWPC2 Anode charge for ^3He nuclei impinged on ^{26}MgO target and scattered in to the Q3D at 5°	55
3.9	MWPC1 Anode charge versus Plastic Scintillator charge (pm) for ^3He nuclei impinged on ^{26}MgO target and scattered in to the Q3D at 5° .	56
4.1	Focal plane spectrum for Ag_2^{34}S at 5°	59

4.2	5° focal plane spectra for Ag_2^{34}S , $\text{Zn}_2^{\text{nat}}\text{S}$ and $^{\text{nat}}\text{C}$ targets.	60
4.3	10° focal plane spectra for Ag_2^{34}S , $\text{Zn}_2^{\text{nat}}\text{S}$ and $^{\text{nat}}\text{C}$ targets.	61
4.4	15° focal plane spectra for Ag_2^{34}S , $\text{Zn}_2^{\text{nat}}\text{S}$ and $^{\text{nat}}\text{C}$ targets.	61
4.5	25° focal plane spectra for Ag_2^{34}S , $\text{Zn}_2^{\text{nat}}\text{S}$ and $^{\text{nat}}\text{C}$ targets.	62
4.6	40° focal plane spectra for Ag_2^{34}S , $\text{Zn}_2^{\text{nat}}\text{S}$ and $^{\text{nat}}\text{C}$ targets.	62
4.7	Comparison of multiple asymmetric peak function fits on an isolated ^{35}Cl state.	65
4.8	Fitted Focal plane spectra at 5° for the Ag_2^{34}S Target	67
4.9	Fitted Focal plane spectra at 10° for the Ag_2^{34}S Target	68
4.10	Fitted Focal plane spectra at 15° for the Ag_2^{34}S Target	69
4.11	Fitted Focal plane spectra at 25° for the Ag_2^{34}S Target	70
4.12	Fitted Focal plane spectra at 40° for the Ag_2^{34}S Target	71
4.13	States used in the calibration of the focal plane for the $^{34}\text{S}(^3\text{He},\text{d})^{35}\text{Cl}$ reaction.	72
4.14	5° $^{34}\text{S}(^3\text{He},\text{d})^{35}\text{Cl}$ Focal Plane Calibration Curve.	73
4.15	Fitted Focal plane spectra for the $\text{Zn}_2^{\text{nat}}\text{S}$ target.	77
4.16	Deuteron angular distributions measured with the $^{32}\text{S}(^3\text{He},\text{d})^{33}\text{Cl}$ reaction at 20 MeV for $J=\ell+s$ coupling.	78
4.17	Deuteron angular distributions measured with the $^{34}\text{S}(^3\text{He},\text{d})^{35}\text{Cl}$ reaction at 20 MeV for $J=\ell+s$ coupling.	80
4.18	Deuteron angular distributions measured with the $^{34}\text{S}(^3\text{He},\text{d})^{35}\text{Cl}$ reaction at 20 MeV for $J=\ell-s$ coupling.	81
4.19	Angular distribution for the $E = 6.867$ MeV state in ^{35}Cl fit.	82
4.20	Thermonuclear $^{34}\text{S}(p,\gamma)^{35}\text{Cl}$ rates over typical nova peak temperatures	85
4.21	Minimum $^{34}\text{S}(p,\gamma)^{35}\text{Cl}$ thermonuclear reaction rate showing the contribution of individual states	86
4.22	Maximum $^{34}\text{S}(p,\gamma)^{35}\text{Cl}$ thermonuclear reaction rate showing the contribution of individual states	87
6.1	Focal plane spectrum for ^{26}MgO target at 5°	100
6.2	Overlay of ^{26}MgO , ^{24}MgO and $^{\text{nat}}\text{C}$ targets	101
6.3	Focal plane spectrum at 30° with the beam optics set to focus the elastically scattered ^3He beam.	102
6.4	Overlay of charge normalised deuteron focal plane spectra for ^{26}MgO (blue) and $^{\text{nat}}\text{C}$ (red) targets.	103

6.5	Deuteron focal plane spectra for ^{26}MgO target before and after carbon background subtraction.	104
6.6	Focal plane spectrum for $(^3\text{He,d})$ reactions on a SiO Target	105
6.7	Inelastic scattering of ^3He off ^{26}MgO and ^{24}MgO targets	106
6.8	Overlay of charge normalised deuteron focal plane spectra for ^{26}MgO and ^{24}MgO targets	107
6.9	Deuteron focal plane spectra for ^{26}MgO target before and after the subtraction of the scaled ^{24}MgO spectrum	108
6.10	5° focal plane spectrum for $(^3\text{He,p})$ reactions on a ^{26}MgO target . . .	109
6.11	5° $^{26}\text{Mg}(^3\text{He,d})^{27}\text{Al}$ Focal Plane Calibration Curve.	110
6.12	Fitted Focal plane spectra at 5° for the ^{26}MgO target	114
6.13	Fitted Focal plane spectra at 10° for the ^{26}MgO target	115
6.14	Fitted Focal plane spectra at 15° for the ^{26}MgO target	116
6.15	Fitted Focal plane spectra at 20° for the ^{26}MgO target	117
6.16	Fitted Focal plane spectra at 25° for the ^{26}MgO target	118
6.17	Fitted Focal plane spectra at 5° for the ^{26}MgO target.	119
6.18	Comparison of previous and present deuteron spectra for the $^{26}\text{Mg}(^3\text{He,d})^{27}\text{Al}$ between 7-8 MeV excitation energy.	122
6.19	Angular distributions of Wang <i>et al.</i>	123
6.20	Deuteron angular distributions measured with the $^{26}\text{Mg}(^3\text{He,d})^{27}\text{Al}$ reaction at 20 MeV for $J=\ell+s$ coupling.	124
7.1	Focal plane spectrum for the $50 \mu\text{g}/\text{cm}^2$ ^{26}MgO target at 10°	127
7.2	Total accumulated $^{26}\text{Mg}(\alpha,t)^{27}\text{Al}$ data using a $50 \mu\text{g}/\text{cm}^2$ ^{26}MgO target.128	
7.3	MWPC1 Anode charge versus MWPC2 Anode charge for the ^{nat}C target	129
7.4	Comparison of observed and known states from (α,α') reactions on a ^{26}MgO target.	132
7.5	Comparison of observed and known states from (α,d) reactions on a ^{26}MgO target.	133
A.1	Comparison of $^{22}\text{Ne}(^3\text{He,d})^{23}\text{Na}$ angular distribution fits.	144

List of Tables

1.1	Properties of Evolutionary ONe Novae Models used in the Iliadis sensitivity study	21
3.1	Targets used to study the $^{34}\text{S}(^3\text{He},\text{d})^{35}\text{Cl}$ reaction.	57
3.2	Targets used to study the $^{26}\text{Mg}(\alpha,\text{t})^{27}\text{Al}$ reaction	57
3.3	Targets used to study the $^{26}\text{Mg}(^3\text{He},\text{d})^{27}\text{Al}$ reaction.	57
4.1	States observed in the $^{34}\text{S}(^3\text{He},\text{d})^{35}\text{Cl}$ reaction.	74
4.2	Summary of ^{33}Cl angular distributions fits.	78
4.3	Nuclear structure of ^{35}Cl for states within $6.2 < \text{Ex} < 7.4$ MeV . . .	83
4.4	Resonance parameters for the $^{34}\text{S}(\text{p},\gamma)^{35}\text{Cl}$ Reaction.	84
4.5	New recommended Minimum and Maximum Reaction Rate for the $^{34}\text{S}(\text{p},\gamma)^{35}\text{Cl}$	89
4.6	Mean composition of the ejecta from a $1.35 M_{\odot}$ ONe white dwarf novae event.	91
5.1	Nuclear structure of ^{35}Cl for states within $6.2 < \text{Ex} < 6.8$ MeV . . .	94
5.2	Energy of ^{35}Cl states within $6.8 < \text{Ex} < 7.4$ MeV excitation energy .	96
5.3	Mean composition of the ejecta from a $1.35 M_{\odot}$ ONe white dwarf novae event.	97
6.1	States observed in the $^{26}\text{Mg}(^3\text{He},\text{d})^{27}\text{Al}$ reaction.	121
6.2	Nuclear structure of ^{27}Al for states within $13 < \text{Ex} < 13.7$ MeV . . .	125
8.1	Known states in ^{27}Al not observed in this work.	136
A.1	Summary of DWBA fits and extracted spectroscopic factors.	145
B.1	Table of fit parameters for the 6.867 MeV state in ^{35}Cl at all angles. .	147
B.2	Experimental differential cross sections for the 6.867 MeV state in ^{35}Cl .	148

Acknowledgements

This thesis would not have been possible without the support of many people and I would like to take a moment to thank those responsible for me completing my PhD. The first and biggest thanks must go to my supervisor Charles J. Barton III. He was the best supervisor I could of asked for and was always available to talk to me about physics, advise me on all aspects of life and most importantly always had his wallet out at the bar. Without his support I would be half the physicist I am today.

Second (and third) I must thank the people responsible for providing me with the data that contained within this thesis Anuj Parikh and Nicolas de Séréville. I would like to further acknowledge the support that Anuj has given me analysing this data and writing the subsequent paper.

I must highlight the contributions of two of my fellow PhD students, Jos Riley and Matt Williams who were with me in Munich when my thesis data was collected. Without them it would not have been possible to run the experiment for an extra day and I would not have the been able to collect the Sulphur data which ended up being the bulk of this work.

I would also like to thank all the staff members in the Physics group who have helped me in my 8 years at York. Specifically I would like to thank Professors Bob Wadsworth and Mike Bentley whose undergraduate courses first got me interested in Nuclear physics, Alison Laird who taught me most of what I know about Nuclear Astrophysics and finally Andrei Andreyev for giving me my first Post-Doc while I was waiting for my viva. A special mention must be given to Ben Kay for giving me my PhD position in the first place. Although he left York before I started, everything worked out well for me in the end.

I must also acknowledge the support I have received from my fellow PhD students. Whenever I was having trouble with my work I could always find someone who was

willing to help. I wish you all the best in your future endeavours.

Finally I must thank my parents, my brother David and all my extended family for all the support I have received over the years. I am only where I am today because of all of you.

Declaration

This thesis is the work of Stephen Alexander Gillespie alone, apart from where private communications are noted in the text. All materials from other sources are referenced in the text and acknowledged in the bibliography. None of the material in this thesis has been presented for examination previously.

Chapter 1

Introduction

The work described in this thesis concerns the study of reaction rates in astrophysical environments through indirect methods using transfer reactions. Specifically, the reactions investigated in this work concern the proton destruction rate of ^{34}S and the neutron destruction rate of ^{26}Al . The $^{34}\text{S}(p,\gamma)^{35}\text{Cl}$ reaction rate has been studied indirectly with the $^{34}\text{S}(^3\text{He},d)^{35}\text{Cl}$ transfer reaction and states important to the neutron destruction reactions $^{26}\text{Al}(n,p/\alpha)$ have been studied through indirect methods with the $^{26}\text{Mg}(^3\text{He},d)^{27}\text{Al}$ and $^{26}\text{Mg}(\alpha,t)^{27}\text{Al}$ transfer reactions. The astrophysical sites, classical novae, Type II supernova and massive stars and motivation for studying these reactions will be discussed in sections 1.2.3 and 1.2.4.

1.1 Astrophysical Sites

Astrophysical reaction rates are highly sensitive to the thermal and chemical conditions within stellar environments. A reaction may have a large impact on the chemical composition of one stellar environment, but will have a negligible impact if conditions, such as temperature, are different than the original environment. It is therefore necessary to understand the different stellar environments in which reactions can occur. The reactions covered in this work involve multiple environments which will be discussed briefly in the following sections. More detailed descriptions of these sites in regards to the relevant reactions will be given in sections 1.2.3 and 1.2.4. The reactions occur at different stages of stellar evolution so

it is necessary to describe several possible paths of stellar evolution. As the reactions occur during the end stages of stellar evolution, neither protostar formation or the burning process of the main sequence will be discussed. The following sections will describe the possible pathways following termination of core hydrogen burning. The mass of the star at this stage determines the endpoint of stellar evolution for that star.

1.1.1 White Dwarf

For a star with mass $0.4M_{\odot} < M < 10M_{\odot}$ following the depletion of core hydrogen, there is no longer sufficient energy generation to prevent gravitational collapse of the star's core. As the star begins to collapse it will heat up until a thick layer of hydrogen surrounding the core is able to undergo hydrogen burning. The energy produced during this burning process causes the surface of the star to expand. At this stage the star is known as a red giant. The collapse of the core continues until it reaches electron degenerate conditions. The temperature of the core of the star continues to increase and it becomes possible for helium burning to occur at $T \approx 0.1$ GK. During this burning phase helium nuclei begin to fuse and cause a build up of carbon and oxygen within the core. For stars with mass $0.4M_{\odot} < M < 2M_{\odot}$ the star core will be under electron degenerate conditions and energy released in the helium burning will cause a thermonuclear runaway within the core. The energy released during this runaway will overcome the gravitational collapse of the core causing it to expand and breaking electron degeneracy. For stars of mass $2M_{\odot} < M < 10M_{\odot}$ electron degeneracy in the core is not reached and helium will continue to burn under normal conditions. During the helium burning phase a series of dredge ups occur, where the core fusion products are mixed into the outer layers of the stellar atmosphere through strong convective currents, resulting in significant mass loss via stellar winds. Depending upon the initial mass of the star the end result of this process is a CO or ONe white dwarf star [1].

1.1.2 Wolf-Rayet Star

For very massive stars $M > 11M_{\odot}$ the hydrogen burning phase occurs over a much shorter period of time, typically millions of years. Following the termination of hydrogen burning the core contracts until the temperature is hot enough for

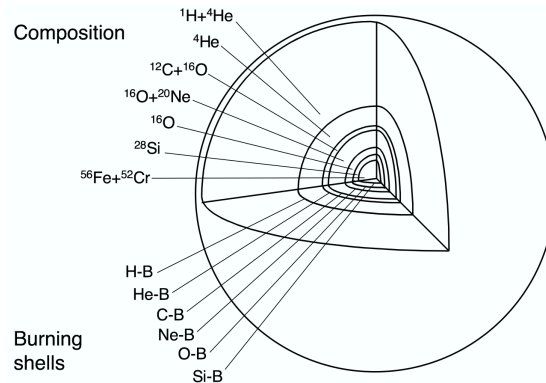


Figure 1.1: Schematic Diagram showing the structure of a pre-supernova star [1]. Labelled on the upper left side of the figure are the most abundant nuclear species in each shell. Nuclear burning shells are labelled in the bottom left of the figure. H-B, He-B, C-B, Ne-B, O-B and Si-B refer to the hydrogen, helium, carbon, neon, oxygen and silicon burning shells respectively.

helium burning to occur. The extra heat from helium burning ignites the hydrogen surrounding the core and the outer layers of the star expand with the star becoming a super giant. Core helium burning continues until there is insufficient material available to burn. The core will again contract until temperatures are sufficiently hot for carbon burning. Helium burning will resume in a shell surrounding the carbon burning core with a hydrogen burning shell surrounding the helium. Other burning stages follow carbon burning with neon, oxygen and silicon burning sequentially as the core depletes the required seed material. As seen in Figure 1.1 the star adopts an onion like structure with an iron core surrounded by successive shells of burning and a hydrogen outer layer. Strong stellar winds cause a significant loss of the outer hydrogen layer with the effect more pronounced in the largest stars, those with masses $M \geq 30-35M_{\odot}$, where most of the outer layers are lost. This results in weak or absent hydrogen lines in the emission spectra. These stars are known as Wolf Rayet stars [1].

1.1.3 Type II Supernova

A Type II supernova is the endpoint of the stellar evolution of a massive star. As described in the preceding section, a massive star adopts an onion like structure of burning shells with an iron core supported by electron degeneracy. With no other sources of energy available via burning processes the mass of the core will continue

to grow as the outer layers continue to burn and contribute matter. Eventually the mass of the core reaches the Chandrasekhar limit [2], the maximum mass of an object for which electron degeneracy pressure is sufficient to overcome gravitational collapse. When this limit is reached the core will begin to collapse. This process is accelerated by two processes, the capture of electrons by the iron nuclei, which reduces the electron density and subsequently the electron degeneracy pressure. In addition the temperature of the star becomes sufficient for direct photodisintegration of the iron nuclei into lighter nuclei which removes energy from the core. The collapse of the core continues until nuclear density is reached. At this density the strong force is repulsive which causes the core to rebound. The rebounding core will encounter the infalling matter which gives rise to an outward moving shockwave. The shock wave will lose energy through photodisintegration of iron nuclei and the emission of neutrinos and will eventually stall. Through a process that is not presently known the shock wave will restart and propagate through the outer layers of the star. As it moves through the layers, nucleosynthesis can occur in the different burning shells. The shock wave will eventually reach the edge of the star where a large amount of matter is ejected into the interstellar medium (ISM). Through a presently unknown mechanism the core of the star will collapse into a neutron star or black hole [1].

1.1.4 Binary Systems

Most stars exist in binary systems where their evolution is significantly affected by their companion star. Each star has its own gravitational boundary known as its Roche limit with a Lagrangian point existing at their intersection. If the initial masses of the stars are different they can evolve at different rates, so that one star may have reached its evolutionary end point while the companion star is still developing.

1.1.4.1 Type 1A Supernova

A Classical Type 1A supernova occurs in binary systems consisting of a white dwarf star with a main sequence or red giant as a companion. If the outer layers of the companion star exist within the gravitation boundary of the white dwarf, matter can be accreted from the companion star to the surface of the white dwarf star. If the rate of matter accretion is sufficiently large, $M \approx 10^{-7} M_{\odot} \text{yr}^{-1}$ [1] the white dwarf

will begin to increase in mass. When the white dwarf reaches the Chandrasekhar limit [2], the maximum mass of the white dwarf, the pressure is sufficient for carbon burning to occur. As the burning occurs under electron degenerate conditions the white dwarf cannot expand to counteract the heating which results in thermonuclear runaway. The energy released during this runaway is eventually so great as to unbind the white dwarf which violently explodes. Following this supernova, nothing remains of the initial star with the material being expelled into the interstellar medium (ISM). Type 1A supernovas involving a single white dwarf are believed to account for at most 20% of the total number of the observed Type 1A events [3]. Type 1A supernovas can also occur following the merger of two white dwarfs. The classification Type 1 refers to an absence of hydrogen lines in the emission spectra, opposed to Type II supernova which have hydrogen lines in there spectra. Supernova are further subdivided based on the presence or absence of other spectral lines, with Type 1a showing a strong silicon emission line at 615 nm. [1].

1.1.4.2 Classical Novae

Classical novae occur in a binary system consisting of a white dwarf and red giant. Similar to Type 1A events matter is accreted from the red giant to the white dwarf. The rate of matter accretion however, is smaller than required for a Type 1A supernova. The hydrogen rich material accreted onto the surface is compressed and begins to fuse into helium nuclei. Thermonuclear runaway occurs on the surface of the star which eventually causes an explosion, ejecting matter into the ISM. Classical novae are less explosive events than Type 1A supernova with the white dwarf remaining intact. With both stars remaining intact matter will continue to be accreted and the classical novae can reoccur, typically with a time period of 10^4 - 10^5 years.

1.2 Astrophysical Motivation

1.2.1 Astrophysical Observables

To relate nuclear reaction rates to astrophysical environments it is necessary to have astronomical observations that are sensitive to the decay of nuclei that are products or daughters of nuclear reactions. Radioactive isotopes decay with characteristic γ

lines, which can be identified with satellite based γ -ray detectors. Pinpointing the source of these emissions allows regions of nuclear synthesis to be identified. The COMPTEL [4] and INTEGRAL [5] satellites have been used to provide all sky maps of γ ray lines to identify the production of specific isotopes. In addition, during certain burning process the outer layers of stars are transparent to γ rays. Their observation therefore provides a means to view the stars' interior.

It is also possible to study the reactions which occur within stellar environments, by studying their ejecta. During the final stages of stellar evolution a large amount of material rich in heavy nuclei is ejected into the ISM. As the ejecta cools the matter will begin to coalesce into small grains. During the formation of the solar system, these grains are then embedded in meteorites. The isotopic composition of these grains differ from that of the surrounding material indicating they pre-date the formation of the Sun, hence they are known as presolar grains. Isotopic ratios of pre-solar grains often show excesses of specific isotopes which can be used to determine their origin. As nuclear reactions are very sensitive to temperature, the measured isotopic ratios will depend on the stellar environment they were produced in. Understanding reaction rates will therefore provide information on the conditions within stars at the time of synthesis which can be used to constrain stellar models.

1.2.2 Sensitivity Studies

Nuclear reactions govern the evolution of stellar environments as they are responsible for the energy generation and the chemical-element synthesis in stars. Knowledge of nuclear reactions is therefore essential to understand how stars evolve. The problem, however, is that this evolution is not driven by a single reaction, but several thousands of co-dependent reactions. It is not feasible to measure every reaction, so there is a need to identify which are the key reactions that must be measured. These key reactions are not necessarily the most important reactions which occur in a stellar environment, for example those that generate the most energy, but rather the ones whose uncertainties have the largest impact on stellar models.

A sensitivity study is one method of identifying these key reactions [6–8]. In a sensitivity study, nuclear synthesis calculations are performed for a given environment. Individual reaction rates, in both the forwards and reverse directions, are varied one at a time within their uncertainties and new calculations are

performed to see how isotopic yields are affected. Experimental rates are used whenever possible, with statistical models used when no other data are available. Full hydrodynamic calculations are computational intensive, so are not suitable when performing a large number of calculations. Sensitivity studies solve these issues by making assumptions about the initial composition of the environment as well as how the temperature and pressure evolve. These thermodynamic profiles are taken from current hydrodynamic simulations. This approach neglects important effects such as convective mixing [9, 10] so cannot calculate absolute abundances, however it is useful to explore the effects of reaction rate uncertainties to identify key reactions.

1.2.3 Motivation $^{34}\text{S}(^3\text{He},\text{d})^{35}\text{Cl}$

Current models of nucleosynthesis in classical novae find elemental abundances which are in broad agreement with the observed ejecta. These models predict that the heaviest isotopes, in the Si-Ca mass region [11–13], are synthesised only in massive ONe white dwarfs. A more stringent test of models, however could be obtained from the isotopic composition of ejecta observed in pre-solar grains. The problem arises, however that only a few grain measurements show signatures of classical novae origin [14–16] and these are also found to be consistent with type II supernova origin [17, 18]. It would be advantageous, therefore to have a set of isotopic ratios which can be used as a test to discriminate pre-solar grains from different stellar sites.

Sulphur isotopes have been proposed as a possible diagnostic tool to determine pre-solar grain paternity. Measurements of sulphur isotopic ratios in SiC grains show clear evidence of ^{32}S over-abundance, or depletions of the heavier $^{33,34}\text{S}$ isotopes, relative to the solar abundances [19–21]. Measurements of the isotopic ratios $^{32}\text{S}/^{34}\text{S}$ and $^{32}\text{S}/^{33}\text{S}$ could therefore be used to with other common isotopic ratios $^{12}\text{C}/^{13}\text{C}$, $^{14}\text{N}/^{15}\text{N}$ and $^{29,30}\text{Si}/^{28}\text{Si}$ [16], to determine pre-solar grain paternity. The $^{32}\text{S}/^{33}\text{S}$ ratio has been updated recently [22] and has shown to be successful in differentiating grains from classical novae and type II supernova events.

Due to uncertainties in several reaction rates, most prominently the $^{34}\text{S}(\text{p},\gamma)^{35}\text{Cl}$ reaction, the $^{32}\text{S}/^{34}\text{S}$ ratio is unable to be used as a diagnostic. Presently the recommended $^{34}\text{S}(\text{p},\gamma)^{35}\text{Cl}$ reaction rate [26] is obtained from a statistical model. A sensitivity study by Iliadis [6] varied this reaction rate within uncertainties and

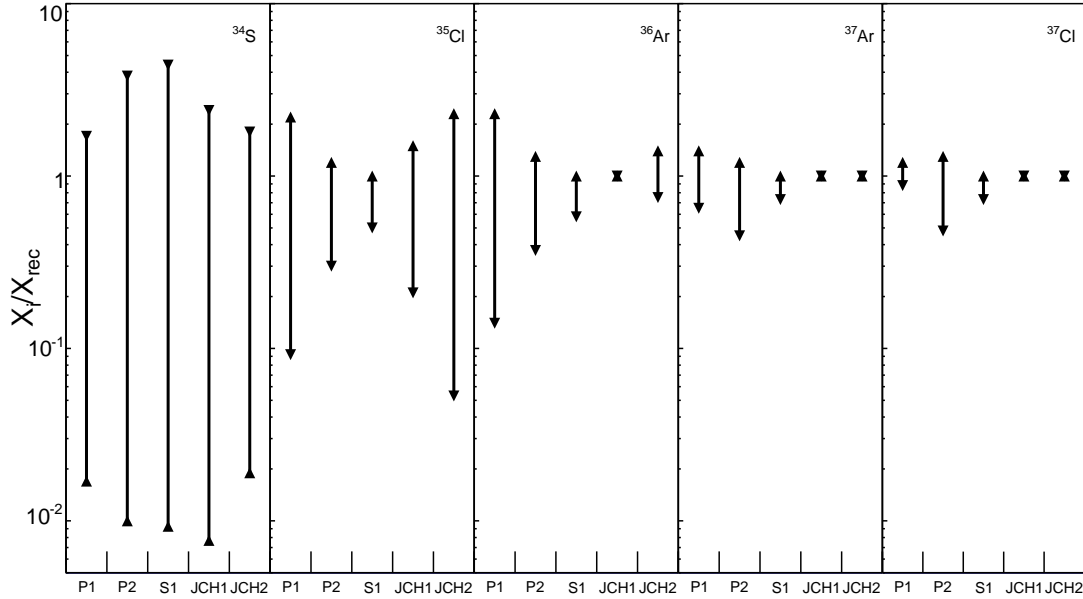


Figure 1.2: Factor change $X_i=X_{rec}$ in final isotopic abundance as a result of varying the $^{34}\text{S}(p,\gamma)^{35}\text{Cl}$ reaction rate within present uncertainties. Data is taken from [6]. X_{rec} is the isotopic abundance using the current recommended reaction rate and X_i is isotopic abundance when the reaction rate is multiplied by a specific factor which depends on the reaction rate uncertainties. Triangles pointing up and down correspond to the upper and lower limit of the reaction rate, respectively. The horizontal axis refers to specific ONe novae models whose parameters are given in Table 1.1.

found that the abundance of ^{34}S can vary by as much as a factor of 130, depending upon the model used. In addition, this reaction rate has a significant effect on ^{35}Cl and ^{36}Ar abundances. Figure 1.2 shows the variation in isotopic abundances, given present uncertainties, for a variety of novae models, whose properties are summarised in Table 1.1. Variations between these models arise due to the initial mass of the white dwarf and the total mass accreted to the white dwarf prior to the novae event. Using this reaction rate, nova models predict a $^{32}\text{S}/^{34}\text{S}$ isotopic ratio of $\approx 10 - 4400$ [6]. Current Type II supernova models predict a ratio of 19 - 38 [27], so it is clear a new rate is required to distinguish grains from these two events.

An experimental reaction rate has not been calculated due to limited information in the temperature region of interest, corresponding to states within 600keV of

Table 1.1: Properties of Evolutionary ONe Novae Models used in the Iliadis sensitivity study [6]. The models labelled P, S, and JCH are adopted from Politano *et al.* [23], Starrfield *et al.* [24] and José *et al.* [25]. The input parameters in the model are the initial mass of the White dwarf, WD, the level of mixing between the accreted matter and the white dwarf, the peak temperature and luminosity of the classical novae, T_{peak} and L_{peak} . The rate of mass accretion is shown as δM_{acc} with the total mass accreted to the white dwarf given as M_{acc} . Following the novae event a total mass M_{ej} is ejected into the ISM.

Model	P1	P2	S1	JCH1	JCH2
WD mass (M_{\odot})	1.25	1.35	1.35	1.15	1.25
Mixing (%)	50	50	50	50	50
T_{peak} (10^6 K)	290	356	418	231	251
L_{peak} ($10^4 L_{\odot}$)	4.3	16.3	39	26	46
M_{acc} ($10^{-5} M_{\odot}$)	3.2	1.5	3.8	3.2	2.2
δM_{acc} ($10^{-10} M_{\odot} \text{ yr}^{-1}$)	16	16	1.6	2.0	2.0
M_{ej} ($10^{-5} M_{\odot}$)	0.0	0.62	2.2	2.6	1.8

the proton threshold in ^{35}Cl . There are only a few energy levels in this region identified from (α, p) transfer reactions and of these no spin, parity, or resonance strengths are known [28]. Above 7 MeV the nucleus has been studied extensively through (p, γ) reactions [29–31]. A more detailed spectroscopic study in the 6-7 MeV excitation region in ^{35}Cl is therefore required to reduce experimental uncertainties in the $^{34}\text{S}(p, \gamma)^{35}\text{Cl}$ reaction rate. For this reason an experimental measurement of the $^{34}\text{S}(^3\text{He}, d)^{35}\text{Cl}$ reaction was performed with the aim of identifying new energy levels, making spin and parity assignments and using this information calculate an experimental reaction rate.

1.2.4 Motivation $^{26}\text{Mg}(^3\text{He}, d)^{27}\text{Al}/^{26}\text{Mg}(\alpha, t)^{27}\text{Al}$

The nucleus ^{26}Al has been of great importance to understand the chemical evolution of the galaxy. The nucleus decays via beta decay to an excited state in ^{26}Mg which de-excites by emitting a 1.809 MeV γ ray. The observation of this γ -ray transition was suggested as the most promising evidence of ongoing nucleosynthesis due to the short half life of the nucleus, 7.2×10^5 yr, in comparison to the galactic timescale, $\sim 10^{10}$ yr [32, 33]. This line was first observed by a germanium detector

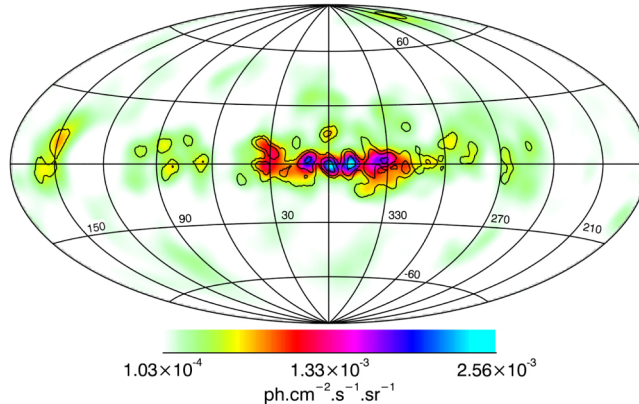


Figure 1.3: Galactic ^{26}Al emission map as observed by the INTEGRAL satellite [36]. Shown is the flux of the 1.809 MeV emission line in units of $\times 10^3 \text{ photons cm}^{-2} \text{ s}^{-1} \text{ sr}^{-1}$ with contours showing galactic longitude, l and latitude, b . ^{26}Al is shown to be concentrated in specific galactic regions which can be correlated to known regions of stellar formation. These include the Perseus region ($105^\circ \leq l \leq 170^\circ$), Cygnus/Cepheus region ($75^\circ \leq l \leq 100^\circ$), the inner Galaxy ($30^\circ \leq l \leq 30^\circ$, $10^\circ \leq b \leq 10^\circ$), Carina ($l = 286^\circ$, $b = 1^\circ$), and the Vela region ($260^\circ \leq l \leq 270^\circ$).

aboard the HEAO 3 satellite [34], with later instruments such as COMPTEL [4] and INTEGRAL [5] mapping this line across the galaxy. The most current map can be seen in Figure 1.3. When combined with maps of other wavelengths the origin of the ^{26}Al line could be attributed to regions with massive star population [35–37].

There is also evidence of ^{26}Al in meteorites based on excesses of the daughter nucleus ^{26}Mg with respect to ^{24}Mg . The first evidence of this was through measurements of Calcium-Aluminium Inclusions (CAIs) in the Allende meteorite [38]. During the early formation of the solar system CAIs would be among the first solids to condense [39], so excesses of ^{26}Mg would suggest ^{26}Al was present in the early solar system. Currently it is believed that contamination from massive stars is responsible for this excess [40, 41]. Understanding how ^{26}Al forms in massive stars will provide crucial information on the early formation of the solar system.

While massive stars are currently the favoured site of ^{26}Al production there is still much information required to constrain reaction rates. The production of ^{26}Al occurs at different stages of a massive stars evolution and it is crucial to understand which reactions affect the final abundances at each stage. To this end Iliadis *et al.* [7] performed a sensitivity study, varying multiple reaction rates within their uncertainties to identify the reactions which have the most affect on final ^{26}Al abundances. The three stages of stellar evolution which were investigated are

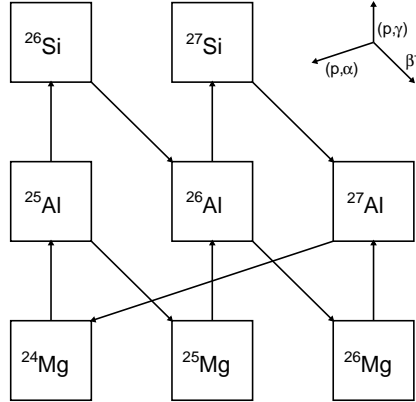


Figure 1.4: Reactions involved in the MgAl cycle. Through a series of (p,γ) reactions and β decays hydrogen is burned and converted into helium.

summarised below.

Core Hydrogen Burning With sufficient seed material core hydrogen burning can proceed through a series of (p,γ) and (p,α) reaction on nuclei with $A > 20$. Several chains of reactions are possible and one such chain which affects ^{26}Al abundance is the MgAl cycle, the key reactions of which can be seen in Figure 1.4. During core hydrogen burning ^{26}Al is produced in the $^{25}\text{Mg}(p,\gamma)^{26}\text{Al}$ reaction and is destroyed mainly through β decay. This process terminates when hydrogen burning can no longer occur and the core collapses to burn helium. The amount of ^{26}Al produced during the core hydrogen burning phase which is then ejected into the ISM is dependent upon the mass of the star. For lighter stars, any ^{26}Al still left in the core will be destroyed through (n,p) and (n,α) reactions. Only a small amount of ^{26}Al present in the outer hydrogen envelope remains which will then be ejected when the star explodes. For heavier stars strong stellar winds can eject the ^{26}Al before it can be destroyed [42].

Convective Shell C/Ne Burning As with the core hydrogen burning phase ^{26}Al is produced in the C/Ne convective shell via the $^{25}\text{Mg}(p,\gamma)^{26}\text{Al}$ reaction. The initial CNO abundances in the carbon burning shell are directly responsible for the amount of ^{25}Mg which is created through the sequence, $\text{CNO} \rightarrow ^{14}\text{N} \rightarrow ^{22}\text{Ne} \rightarrow$

^{25}Mg . A significant proportion of ^{25}Mg is left unburned in the carbon burning shell and will be destroyed during neon burning. High temperatures within the neon shell would eventually destroy any ^{26}Al produced, however strong convective currents simultaneously bring fresh ^{25}Mg seed material into the neon burning shell and the ^{26}Al into lower temperature shells where its lifetime is significantly increased. When the star explodes it is then possible for the produced material to be emitted into the ISM. In present calculations the destruction rate of ^{26}Al is dominated by β decay, however, the sensitivity study found varying the $^{26}\text{Al}(n,p)^{26}\text{Mg}$ reaction rate had a significant effect on the final ^{26}Al abundance. Varying the rate of this reaction within its uncertainties leads to it being the dominant source of ^{26}Al destruction, instead of β decay, which highlights the need for a new improved measurement.

Explosive Ne/C Burning

During the explosion of the star as the temperatures reaches ~ 2.3 GK, ^{26}Al is produced strongly within the carbon neon shells and emitted into the ISM. As before the dominant production method for ^{26}Al is the $^{25}\text{Mg}(p,\gamma)$ reaction, with the ^{25}Mg produced from neutron capture on ^{24}Mg which remains after carbon and neon burning [42]. The major source of ^{26}Al destruction during the explosive Ne/C burning stage are the $^{26}\text{Al}(n,p)^{26}\text{Mg}$ and $^{26}\text{Al}(n,\alpha)^{23}\text{Na}$ reactions. The explosive Ne/C burning phase is found to be the major contributor of the total ^{26}Al yield, therefore it becomes necessary understand its destruction rate through the $^{26}\text{Al}(n,p/\alpha)$ reactions.

1.2.4.1 The $^{26}\text{Al}(n,p/\alpha)$ reactions and their role in the destruction of ^{26}Al

The $^{26}\text{Al}(n,p/\alpha)$ reactions rates have not been measured directly and the adopted rates are theoretical models based on a statistical model [43], see section 2.4.3 for more details. As it is difficult to estimate the uncertainties of the current reaction rate it becomes necessary for a new rate to be calculated based on experimental data in order to understand how ^{26}Al is produced in stellar environment.

The $^{26}\text{Al}(n,p/\alpha)$ reactions proceed through states up to 500 keV above the neutron threshold in ^{27}Al . These states lie within the Gamow window which will be discussed in section 2.3. Detailed spectroscopic studies in this region are therefore essential

to calculate an experimental reaction rate. Previous studies which have populated this region include, a $^{23}\text{Na}(\alpha, \text{p})^{26}\text{Mg}$ study by Whitmire *et al.* [44], a $^{23}\text{Na}(\alpha, \gamma)^{27}\text{Al}$ study by de Voight *et al.* [45] and a $^{26}\text{Al}(\text{n}, \alpha)^{23}\text{Na}$ study by de Smet *et al.* [46]. There is little agreement however, between the data. The excitation energy regions populated by de Voight and de Smet populate do not overlap and the reaction employed by Whitmire should populate different states due to the selectivity of the reaction, see section 2.1.3.3 for more details. The large uncertainties in the energy obtained by Whitmire *et al.*, 8.5 keV, also makes any comparison difficult, especially considering the high level density expected in this region.

This region has been studied recently using the $^{27}\text{Al}(\text{p}, \text{p}')^{27}\text{Al}$ [47] reaction and an Enge-Split pole spectrometer [48]. Over 30 new states above the neutron threshold were reported, however no other spectroscopic information could be extracted. Without this information an experimental reaction rate cannot be calculated, see section 2.4 for details. In order to extract the necessary spin parity information an experiment was performed using the $^{26}\text{Mg}(\text{}^3\text{He}, \text{d})^{27}\text{Al}$ and $^{26}\text{Mg}(\alpha, \text{t})^{27}\text{Al}$ transfer reactions. The two reactions preferentially populate low and high spin states respectively and when combined with other complementary studies allow new $^{26}\text{Al}(\text{n}, \text{p}/\alpha)$ reaction rates to be calculated.

Chapter 2

Theory

The study of reaction rates in astrophysical environments requires detailed knowledge of nuclear structure. In particular it is important to not only know which states are present within the nucleus, but which states may contribute to the total reaction rate for specific astrophysical environment. Spectroscopic studies must therefore be performed in order to extract the properties of these states. Following the extraction of these properties reaction rates are determined and are used to predict nuclear synthesis yields, which can be compared to astrophysical observables such as cosmic γ ray lines and pre-solar grains. In this chapter reaction rates will be discussed and in particular the necessary inputs from nuclear physics. Nuclear reaction mechanisms will be detailed in section 2.1 with the theoretical models discussed in section 2.2. Section 2.3 will discuss the Gamow window and its importance to astrophysical reactions, with the formalism of thermonuclear reaction rates described in section 2.4.

2.1 Nuclear Reactions

A nuclear reaction involving two colliding particles often involves the exchange of energy and/or nucleons. The measurement of one of these particles following a collision can be used to extract nuclear information on both particles. Reactions are sensitive to nuclear properties, so when performing an experiment it is important to select a reaction which populates states of interest. Many types of reactions are available, however they can be separated into two different classes of reactions;

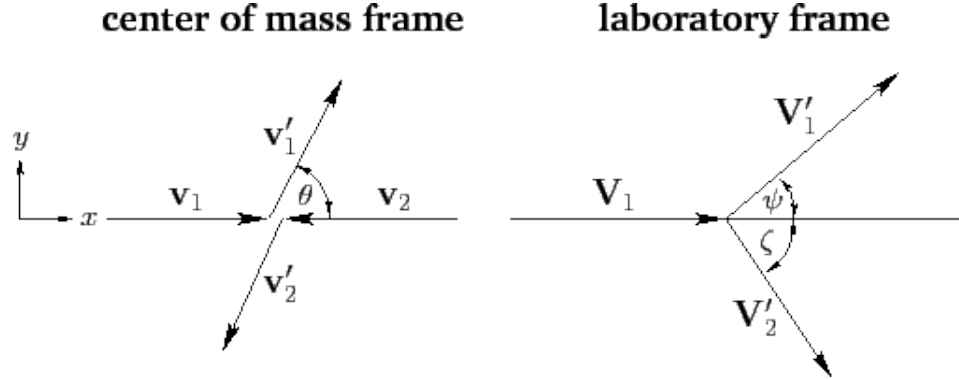


Figure 2.1: Scattering in the centre of mass and laboratory frames [49]. The velocity of the two colliding particles 1,2 before the collision are denoted by the letter v in the CoM frame and V in the laboratory frame. Following the collision the particles are scattered at an angle θ in the CoM frame and ψ and ζ in the laboratory frame with a velocity denoted with a prime superscript.

direct and compound. The time-scale for the reaction determines whether they are a direct or compound reaction with direct reactions occurring more quickly. Direct and compound reactions will be discussed in more detail in sections 2.1.3 and 2.1.4. When discussing any type of nuclear reaction there are several properties common to all which will be discussed below.

2.1.1 Centre of Mass Frame

In a typical nuclear physics reaction a stationary target nucleus A is bombarded with a projectile nucleus B. The same reaction can also be performed by firing the nucleus A at a target containing nuclei B. To compare theoretical models to experimental data a coordinate system is used which is invariant of the motion of the two nuclei. The coordinate system employed is the Centre of Mass (CoM) system, in which the centre of mass of the colliding nuclei is at rest. In this system the two nuclei have equal and opposite momentum before and after the collision ensuring the CoM remains at rest. The kinematics of reactions in the laboratory and CoM frames can be seen in Figure 2.1. As measurements are taken in the laboratory reference frame it is necessary to convert them into the centre of mass frame in order to compare to theoretical calculations.

2.1.2 Cross Section

A useful measure of a reaction is the probability that it can occur. The quantity used is the cross section, σ which is defined as:

$$\sigma = \frac{\text{Number of reactions}}{\text{Number of Beam Particles} \times \text{Number of Target Atoms per unit Area}} \quad (2.1)$$

and has dimension of area. Cross sections are given in units of barns ($1\text{b} = 10^{-28}\text{m}^2$) or the subunits millibarns and microbarns.

Due to experimental constraints, such as limited numbers of detectors, it is not always possible to measure a reaction at all angles. Instead it is useful to have a measure of the cross section at a specific point, defined by the polar coordinates (θ, ϕ) relative to the beam axis as seen in Figure 2.2, which corresponds to the location of the detectors. The number of scattered particles into a given solid angle $d\Omega$ is defined by the differential cross section $d\sigma(\theta, \phi)/d\Omega$. Unless the beam or target is polarised, scattering is symmetrical around the beam direction and independent of ϕ . The total cross section can then be obtained by integrating the differential cross section:

$$\sigma = \int \frac{d\sigma(\theta)}{d\Omega} d\Omega. \quad (2.2)$$

Differential cross sections are often plotted as angular distributions which describe how the cross section varies as a function of θ . Angular distributions are dependent upon angular momentum transfer and are compared to theoretical calculations to extract information on the colliding nuclei.

2.1.3 Direct Reactions

A direct reaction is defined as a nuclear reaction where the two colliding nuclei make a glancing contact and immediately scatter. The timescale of this reaction is short and often involve the interaction of only a few nucleons, usually at the surface of the nucleus. Direct reactions proceed immediately between the initial and final states. The overlap of these wavefunctions describes the probability that the reaction can occur between these states from which nuclear structure information can be extracted. There are several types of direct reactions and the choice of the reaction influences what information can be obtained. Direct reactions relevant to the work in this thesis will be discussed below.

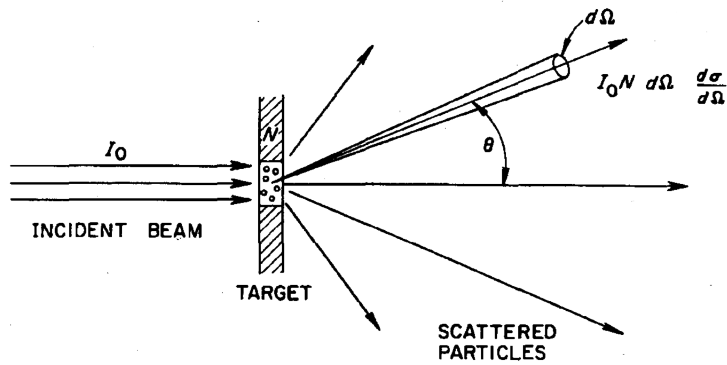


Figure 2.2: Diagram for the definition of differential cross section [49]. An incident beam of I_0 particles per second collides with a target of thickness N and is scattered at an angle θ . The total number of particles scattered into an element of solid angle $d\Omega$ can be related to the incident beam current and target thickness through the differential cross section $d\sigma/d\Omega$

2.1.3.1 Elastic Scattering

For the case of elastic scattering the internal structure of the colliding particles remain the same before and after the collision. The internal energy of the colliding particles remain unchanged and the kinetic energy is conserved in the CoM frame. The cross section for elastic scattering is proportional to the sum of the charge radii of the colliding particle. This property allows elastic scattering measurements to be used to measure the charge radius of nuclei. Optical models use potentials derived from elastic scattering experiments to model scattering processes (see section 2.2.1 for details).

2.1.3.2 Inelastic Scattering

During an inelastic scattering process there is an exchange of energy between the two nuclei leaving one or both in an excited state. By measuring the scattered particle it is possible to study excited states within the nucleus. Inelastic scattering is a non-selective reaction mechanism and is able to populate all states regardless of spin.

2.1.3.3 Transfer reactions

A transfer reaction involves the exchange of one or more nucleons between the two colliding particles. Following the exchange of the nucleon/s the target can be left in an excited state. As is the case for inelastic scattering measuring the scattered particles can be used to study states in the target nucleus. Transfer reactions are, however selective in the levels they populate [50]. This can be explained classically where the angular momentum, ℓ , transferred can be approximated as:

$$\ell = Rq, \tag{2.3}$$

where R is the interaction distance and q is the transferred linear momentum between the incoming and outgoing scattered beams, with magnitude:

$$q^2 = (p_i^2 + p_f^2 - 2p_i p_f \cos(\theta)), \tag{2.4}$$

where $p_{i,f}$ is the initial and final momentum of the particle which is scattered at an angle θ . It is clear from eqs. (2.3) and (2.4) that the change in momentum between the incoming and outgoing channels determines the ℓ transfer. It is therefore possible to select reactions which will preferentially populate low or high spin states. In this work two proton-transfer reactions are used, the (${}^3\text{He},d$) reaction, to populate low-spin states and the (α,t) reaction for high-spin states.

2.1.4 Compound Reactions

A compound reaction involves the collision of two nuclei which then coalesce forming a compound nucleus. This nucleus exists for a sufficient time, $\sim 10^{-19}$ s, that the excitation energy is shared uniformly amongst all of the nucleons. If the energy of this compound is sufficiently high the nucleus can decay through the emission of one or more nucleons. Due to the long interaction time the decay of the compound nucleus is found to be independent of its formation. The compound nucleus forgets how it was formed and will decay in the same way regardless of the reaction which created it, provided the nucleus has the same total energy.

2.2 Reaction Theory

Direct reactions can be modelled using scattering theory where an incoming beam represented as a plane wave of the form:

$$\psi_a = Ae^{i(kz-\omega t)}, \quad (2.5)$$

scatters off a potential V . Equation (2.5) uses the standard definition for plane wave where ϕ_a is the magnitude of a wave at a specific point in space and time. A is the peak amplitude of the wavefunction, with k being the wave number, ω is the angular frequency and z and t are the specific point in space and time of the wavefunction. Following this interaction the outgoing scattered wave is modelled as a radial wave:

$$\psi_{scatt} = f(\theta) \frac{e^{(ikr)}}{r}, \quad (2.6)$$

which is symmetric about the beam axis. The parameter $f(\theta)$ is the amplitude of the wavefunction about θ and r is the radial distance from the interaction point. The whole scattering process can then be described by a wavefunction which is the sum of eqs. (2.5) and (2.6) for all available reaction channels. This wavefunction χ must be a solution of the the Schrödinger equation:

$$\left[\frac{\hbar^2}{2m} \nabla^2 + V(r) \right] \psi(r) = E\psi(r), \quad (2.7)$$

where $V(r)$ is the nuclear potential which excites both nuclei. This expression can be simplified to:

$$[\nabla^2 - U(r) + k^2] \psi(r) = 0, \quad (2.8)$$

where $k = [2mE/\hbar^2]^{1/2}$ and $U(r) = 2mV(r)/\hbar^2$. Once a valid solution for ψ is found the differential cross section can be calculated using:

$$\frac{d\sigma}{d\Omega} = \frac{\mu_b}{\mu_a} |f(\theta)|^2, \quad (2.9)$$

where $\mu_{a,b}$ are the velocities of the incoming and outgoing channels respectively. The equations above are simplified, as they neglect the fact the nucleus has internal structure. When accounting for the structure such as the internal degrees of freedom of the colliding particles it can become difficult to find wavefunctions which are exact solutions to the Schrödinger equation [49]. To account for the internal structure of

the nucleus, different models and assumptions must be used. For the case of transfer reactions the model which is often used is the Distorted Wave Born Approximation (DWBA).

2.2.1 DWBA

The DWBA is a common tool for calculating angular distributions for transfer reactions. The Born approximation states that if the interaction strength is weak compared to the total energy of the system, the interaction can be treated as a perturbation [51]. The order of the perturbation determines the number of steps in the reaction between the initial and final interaction. The Born approximation considers only single step first order perturbations.

The DWBA [50] is an extension of this where the scattering potential can be split into two parts U_1 and U_2 . If U_2 is weak in comparison to U_1 it can be treated as a perturbation. The exact form of χ which satisfies eq. (2.8) is unknown, however it can be replaced with the wavefunction which solves Schrödinger's equation for the potential U_1 . The wavefunctions of the system are then not described in terms of plane waves, but the 'distorted wave' solution for U_1 .

In the DWBA the dominant process is elastic scattering with the other reaction channels expressed as perturbations. The wavefunction which describes elastic scattering can be obtained using an optical model potential which is described in section 2.2.1.2. With this wavefunction known the angular distributions for other reaction channels can be calculated.

The angular distributions obtained from DWBA calculations can then be compared to experimental data to determine the orbital angular momentum, ℓ , transferred. Due to the spin of the transferred particles it is not always possible to make definite J^π assignments. In this work proton transfer reactions are used which can populate levels with $J = \ell \pm 1/2$.

2.2.1.1 Spectroscopic Factors

When comparing DWBA calculations to experimental data it is clear that they overestimate the magnitude of the differential cross section. It is therefore necessary to normalise the DWBA calculations to match the experimental data [52]. The

normalisation factor is known as the spectroscopic factor, C^2S , and it is defined as:

$$\frac{d\sigma}{d\Omega_{exp}} = C^2 S \frac{d\sigma}{d\Omega_{DWBA}}, \quad (2.10)$$

where C is the isospin Clebsch-Gordon coefficient. As the DWBA assumes single step processes the calculations should not be scaled past the first minimum. This corresponds to a grazing collision, with higher angle scattering increasing the likelihood the reaction involves multiple steps [53]. The spectroscopic factor describes the probability that the state being populated in the reaction can be well described as a isolated core plus a single nucleon. The transfer of a particle to a double closed shell nucleus matches this description and a spectroscopic factor ~ 1 would be expected. A well known case is the transfer of a neutron to an ^{16}O nucleus which is found to have spectroscopic factor of 0.9 for the transfer to the ^{17}O ground state, which is the largest known measured value [54]. If the spectroscopic factor is < 1 , this implies that the reaction has been hindered due to the need to rearrange nucleons to form the final state.

2.2.1.2 Optical Model Potential

The optical model is a simple scattering model in which the interaction of two many-body nuclei is modelled as two structureless bodies interacting via a simple potential, which varies only as a function of distance [55]. Where other interactions are possible they are treated as loss of the total elastic cross section. This absorption is accounted for by using a complex potential of the form:

$$\begin{aligned} U(r) = & -V_r f_{ws}(r, R_0, a_0) - iW_v f_{ws}(r, R_w, a_w) \\ & - iW_s(-4a_w) \frac{d}{dr} f_{ws}(r, R_w, a_w) \\ & - 2(V_{so} + iW_{so}) \left(-\frac{1}{r} \frac{d}{dr} f_{ws}(r, R_{so}, a_{so}) \right) \\ & + V_c. \end{aligned} \quad (2.11)$$

V and W refer to real and imaginary potentials with R and a being the radius and diffuseness parameters of these potential. The subscripts r, v, s, so and c refer to the real, volume, surface, spin orbit and Coulomb potentials respectively. These parameters can be obtained from elastic scattering data. The advantage of the optical model is that multiple sets of elastic scattering data can be fit to obtain a

set of parameters which vary smoothly as a function of A , Z and projectile energy. These global parameters are used in large-scale calculations [56,57] and for reactions where no experimental data is available.

2.2.2 FRESCO

The DWBA calculations of this work were performed using the coupled channel reaction code FRESCO [58]. FRESCO is a general purpose reaction code, written in Fortran 90, which can be used to model a variety of direct nuclear reactions including elastic, inelastic and transfer reactions. Calculations are performed by defining a number of parameters which FRESCO uses to construct and solve the Schrödinger equation. From this solution it is then possible to extract the required nuclear information such as the angular distributions for individual states.

The parameters which are required for a calculation can be divided into five parts, however certain reaction mechanisms such as elastic scattering do not require all the parameters to be defined. The set of parameters are:

General Parameters - These are required for all calculations and control how the code converges to a solution. These include the maximum values of angular momentum and radius considered in the calculation as well as step sizes. Also included in the general parameters are the beam energies for which the reactions are studied. The final set of parameters are a series of switches which determine what information, such as cross-sections and matrix elements, are output at the end of the calculation.

Intrinsic Parameters - These are specific for the reaction being studied and describe the beam and target nuclei, before and after the collision. Nuclear properties such as mass and spin parity must be defined as well as any states involved in the reaction.

Nuclear Potentials - The parameters used here define the potentials which are used for the reaction calculation. The potentials used are taken as optical potentials, section 2.2.1.2, and are separated into coulomb, volume, surface and spin orbit potential terms. For each type of potential used a real and imaginary term must be included for the potential depth, V_0 and the radius and diffuseness parameters R and a . Also included are the shape of the volume potential, which can be defined as a Woods-Saxon or Gaussian potential. It is also possible to define any other shape

of potential.

Overlap Functions - Where a calculation requires single particle excitations to be performed, such as inelastic scattering or transfer, parameters must be included to construct overlap functions. The overlap function is a description of the composite nucleus looks relative to its core. As with spectroscopic factors, section 2.2.1.1, the overlap functions describe how the final state looks like a core plus a single nucleon. Here the spin and angular momentum of the transferred particles must be defined as well as a description of which nuclear orbitals must be populated.

Coupling Parameters - These describe the type of coupling between the initial and final states. Simply this describes the method in which the final state is populated whether through an electromagnetic interaction, a single particle excitation of the beam or target nuclei or a particle transfer. For a transfer reaction it is also possible to include the type of transfer coupling which includes; zero range, local energy approximation, finite range or a non-orthogonality correction to the previous transfer types. It is also possible to include couplings in the reverse direction.

FRESCO calculations are performed in this work to extract differential cross sections. Individual calculations are performed for each spin transfers depending on the type of reaction, for example the ($^3\text{He},d$) reaction involves low spin transfer so calculations are performed for $\ell = 0-3$. These calculations can then be compared to experimental angular distributions in order to extract spin and parity as well as proton transfer spectroscopic factors. Descriptions of the calculations performed for the $^{34}\text{S}(^3\text{He},d)^{35}\text{Cl}$ and $^{26}\text{Mg}(^3\text{He},d)^{27}\text{Al}$ reactions will be discussed in detail in sections 4.4 and 6.4 respectively. In addition as a test of the DWBA calculations used in this work a replication study was performed which can be found in Appendix A.

2.3 Gamow Window

For a nuclear reaction to occur classically the colliding particles must have sufficient energy to overcome the Coulomb barrier. Quantum mechanically, however there is a possibility that the colliding particles can tunnel through the Coulomb barrier and the reaction can occur unhindered. The probability for a particle to tunnel through

a Coulomb potential is given by the expression:

$$P_g(E) = e^{-\sqrt{\frac{E_g}{E}}}, \quad (2.12)$$

where E_g is the Gamow factor:

$$E_g = 4\pi^2\eta^2 E, \quad (2.13)$$

with η being the Sommerfeld parameter:

$$\eta = \frac{Z_1 Z_2 e^2}{\hbar v}, \quad (2.14)$$

where $Z_1 Z_2 e^2$ is the product of charges of the colliding particles. From eq. (2.12) it can be seen the probability of penetration of the Coulomb barrier is energy dependent with high energy particles most likely to penetrate the barrier. In an astrophysical environment, the particles will have a range of energies governed by a Maxwell-Boltzmann distribution:

$$f(E) = \sqrt{\frac{8}{\pi m (k_B T)^3}} E e^{-\frac{E}{k_B T}}. \quad (2.15)$$

The probability a nuclear reaction will occur is dependent upon the product of eqs. (2.12) and (2.15). The product of these equations, known as the Gamow distribution can in seen in Figure 2.3. Also shown are the separate Maxwell-Boltzmann distribution (dashed black line) and penetrability factor (dashed-dotted line). It can be seen clearly that if the energy of the particles is too low they cannot penetrate the barrier, but if the energy is too high there is insufficient numbers of particles for the reaction to occur. There is, however, a small energy region, known as the Gamow window [53] for which nuclear reactions are most likely to occur and is defined by:

$$E = E_0 \pm \frac{\Delta}{2}, \quad (2.16)$$

where E_0 is the Gamow peak:

$$E_0 = \left(\frac{E_g k_B^2 T^2}{4} \right)^{\frac{1}{3}} \quad (2.17)$$

and Δ is the Gamow width:

$$\Delta = \frac{4}{3^{1/2}}(E_0 k_B T)^{1/2}. \quad (2.18)$$

Resonances which lie within the Gamow window are the most important during astrophysical reactions. The contribution of individual states to the reaction rate is discussed in section 2.4

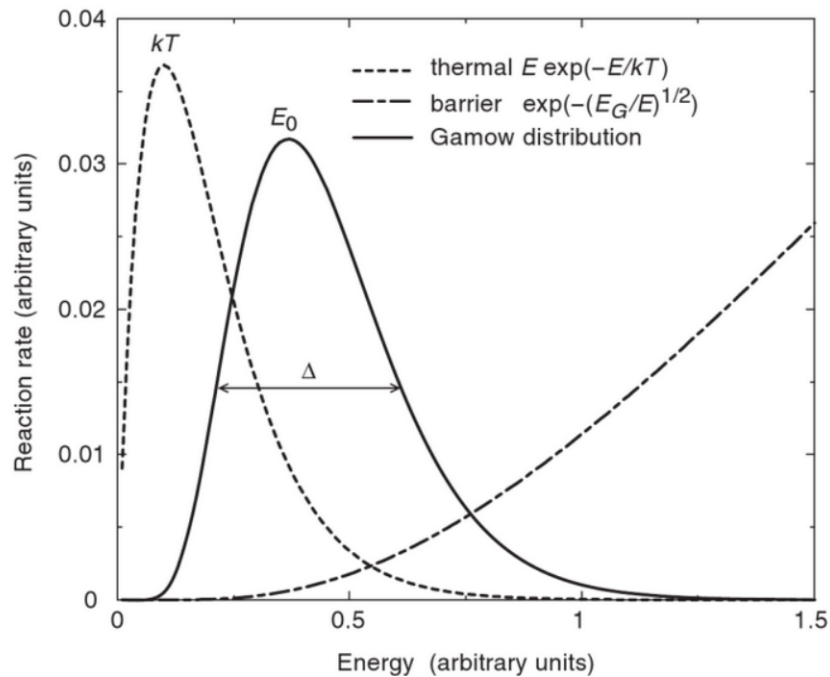


Figure 2.3: Dependence of the reaction cross section for charged particles as a function of energy (arbitrary units) [53]. The probability for a reaction to occur, the Gamow distribution (solid black line), is the product of the Maxwell-Boltzmann distribution (dashed line) and penetrability factor (dashed-dotted line).

2.4 Thermonuclear Reaction Rates

The thermonuclear reaction rate describes the number of reactions between two nuclei in a thermonuclear environment per second. The formalism for the reaction rate used in this work was detailed recently by Iliadis [1,59] and has been summarised

below. The thermonuclear reaction rate is given as:

$$N_A \langle \sigma \nu \rangle = \frac{3.7138 \times 10^{10}}{T_9^{3/2}} \sqrt{\frac{m_a + m_b}{m_a m_b}} \int_0^\infty E \sigma(E) e^{-\frac{11.605E}{T_9}} dE \quad \text{cm}^3 \text{mol}^{-1} \text{s}^{-1} \quad (2.19)$$

and describes the number of nuclear reactions per unit volume and time per mole of material. N_A is the Avogadro constant and $\langle \sigma \nu \rangle$ is the reaction rate per particle pair. It can be seen that the reaction is dependent upon both nuclear properties, contained within $\sigma(E)$ and the temperature T_9 which is units of GK (10^9 K). The temperature of the astrophysical environment determines the kinetic energy of the colliding particles as described by the Maxwell Boltzmann distribution. The parameter $\sigma(E)$ describes how the cross section varies as a function of energy. This parameter does not necessarily vary smoothly as a function of energy and is made of multiple contributions which must be combined to calculate the cross section. The multiple contributions required to calculate the reaction rate will be discussed in the following sections.

2.4.1 Non-Resonant Reaction Rate

Non-Resonant contributions to the cross section are found to vary smoothly as a function of energy at high energies. At low energies the probability of interaction is decreased several orders of magnitude due to the presence of the Coulomb barrier. The cross section due to non-resonant contributions is often given as:

$$\sigma(E) = \frac{1}{E} e^{-\frac{E_g}{E}} S(E), \quad (2.20)$$

where $S(E)$ is the astrophysical S factor. $S(E)$ is a useful parameter as it contains the energy dependent nuclear effects to the cross section and removes the dependence due to the Coulomb barrier. This parameter varies smoothly with energy and so can be approximated as a polynomial:

$$S(E) \simeq S(0) + S'(0)E + S''(0)E^2. \quad (2.21)$$

2.4.2 Resonant Reaction Rate

The following contributions to the reaction rate proceed with resonances within the nuclei of interest. It is therefore necessary to first describe what a resonance is and how its properties influence the reaction rate.

2.4.2.1 Resonances

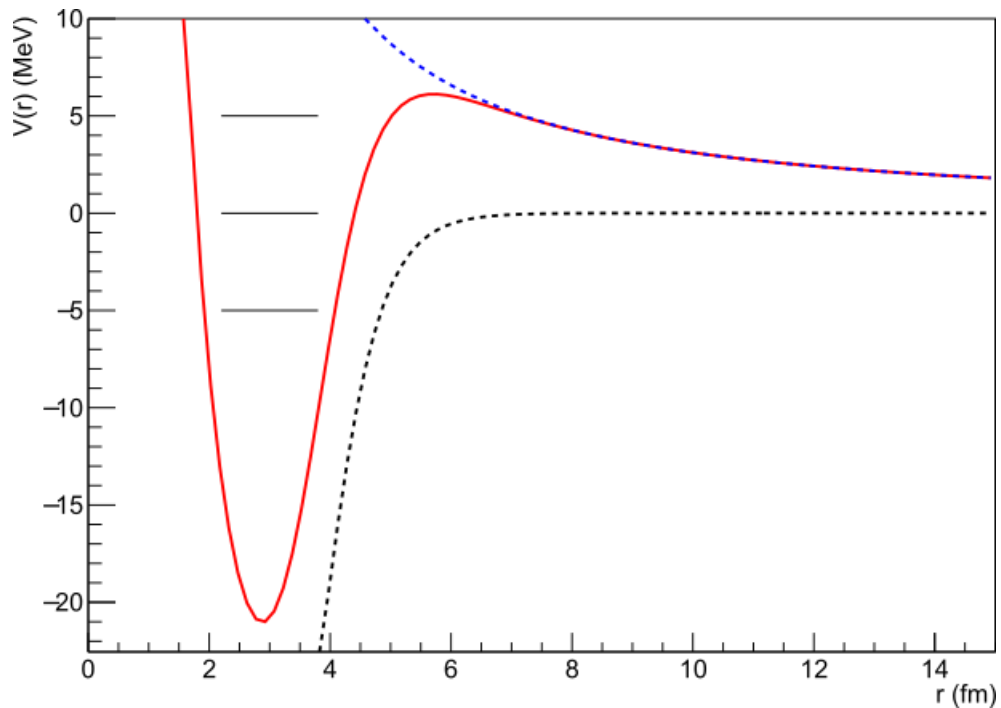


Figure 2.4: Graph showing a neutron resonance in a potential well in ^{27}Al . Shown as a dashed black line is a Woods-Saxon potential, with the dashed blue showing a centripetal potential and the solid red line showing the total potential. A particle can populate states within this well represented as a solid black lines. A resonance is a state which would be unbound to the nuclear potential (dashed black line), but can exist due to the angular momentum barrier (dashed blue).

A resonance is a ‘nearly bound’ state, which exhibits discrete quantum numbers despite being unstable against particle emission. A resonance is unbound to the nuclear potential barrier, however can exist due to extra binding from coulomb and centripetal effects as seen in Figure 2.4. The lifetime of these resonances are typically orders of magnitude greater than the orbital period of a nucleon $\sim 10^{-22}$ s [49], however the nucleon within this resonance state can eventually tunnel through the potential and decay through particle emission. A resonance can be described by

three parameters, the resonance energy, the lifetime and width Γ which is related to the lifetime τ through the uncertainty principle:

$$\Gamma \geq \frac{\hbar}{\tau} \quad (2.22)$$

Each of the available decay paths (p,n, α , γ) have their own partial widths Γ_i which contribute to the total width Γ . The partial widths themselves describe the probability of a state decaying through a certain channel. In order for the particle to decay it must first tunnel through the potential barrier. The penetrability through this barrier is calculated using:

$$P_l = R \left(\frac{k}{F_l^2 + G_l^2} \right), \quad (2.23)$$

where F_l and G_l are the regular and irregular Coulomb wave function and k is the channel wave number [60]. The widths are also dependent upon the single particle reduced width θ_{sp} which is the probability that the particle is emitted at the nuclear surface. Values of θ_{sp} for specific orbitals are computed using a suitable nuclear potential [61]. Finally the partial widths are dependent upon the value C²S which is a combination of the isospin Clebsch-Gordan coefficient C² and single particle spectroscopic factor S. The partial widths is calculated using:

$$\Gamma_i = \frac{2\hbar^2}{\mu r^2} C^2 S P_l \theta_{sp}^2, \quad (2.24)$$

where r is the interaction radius and μ is the reduced mass of the core + single particle system [59]. Using the partial widths and the spin of the resonance it is possible to define a new property known as the resonance strength $\omega\gamma$ which is defined as:

$$\omega\gamma = \frac{2J_r + 1}{(2J_p + 1)(2J_T + 1)} \frac{\prod \Gamma_i}{\Gamma_{Tot}}. \quad (2.25)$$

The resonance strength takes into account all nuclear structure information for the resonance which is needed to calculate $N_A \langle \sigma \nu \rangle$.

2.4.2.2 Narrow Resonant Reaction Rate

The presence of a resonance results in a large increase in the total cross section. For narrow resonances in which the Maxwell Boltzmann factor $e^{-\frac{E}{kT}}$ is constant

over the width of the resonance. The cross section, $\sigma(E)$ in eq. (2.19), can then be approximated as the sum of all narrow resonances with the total reaction rate calculated using:

$$N_a \langle \sigma v \rangle = 1.5399 \times 10^{10} (\mu T_9)^{-3/2} \sum_i (\omega \gamma)_i e^{-\frac{11.605 E_i}{T_9}} \text{cm}^3 \text{mol}^{-1} \text{s}^{-1}, \quad (2.26)$$

where μ is the reduced mass and the subscript i refers to individual resonances [1, 59].

2.4.2.3 Broad Resonance Reaction Rate

Equation (2.26) becomes invalid when the widths of the resonant states become broad. The Boltzmann factor and partial widths vary as a function of energy so cannot be assumed to be constant over the width of a broad resonant state. In addition if the Gamow window lies outside the resonance energy, contributions from the tail would be neglected from the reaction rate. The cross section for a broad resonance is calculated using a Breit-Wigner formula:

$$\sigma(E) = 0.6566 \frac{\omega}{E} \mu^{-1} \frac{\Gamma_a(E)^2 \Gamma_b(E + Q - E_f)^2}{(E_r - E)^2 + \Gamma(E)^2/4}, \quad (2.27)$$

where Q is the reaction Q-value, and E_f is the energy of the final state in the residual nucleus. This expression is used in place of $\sigma(E)$ in eq. (2.19) to calculate the reaction rate contribution of broad resonances.

2.4.2.4 Interference

If two broad resonances with the same spin overlap, their amplitudes will interfere. The contribution from the two resonances is given by:

$$\sigma(E) = \sigma_1(E) + \sigma_2(E) \pm 2\sqrt{\sigma_1(E)\sigma_2(E)} \cos(\delta_1 - \delta_2), \quad (2.28)$$

with σ_i obtained from eq. (2.27). δ_i is the resonance phase shift and is calculated using:

$$\delta_i = \arctan \left[\frac{\Gamma_i(E)}{2(E - E_{ri})} \right]. \quad (2.29)$$

2.4.3 Statistical Models

To understand the nuclear evolution of astrophysical events it is necessary to have reaction rates for many different reactions. While it is possible to measure some of these reaction rates through direct or indirect methods, many cannot be studied in current laboratory facilities. In place of rates based on experimental information, it is therefore necessary to use theoretical models to predict reaction rates. For the majority of astrophysical reactions the rates which are used are calculated using a Wolfenstein-Hauser-Feshbach approach [62, 63]. The main assumption of this approach is that there is a high level density of relevant resonances in the reaction energy range, typically 5-10 MeV⁻¹ [64]. While many reactions meet this criteria, lighter nuclei and those at shell closures or the drip lines do not reach sufficient level densities and the use of a statistical model is not ideal.

The statistical model reaction rates for the ³⁴S(p,γ)³⁵Cl and ²⁶Al(n,p/α) reactions, mentioned in sections 1.2.3 and 1.2.4 were calculated using the code NON-SMOKER. NON-SMOKER uses the level density of excited states and the particle and γ-transmission coefficients [43] in order to calculate reaction rates. The transmission coefficients describe an absorption via an imaginary optical potential, section 2.2.1.2, and represent a transition from an excited state in a compound nucleus to another state through the emission of a particle or γ ray. They are calculated as the sum of partial waves for all energetically favourable bound and unbound states. Particle transmission coefficients are calculated by solving the Schrödinger equation for an optical potential for the particle nucleus interaction [56,57]. The largest contribution to the γ-transmission coefficients are E1 and M1 transmissions. The E1 transition is the strongest of these and the contribution is calculated from a Lorentzian representation of a Giant Dipole Resonance [65], which is the bulk vibration of neutrons against protons in a nucleus.

The reaction rates derived from the NON-SMOKER are used in large scale nuclear astrophysics calculations where many reactions have not yet been measured. Sensitivity studies in particular use these rates to explore the effect of individual reactions to identify which are important for the chemical evolution of a stellar environment and as a result those which should be measured experimentally [6-8].

2.4.4 Reverse Reaction Rate

Nuclear reactions are not unidirectional and as long as it is energetically allowed to do so a reaction can proceed in forward and reverse directions. The extra kinetic energy of nuclei in a hot stellar environment allow for nuclear reactions to occur in both directions even if one has a negative Q value. To accurately predict nucleosynthesis yields it is necessary to include all reactions in both directions.

Rather than measure all reactions in both directions however, it is possible to calculate the reverse rate of any reaction from the principle of detailed balance. This requires the transition probabilities for the forward and reverse reactions to be equal. In stellar environments the forward and reverse reactions will reach an equilibrium and at this point the transition probabilities will be equal. As this will satisfy the principle of detailed balance it is then possible to relate the two reaction rates using,

$$\frac{N_a \langle \sigma \nu \rangle_{CD \rightarrow AB}}{N_a \langle \sigma \nu \rangle_{AB \rightarrow CD}} = \frac{(2J_A + 1)(2J_B + 1)}{(2J_C + 1)(2J_D + 1)} \cdot \left(\frac{G_A G_B}{G_C G_D} \right) \cdot \left(\frac{A_A A_B}{A_C A_D} \right)^{3/2} \cdot e^{-11.605Q/T_9}, \quad (2.30)$$

where Q is the reaction Q-value for the forward reaction and G_i is the temperature-dependent normalized partition functions which is defined as,

$$G_i = \sum_{\mu} \frac{(2J_{i\mu} + 1)}{(2J_{i0} + 1)} e^{-E_{i\mu}/kT} \quad (2.31)$$

where $J_{i\mu}$ and $E_{i\mu}$ are the spin and excitation energy of state μ in nucleus i and J_{i0} is the ground-state spin of nucleus i [26]. For the case of a capture reaction, $A(B,\gamma)D$, the reverse reaction will be photodissociation and the transition rate for this can be calculated using,

$$\begin{aligned} \frac{\lambda_{C\gamma \rightarrow AB}}{N_a \langle \sigma \nu \rangle_{AB \rightarrow C\gamma}} &= 9.685 \times 10^9 T_9^{3/2} \cdot \frac{(2J_A + 1)(2J_B + 1)}{(2J_C + 1)} \\ &\cdot \left(\frac{G_A G_B}{G_C} \right) \cdot \left(\frac{A_A A_B}{A_C} \right)^{3/2} \cdot e^{-11.605Q/T_9}, \end{aligned} \quad (2.32)$$

where λ is the number of photodissociations per second.

2.4.5 Reaction Rates Involving Excited Nuclei

Equation (2.19) is valid only if the reacting nuclei are in their ground states. While this assumption is valid for reactions measured in the lab, in stellar environments the high temperatures make it possible for the reacting nuclei to be thermally excited. If the ground state and excited state of the reacting nuclei have different spin values they will preferentially populate different states. A example of this is transferring a neutron to ^{26}Al . The ground state and first excited state have spin parity values of 5^+ and 0^+ respectively. Due to the presence of angular momentum barriers, neutron transfer reactions on the ground state of ^{26}Al will preferentially populate high spin states in ^{27}Al whereas low spin states would be populated if ^{26}Al was in its excited state. To account for these effects the reaction rate must be corrected by a Stellar Enhancement Factor (SEF) [66]. The SEF is defined as,

$$SEF = \frac{\langle \sigma^* \nu \rangle}{\langle \sigma \nu \rangle}, \quad (2.33)$$

where σ is the cross section assuming ground state reactions only and σ^* is the cross section in the stellar environment where reactions can occur on excited states. Values of SEF for nuclei close to stability can be found in data tables [43].

Chapter 3

Munich Experimental Setup

The reactions described in chapter 1 were studied at the Maier-Liebnitz Laboratory in Garching, Munich. Beams of ${}^3\text{He}$ and α particles were accelerated using a 14 MV Tandem Van de Graaff accelerator and impinged on a variety of targets most importantly Ag^{34}S and ${}^{26}\text{MgO}$ targets. A full list of targets used in this work will be detailed in section 3.3.1. Reaction products were separated and analysed using the Munich Q3D magnetic spectrometer, which will be discussed in the following section.

3.1 Beam Production

The ${}^3\text{He}$ and α beams were produced by the MML tandem accelerator. An ion source is used to form ${}^3\text{He}^-$ and ${}^4\text{He}^-$ ions which are repelled into the accelerator due to a bias applied to the ion source. The negatively charged ions are attracted towards a high-voltage terminal located at the centre of the accelerator. Also located at the centre of the detector is a carbon foil which strips electrons from the ions forming ${}^3\text{He}^+$ and ${}^4\text{He}^+$ ions which are repelled by the high-voltage terminal out of the accelerator. This means that the central voltage is used twice. The energy of the ions will be from a combination of the voltage on the central terminal and the ion source with $E_{\text{Beam}} = 2qV_{\text{Terminal}} + qV_{\text{Source}}$ where q is the charge of the ions.

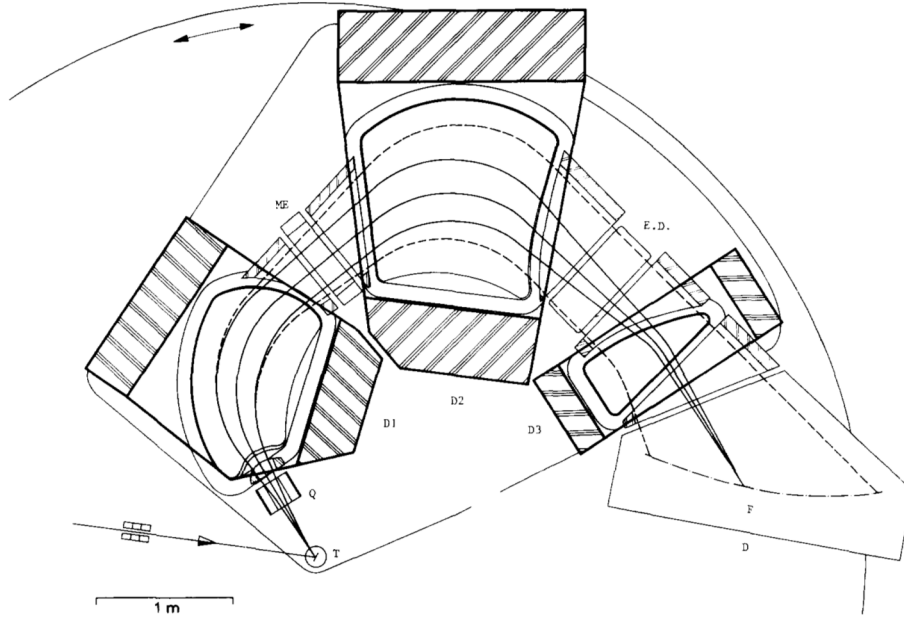


Figure 3.1: Ion optical layout of the Q3D spectrometer. T - target chamber; ME - multipole element; Q - quadrupole D1, D2, D3 - dipole magnets; E.D. - electrostatic deflector; F - focal plane; D - detector chamber [68].

3.2 Experiment Detectors

3.2.1 Munich Q3D Magnetic Spectrometer

The Munich Q3D Magnetic Spectrometer, hereafter referred to as the Q3D, is a charged particle spectrometer, consisting of a three dipole magnets, one quadrupole magnet and a single multipole magnet. A schematic of this spectrometer can be seen in Figure 3.1. The Q3D has a large solid angle acceptance, up to 14.7 msr^{-1} , which can be reduced to increase energy resolution at the expense of transmission. The Q3D is a high resolution spectrometer with a resolution of $\Delta E/E \sim 2 \times 10^{-4}$ [67] where E is the energy of the scattered particle. The Q3D can be rotated in order to study reaction products at different angles to extract angular distributions.

Reaction products are separated by magnetic elements within the detector and brought to focus on a common plane. Position along this focal plane can then be used to determine the energy of reacted particles. From reaction kinematics the energy of excited states in the target nuclei can be extracted. A description of the ion optics will be discussed in the following sections. Position and particle identification is determined using several detectors positioned at the focal plane and

will be discussed in section 3.2.2.

3.2.1.1 Dipole Magnets

A charged particle moving with velocity, \mathbf{v} , through a uniform magnetic field, \mathbf{B} , will experience a Lorentz force of the form:

$$\mathbf{F} = q(\mathbf{v} \times \mathbf{B}), \quad (3.1)$$

which for the case of a particle moving perpendicular to the field simplifies to:

$$F = qvB. \quad (3.2)$$

A particle experiencing this force will move in a circular orbit with radius ρ and will experience a centripetal force:

$$F = \frac{mv^2}{\rho}. \quad (3.3)$$

Combining eqs. (3.2) and (3.3) gives:

$$B\rho = \frac{mv}{q}, \quad (3.4)$$

where the quantity $B\rho$ is the magnetic rigidity. Particles with different momentum, will have different $B\rho$ and will follow different paths through the field as seen in Figure 3.2. Changing the field strength can be used select particles whose energies correspond to a excitation energy in the nuclei of interest.

3.2.1.2 Quadrupole Magnet

A quadrupole magnet consists of four poles arranged so that the field present at the centre is zero. A schematic of a quadrupole magnet with field lines can be seen in Figure 3.3. The magnetic field due to a quadrupole magnet is non-uniform with the field strength increasing radially outwards. A charged particle travelling through the top of the magnet will experience a force, eq. (3.1), directed towards the centre of the magnet. Similarly a particle travelling through the bottom of the magnet will be deflected towards the centre. Particles travelling through either the left or right of the magnet, will however experience a force directed away from the centre. It can therefore be seen that a quadrupole magnet focusses a beam of particles in

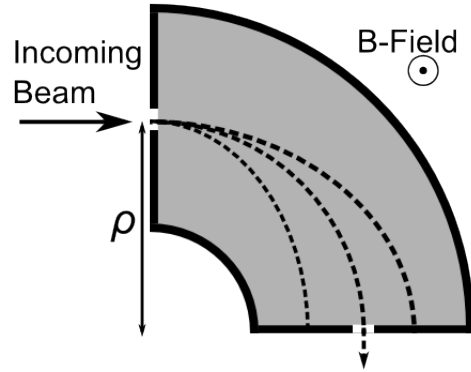


Figure 3.2: Diagram showing trajectory of charged particles through a dipole magnet. Magnetic Field strength can be adjusted to select isotopes with specific $B\rho$.

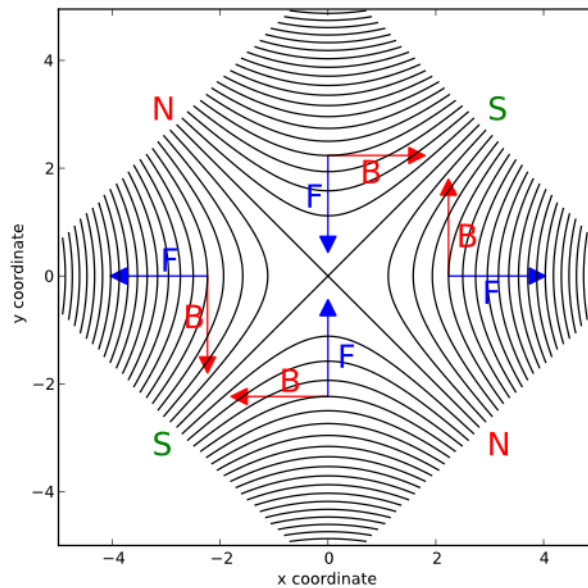


Figure 3.3: Diagram showing idealised magnetic field lines produced by a quadrupole magnet. Field lines are labelled assuming a particle moving into the page [69].

one direction while defocussing in the other. A quadrupole magnet is employed in the Q3D in order to improve the vertical acceptance of ions travelling through the detector.

3.2.1.3 Multipole Magnet

For wide angle magnetic spectrometers, kinematic broadening effects begin to become the dominant factor affecting the resolution of the detector [70]. For a reaction of the form A(B,C)D with particle A impinging on a target B, the Q value can be written as:

$$Q = E_C \left(1 + \frac{m_C}{m_D}\right) - E_A \left(1 + \frac{m_A}{m_D}\right) - \frac{2}{m_D} (E_A E_C m_A m_C)^{\frac{1}{2}} \cos \theta_{lab}. \quad (3.5)$$

Differentiating with respect to θ and rearranging it can be seen that:

$$\frac{1}{E_C} \frac{\partial E_C}{\partial \theta} = -\frac{100\pi}{180} \cdot \frac{2 \left(m_A m_C \frac{E_A}{E_C}\right)^{\frac{1}{2}} \sin \theta}{m_C + m_D - \left(m_A m_C \frac{E_A}{E_C}\right)^{\frac{1}{2}} \cos \theta} \quad (3.6)$$

Assuming a case of elastic scattering of α particles on a ^{12}C target at 90° eq. (3.6) simplifies to:

$$\frac{1}{E_C} \frac{\Delta E_C}{\Delta \theta} \simeq 1.2\% \text{ deg}^{-1}. \quad (3.7)$$

The result in equation eq. (3.7) is percent energy change per degree. It can be seen from this result that for a wide acceptance window $\Delta\theta$ this effect can be quite large.

In the Q3D this effect is reduced using a multipole magnet [68]. Kinematic broadening is to first order a defocussing effect so can be compensated by focussing in the horizontal plane. This focussing can be performed using a quadrupole magnet as described in section 3.2.1.2. From eq. (3.6) it can be seen that for heavy ion kinematics, where the beam has a greater mass than the target, there is greater kinematic broadening and larger corrections are required. The Q3D uses a multipole element, which produces simultaneous dipole, quadrupole, sextupole, octopole and hexapole fields. The multipole is placed at the vertical focus of the quadrupole field so that vertical focussing is not affected.

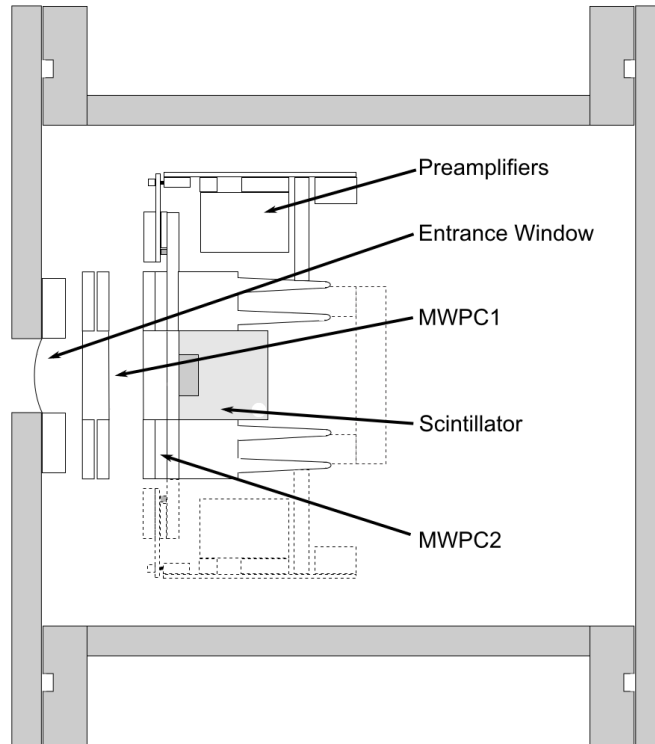


Figure 3.4: Side view schematic of the Q3D focal plane detectors. Particles enter from the left [71]

3.2.2 Focal Plane Detectors

The focal plane detectors of the Q3D are made up of three detectors, two MultiWire Proportional Counters (MWPC) and a plastic scintillator, the arrangement can be seen in Figure 3.4. The purpose of these detectors is to both detect position of the reacted particles and provide particle Identification (PID). Details of these detectors and their operation will be given in the following sections.

3.2.2.1 Scintillators

Scintillators are a class of detectors made of a variety of materials used to detect ionising radiation. The material choice greatly affects the scintillator performance, however all work on the principle of fluorescence. Ionising radiation excites electrons in the scintillating material, which proceeds to de-excite by the emission of visible light. The total number of photons produced is proportional to the energy of the incoming radiation. The choice of scintillating material is important in determining the light yields, photons per keV, and the response time, the delay between excitation

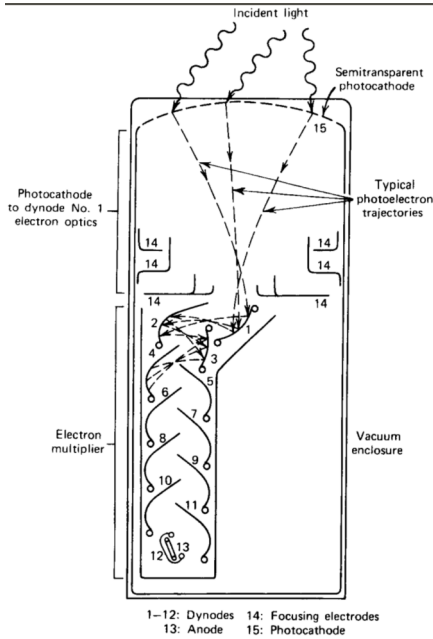


Figure 3.5: Basic elements of a Photomultiplier tube. [73]

and de-excitation [72]. The photons are collected by a PhotoMultiplier Tube (PMT) which outputs a current signal to measure the energy of the radiation. A simple PMT, as seen in Figure 3.5, is a vacuum tube consisting of a photocathode and an electron multiplier. The photocathode absorbs photons produced by the scintillating material, creating low energy photoelectrons. These electrons are then accelerated due to a bias applied across the PMT. The electrons collide with dynodes within the PMT producing a large number of electrons which are then accelerated and collected by an anode. In this way large signals can be produced from low photon yields. The Q3D uses a $7 \times 14\text{mm}^2$ Ne-104 plastic scintillator.

3.2.2.2 MultiWire Proportional Counter

A MWPC is a type of gas filled position sensitive detector. A basic proportional counter consists of an anode wire held at high voltage surrounded by a tube which acts as a cathode. Radiation collides with gas molecules within the detector, causing the formation of electron-ion pairs. Under normal conditions the electron-ion pairs will recombine, however the voltage difference between the anode and cathode creates an electron field which allows the electron and ions to drift to their respective electrodes [72]. For sufficiently high electric fields secondary ionisation can occur when the kinetic energy of the free electrons is sufficient to create another

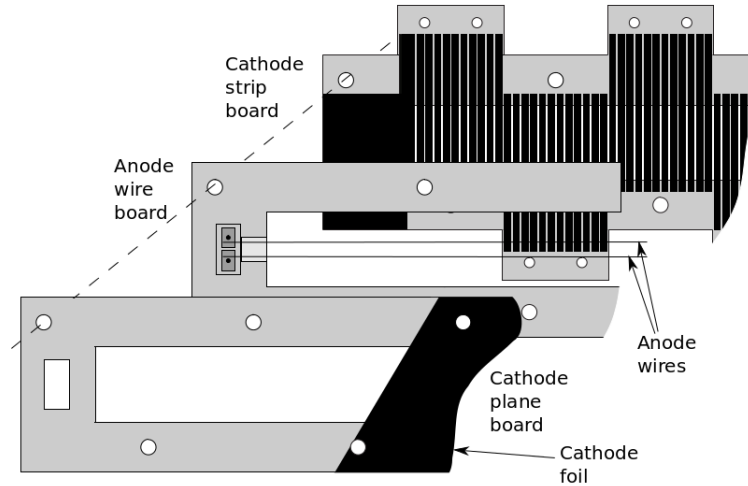


Figure 3.6: A schematic diagram of MWPC2. A side view can be seen in Figure 3.7 [71]

electron-ion pair. The electrons liberated by this ionisation are then accelerated by the electric field and cause further ionisation. This process is known as a Townsend Avalanche. The signal induced on the anode is proportional to the initial number of electron-ion pairs created and as a result the energy of the incident radiation.

The MWPC is a development of this design which uses multiple anode wires between two cathodes. As an ion passes through the detector it ionises the gas creating electron-hole pairs inducing signals on the anode wires as the electrons are accelerated by the electric field. Typically the signals collected by the anode wires are used to localise the original event.

Position along the Q3D focal plane is determined using MWPC2 as labelled in Figure 3.4, a detailed schematic can be seen in Figure 3.6. The MWPC consists of two anode wires running parallel across the focal plane between two cathodes. The back cathode is segmented and is used to determine position sensitivity as shown in Figure 3.7. As a particle enters the MWPC electrons are produced which drift towards the anode, inducing a charge across multiple cathode strips. Fitting the magnitude of the collected charge across multiple strips allows sub strip position resolution to be achieved.

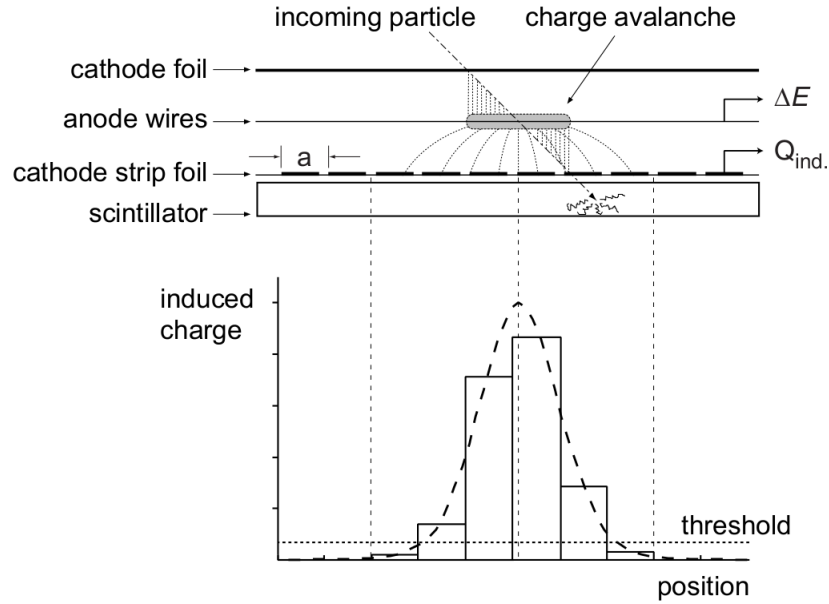


Figure 3.7: A schematic showing how focal-plane position of reaction products is determined using MWPC2 [71]

3.2.3 Particle Identification

Multiple reactions occur at the target position, with different reactions products able to scatter into the Q3D and implant on to the focal plane. The cross section for competing reactions may in some cases be several orders of magnitude greater than the reaction of interest. Reaction products must therefore be identified at the focal plane.

Using the method of differential energy loss and the focal plane detectors described in section 3.2.2 it is possible to identify products at the focal plane. For non relativistic velocities the energy loss of a charged particle through an absorber is given by the Bethe-Bloch formula [72]:

$$-\frac{dE}{dx} = \frac{4\pi e^2 Z_i^2}{m_e v^2} N_t Z_t \cdot \ln \left(\frac{2m_e v^2}{I} \right), \quad (3.8)$$

where Z_i and v are the atomic number and velocity of the ion; Z_t , I and N_t are the atomic number, mean excitation potential and number density of the absorber. The second term in eq. (3.8) varies slowly in energy so it can be seen that the energy loss will be dominated by the $1/v^2$ term or inversely proportional to energy. The

Bethe-Bloch formula can then be approximated as:

$$-\frac{dE}{dx} \propto \frac{Z_i^2 m_i}{E_i}. \quad (3.9)$$

From this equation it can be seen that energy loss of a charged particle travelling through a medium is dependent on its charge and mass. By measuring the energy deposited by a particle it is possible to distinguish between different particles. It is common to measure the energy deposited in multiple detectors in order to identify particles. In this work two methods are used to identify scattered particles.

The first method for Particle ID is the $\delta E/\delta E$ method, in which the charge collected in the two MWPCs is plotted against each other, this is shown in Figure 3.8 for the $^{26}\text{Mg}(^3\text{He},d)^{27}\text{Al}$ reaction. Two distinct loci are seen corresponding to deuterons and protons allowing a gate to be placed around the deuteron reaction products only. It should be noted that the anode bias was set to observe protons and deuterons, which means the inelastically scattered ^3He could not be gated on. It should be noted that the choice of gate used will affect the cross sections extracted in the work. If the gate is too small it will not be possible to select all of the deuterons and the cross sections extracted will be underestimated. A larger gate could be used, however this increases the chances that other reaction channels will be included and the gated spectrum will have higher contaminant levels. For the case of the gate used in Figure 3.8 it is likely that there are deuterons which are not included in this gate. While this would result in the extracted cross sections from being underestimated, the effect is likely smaller than other sources of uncertainty and can be ignored.

A second gate can also be placed using the $\delta E/E$ method. This method plots the partial energy deposition in one detector versus the total energy deposited in a second detector. Particles which deposit most of their energy in the first detector, will deposit little in a second and similarly if a particle deposits little energy in the first detector, more will be deposited in the second. For the Q3D the energy loss in the first MWPC is plotted against the energy deposited in the plastic scintillator. The result of this for the $^{26}\text{Mg}(^3\text{He},d)^{27}\text{Al}$ reaction can be seen in Figure 3.9.

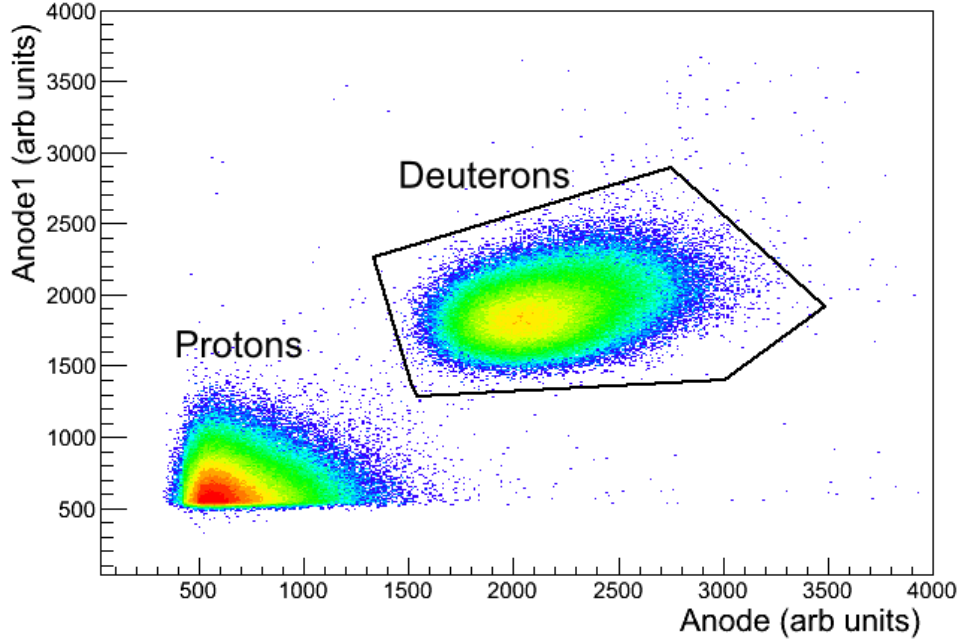


Figure 3.8: MWPC1 Anode charge versus MWPC2 Anode charge for ^3He nuclei impinging on ^{26}MgO target and scattered in to the Q3D at 5° . A gate is placed around the deuteron locus.

3.2.4 Focal Plane Calibration

To identify states the focal plane must first be calibrated. The focal plane is calibrated in terms of $B\rho$ which can then be converted to energy using eq. (3.4). This is accomplished by using isolated states with known $B\rho$. Programs are available which use reaction kinematics to predict the position of reacted particles for different states on a focal plane [74]. Specific states used in calibration for each reaction will be discussed in later sections. The focal plane can be calibrated at a single angle, with rigidities at other angles calculated using:

$$B_{exp}\rho = \frac{B_{exp}}{B_{ref}} \cdot f(x), \quad (3.10)$$

where B_{ref} is the magnetic field settings used in the calibration and B_{exp} is the field settings used for specific angle. $f(x)$ is a quadratic function converting focal plane position to radius of curvature ρ .

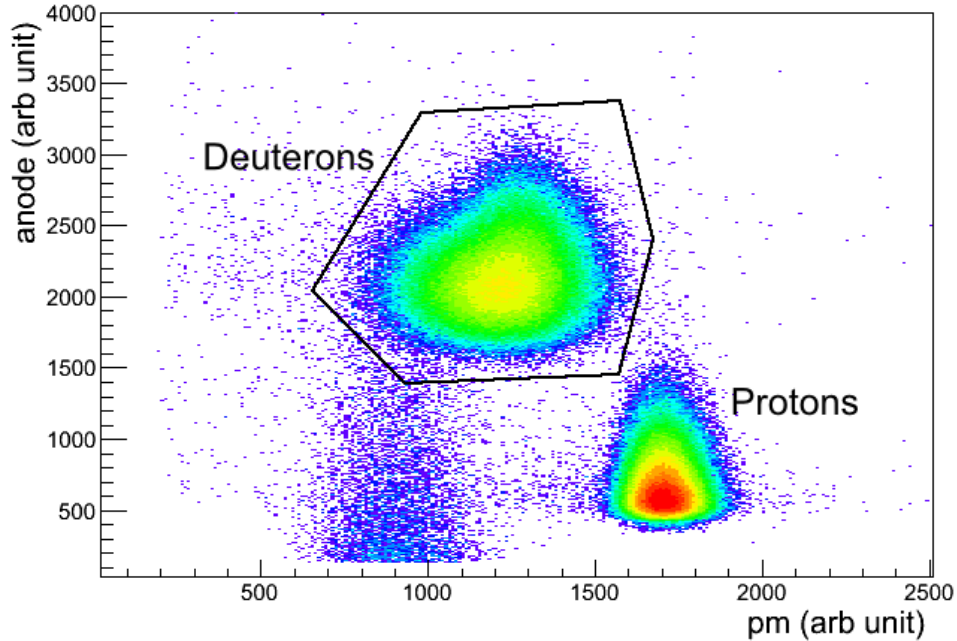


Figure 3.9: MWPC1 Anode charge versus Plastic Scintillator charge (pm) for ${}^3\text{He}$ nuclei impinged on ${}^{26}\text{MgO}$ target and scattered in to the Q3D at 5° . A gate is placed around the deuteron locus.

3.3 Experimental Details

3.3.1 Targets

The Q3D target ladder has space to accommodate up to five targets. A full list of targets used in this work can be seen in Tables 3.1 to 3.3. The ${}^{34}\text{S}({}^3\text{He},\text{d}){}^{35}\text{Cl}$ reaction was studied using an enriched $50\ \mu\text{g}/\text{cm}^2$ $\text{Ag}_2{}^{34}\text{S}$ target with $\text{Ag}_2^{\text{nat}}\text{S}$ and $\text{Zn}^{\text{nat}}\text{S}$ used to identify contaminant peaks. For the ${}^{26}\text{Mg}(\alpha,\text{t}){}^{27}\text{Al}$ and ${}^{26}\text{Mg}({}^3\text{He},\text{d}){}^{27}\text{Al}$ reactions, states in ${}^{27}\text{Al}$ were studied using isotopically enriched ${}^{26}\text{MgO}$ targets with a thickness of $20\ \mu\text{g}/\text{cm}^2$ and $50\ \mu\text{g}/\text{cm}^2$. Both targets were backed with $8\ \mu\text{g}/\text{cm}^2$ carbon. Natural MgO targets were used in both reactions to identify contamination from other Mg isotopes, with carbon targets used to identify contamination from the carbon backing. The experimental targets were made to a precision of 20% at the one sigma level which will be the used as the uncertainty in target thickness.

Table 3.1: Targets used to study the $^{34}\text{S}(^3\text{He},\text{d})^{35}\text{Cl}$ reaction. The thickness of the target is assumed to be precise up to 20% at the one sigma level.

Target Ladder Position	Target	Thickness
1	Collimator	-
2	$\text{Ag}_2^{34}\text{S} + \text{C Backing}$	$20\mu\text{g}/\text{cm}^2 + 8\mu\text{g}/\text{cm}^2$
3	$\text{Ag}_2^{\text{nat}}\text{S} + \text{C Backing}$	$50\mu\text{g}/\text{cm}^2 + 10\mu\text{g}/\text{cm}^2$
4	$\text{ZnS} + \text{C Backing}$	$40\mu\text{g}/\text{cm}^2 + 8.5\mu\text{g}/\text{cm}^2$
5	$\text{Ag}_2^{\text{nat}}\text{S} + \text{C Backing}$	$43.2\mu\text{g}/\text{cm}^2 + 10\mu\text{g}/\text{cm}^2$
6	^{12}C	$40\mu\text{g}/\text{cm}^2$

Table 3.2: Targets used to study the $^{26}\text{Mg}(\alpha,\text{t})^{27}\text{Al}$ reaction. The thickness of the target is assumed to be precise up to 20% at the one sigma level.

Target Ladder Position	Target	Thickness
1	Collimator	-
2	$^{26}\text{MgO} + \text{C Backing}$	$20\mu\text{g}/\text{cm}^2 + 8\mu\text{g}/\text{cm}^2$
3	$^{26}\text{MgO} + \text{C Backing}$	$50\mu\text{g}/\text{cm}^2 + 8\mu\text{g}/\text{cm}^2$
4	SiO	$25\mu\text{g}/\text{cm}^2$
5	$\text{ZnS} + \text{C Backing}$	$50\mu\text{g}/\text{cm}^2 + 8\mu\text{g}/\text{cm}^2$
6	$^{\text{nat}}\text{C}$	$22.8\mu\text{g}/\text{cm}^2$

Table 3.3: Targets used to study the $^{26}\text{Mg}(^3\text{He},\text{d})^{27}\text{Al}$ reaction. The thickness of the target is assumed to be precise up to 20% at the one sigma level.

Target Ladder Position	Target	Thickness
1	Collimator	-
2	$^{26}\text{MgO} + \text{C Backing}$	$20\mu\text{g}/\text{cm}^2 + 8\mu\text{g}/\text{cm}^2$
3	$^{26}\text{MgO} + \text{C Backing}$	$50\mu\text{g}/\text{cm}^2 + 8\mu\text{g}/\text{cm}^2$
4	$^{24}\text{MgO} + \text{C Backing}$	$40\mu\text{g}/\text{cm}^2 + 8.6\mu\text{g}/\text{cm}^2$
5	$^{\text{nat}}\text{C}$	$27.8\mu\text{g}/\text{cm}^2$
6	SiO	$25\mu\text{g}/\text{cm}^2$

Chapter 4

$^{34}\text{S}(^3\text{He},\text{d})^{35}\text{Cl}$ Analysis and Results

The $^{34}\text{S}(^3\text{He},\text{d})^{35}\text{Cl}$ reaction was studied at the MLL facility in Garching using the Q3D magnetic spectrometer. A beam of 20 MeV ^3He nuclei were accelerated by a tandem accelerator and impinged on the targets listed in Table 3.1. Scattered particles were analysed at the focal plane of a Q3D magnetic spectrometer. Reaction products were measured at 5 angles, 5, 10, 15, 25, and 40 degrees, with respect to the beam axis, with the aim of measuring angular distributions. Spin parity values and spectroscopic factors were then extracted and used to calculate a new $^{34}\text{S}(p,\gamma)^{35}\text{Cl}$ reaction rate at nova temperatures. In this chapter the results and techniques required to extract them will be detailed. The implications of these results will be discussed in chapter 5.

4.1 Focal Plane Identification

In order to identify states in ^{35}Cl a gate must first be placed to identify the deuteron reaction channels. Using the focal plane detectors and the δE versus δE method a deuteron spectrum is obtained. The spectrum at 5° for the Ag_2^{34}S target can be seen in Figure 4.1. It is clear that the $(^3\text{He},\text{d})$ reaction channel is dominant with few states from other reaction channels seen at the focal plane. A further gate can also be placed using the δE versus E method, however this does not have a measurable effect given the cleanliness of the spectrum. With the deuteron peaks identified

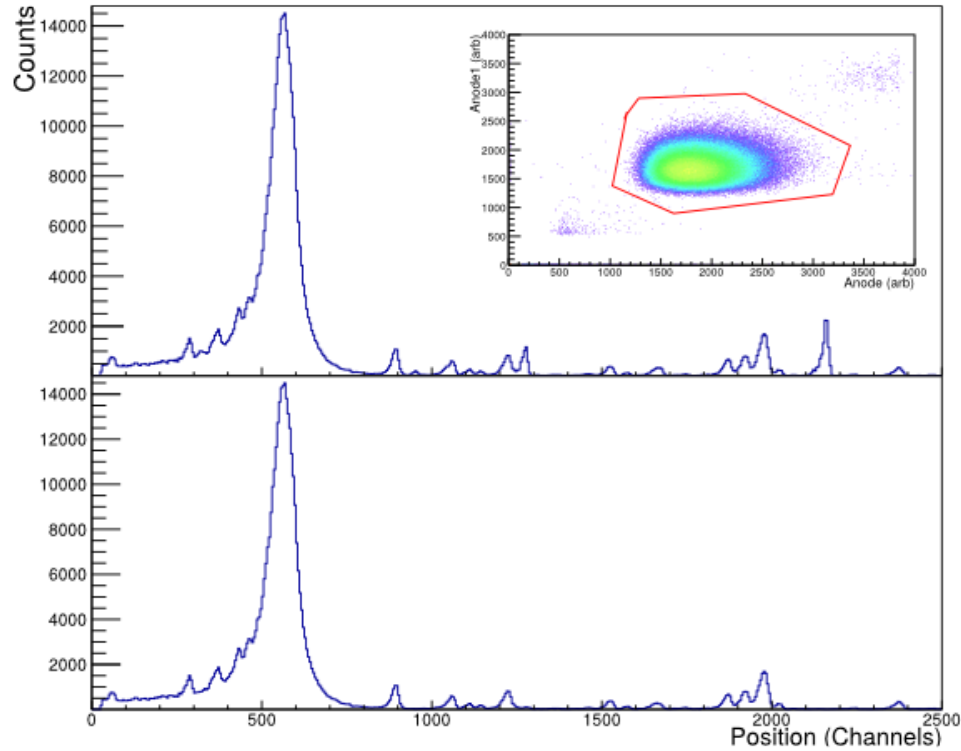


Figure 4.1: Focal plane spectrum for Ag_2^{34}S at 5° . Top - Ungated focal plane spectrum showing all reaction products. Inset - MWPC1 Anode charge versus MWPC2 Anode charge, a gate is placed around the deuteron locus. Bottom - Deuteron gated focal plane spectrum for Ag_2^{34}S at 5° . Peaks seen in this spectrum are due to $(^3\text{He},d)$ reactions on target 2 in Table 3.1.

it is necessary to identify those state which are from reactions on ^{34}S nuclei. The Ag_2^{34}S target used was carbon backed so a separate natural carbon target was used to identify any states from reactions on $^{12,13}\text{C}$. While an enriched target was used a certain amount of ^{nat}S will be present in the target with states from reactions on ^{32}S being the most prevalent of other sulphur isotopes based on the natural abundances. Several ^{nat}S targets were available for this study and were trialled in order to identify the one with the strongest sulphur composition. Reactions on two $\text{Ag}_2^{nat}\text{S}$ targets and a Zn^{nat}S target were initially measured at 5° . The Zn^{nat}S target was shown to have the highest reaction count rate at 5° and was chosen to be used at the other measurement angles.

Figures 4.2 to 4.6 shows the overlay of the Ag_2^{34}S , $\text{Zn}_2^{nat}\text{S}$ and ^{nat}C targets at all angles, which allows for the identification of the contaminant states. Using the code nukestim [74], which uses reaction kinematics to predict the expected position of reaction products on a focal plane, these states can be identified and are marked

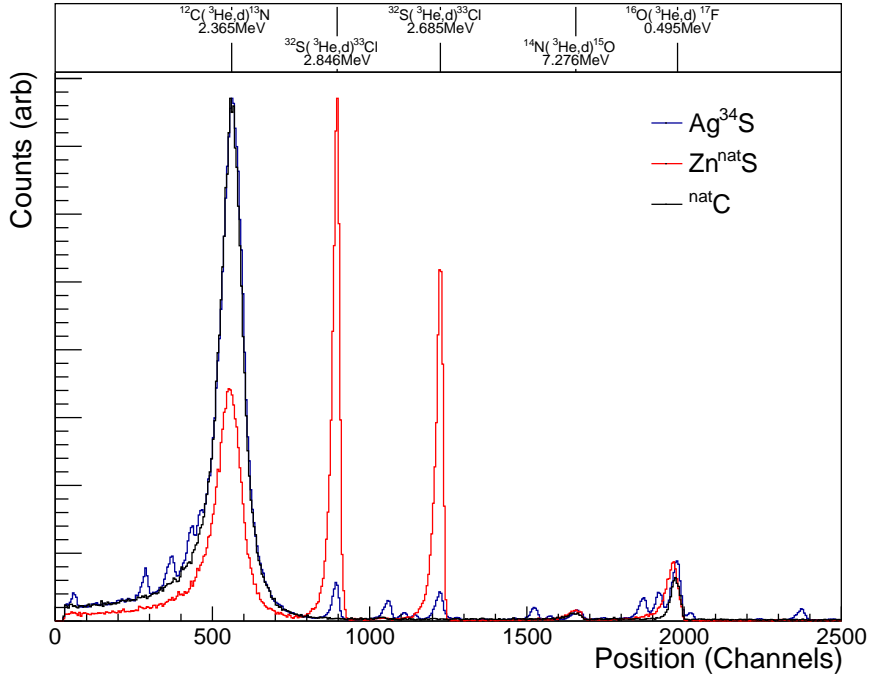


Figure 4.2: Bottom - 5° focal plane spectra for Ag_2^{34}S , $\text{Zn}_2^{\text{nat}}\text{S}$ and $^{\text{nat}}\text{C}$ targets. The spectra have been scaled to appear on the same axis. Top - Predicted position of states on the Q3D focal plane from the nukesim code [74].

in the top panel of Figure 4.2. It should be noted that these predictions are for a split-pole spectrometer and should not be taken as exact positions. It should be noted that the 2.846 MeV state in ^{33}Cl is not a singlet. The resolution of previous ($^3\text{He,d}$) studies [75, 76] was insufficient to resolve a state at 2.839 MeV which has been identified in later studies using (p,γ) reactions [77–79]. Given the expected energy resolution of the Q3D spectrometer it may be possible to identify this state when fitting the focal plane data.

4.2 Focal Plane Fitting

Before fitting the focal plane spectra several corrections must first be performed. High count rates result in dead-time losses which must be accounted for in order to extract accurate cross sections. These dead-time losses are recorded in the first bin of the focal plane histograms and can be corrected for using:

$$T_{\text{Dead}} = \frac{\text{All Counts in Spectrum}}{(\text{All Counts} - \text{Counts in Channel } 0)}. \quad (4.1)$$

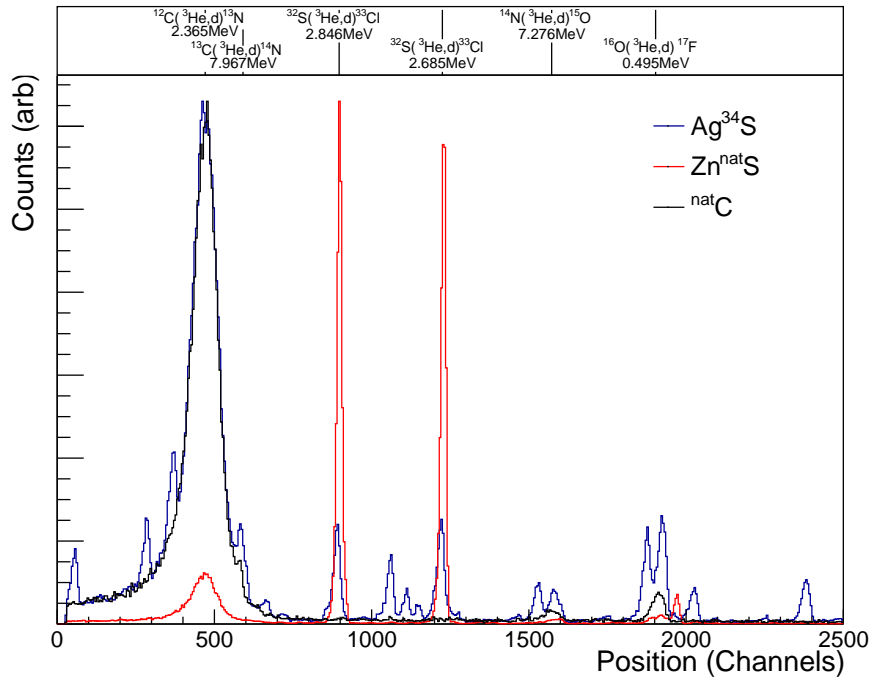


Figure 4.3: Bottom - 10° focal plane spectra for Ag_2^{34}S , $\text{Zn}_2^{\text{nat}}\text{S}$ and $^{\text{nat}}\text{C}$ targets. The spectra have been scaled to appear on the same axis. Top - Predicted position of contaminant states on the Q3D focal plane from the nukesim code [74].

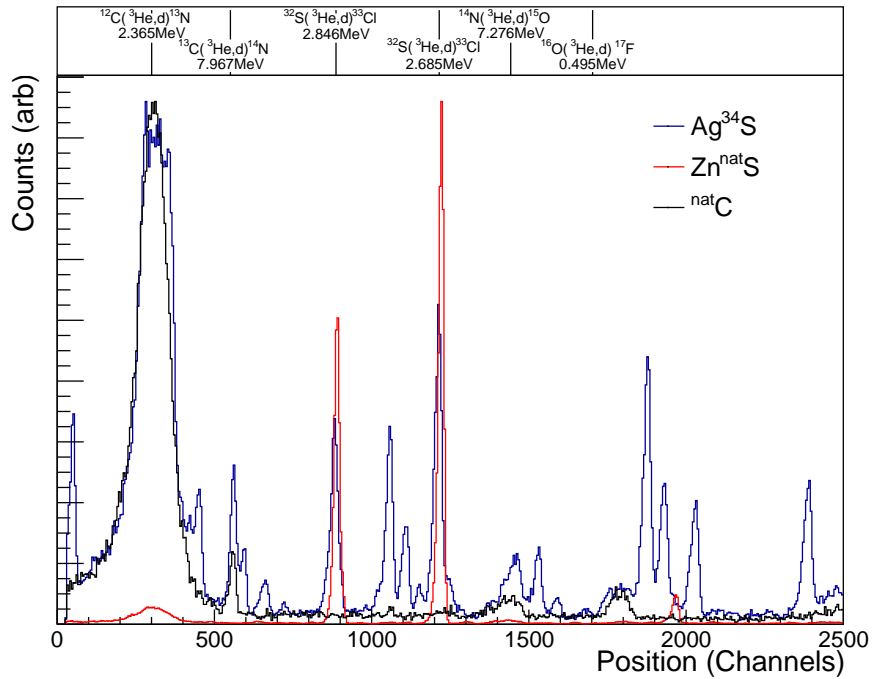


Figure 4.4: Bottom - 15° focal plane spectra for Ag_2^{34}S , $\text{Zn}_2^{\text{nat}}\text{S}$ and $^{\text{nat}}\text{C}$ targets. The spectra have been scaled to appear on the same axis. Top - Predicted position of contaminant states on the Q3D focal plane from the nukesim code [74].

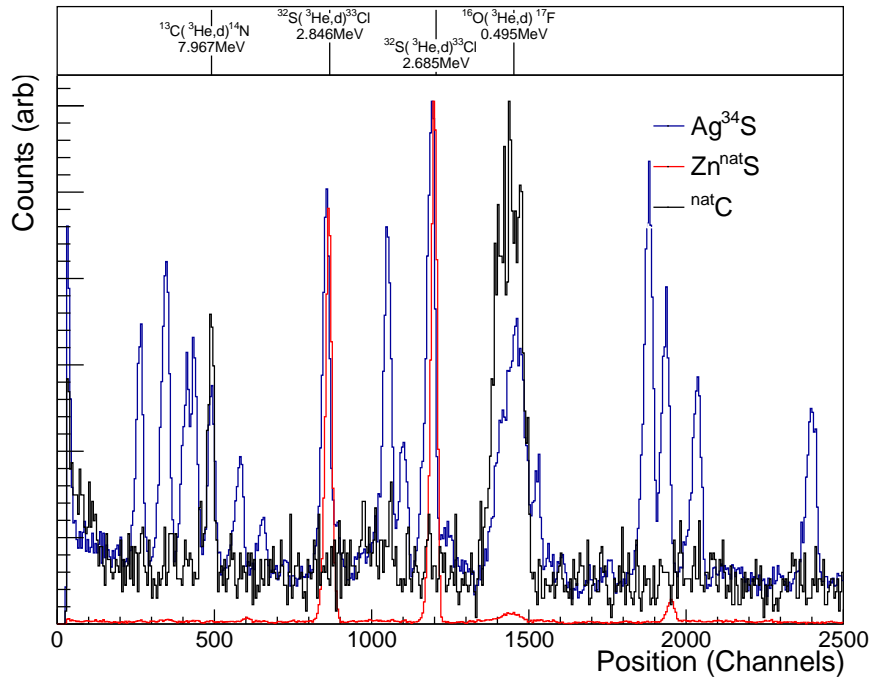


Figure 4.5: Bottom - 25° focal plane spectra for Ag_2^{34}S , $\text{Zn}_2^{\text{nat}}\text{S}$ and natC targets. The spectra have been scaled to appear on the same axis. Top - Predicted position of contaminant states on the Q3D focal plane from the nukemim code [74].

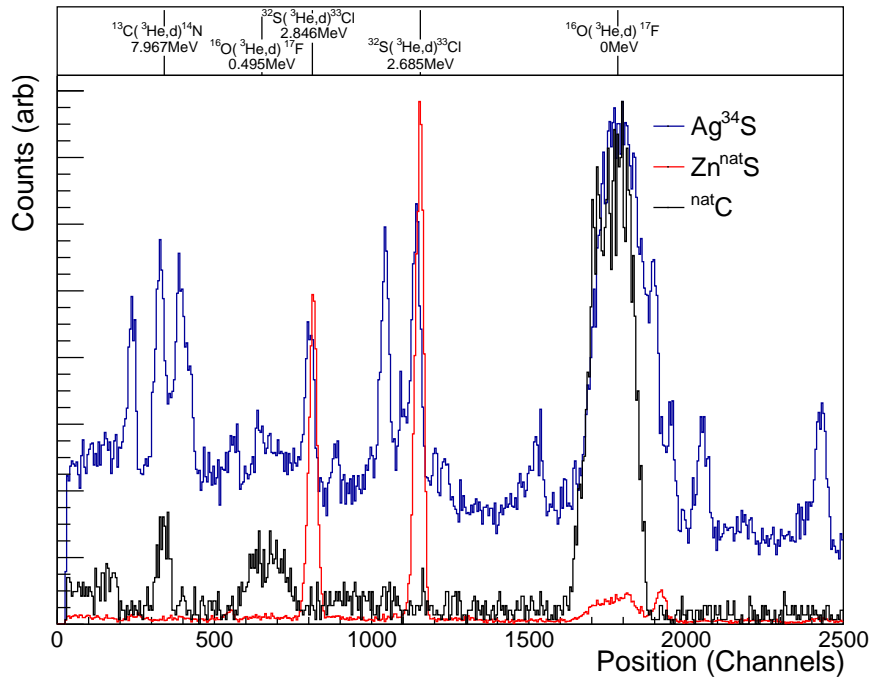


Figure 4.6: Bottom - 40° focal plane spectra for Ag_2^{34}S , $\text{Zn}_2^{\text{nat}}\text{S}$ and natC targets. The spectra have been scaled to appear on the same axis. Top - Predicted position of contaminant states on the Q3D focal plane from the nukemim code [74].

This is a measure of the amount of time the detector was inactive and so not recording true events. The focal plane spectra be corrected by this value to correct for the dead time losses. In this work these are negligible.

The spectra must also be normalised by the total beam current accumulated during the run. As explained in Chapter 3 a Faraday cup is placed behind the target ladder. This is connected to a Beam Current Integrator which outputs a signal which is proportional to the total beam current. The current is read out as two scalar values SCA1/SCA3 which can be used to calculate the total beam current using:

$$Q = \frac{SCA1 - SCA3}{1000} * 2 \times 10^{-6}, \quad (4.2)$$

where the factor 2×10^{-6} is the equipment scale. Following these corrections focal plane spectra can be fitted. In order to identify excited states and to extract cross sections the peaks must be fitted with an appropriate fit function. Many states are seen across the focal plane which overlap with each other and contaminant states. Procedures must therefore be developed when fitting spectra to ensure consistency at each angle. The choice of fit function will be discussed in section 4.2.1, with the procedure described in section 4.2.2 and the individual fits detailed in section 4.2.3.

4.2.1 Peak Functions

It is clear from Figure 4.2 that the observed peaks are asymmetric. This is because the energy resolution of the Q3D is sufficiently high that effects such as energy loss through target and the MWPCs are visible as low energy tails on peaks. In order to fit these peaks an asymmetric peak function must be used. Several peak functions were trialled and compared in order to select a single function which will be used to fit the full focal plane spectrum. The first function trialled was a Landau function which has the form:

$$y = Ae^{\frac{-\lambda + e^{-\lambda}}{2}} \quad (4.3)$$

$$\lambda = \frac{x - \mu}{S},$$

where the parameter μ is the peak centroid and S is a parameter which controls both the width and length of the low energy tail. This function was first described by Landau to describe energy loss of a charged particle through a thin layer of matter [80], which should make it a suitable fit function. A second function which

was tested was the Radware Peak [81]. The Radware peak consists of a sum of a regular Gaussian peak and an exponential convolved with a Gaussian broadening and is defined as:

$$y = A \left(e^{-\frac{(x-\mu)^2}{2\sigma^2}} \cdot \eta + e^{\frac{x-\mu}{\beta}} \cdot \operatorname{erfc} \left[\frac{x-\mu}{\sigma\sqrt{2}} + \frac{\sigma}{\beta\sqrt{2}} \right] \cdot (1-\eta) \right). \quad (4.4)$$

Where the parameters μ and sigma are the standard Gaussian parameters and erfc is the complimentary error function which is related to the error function erf by, $\operatorname{erfc} = 1 - \operatorname{erf}$. The length of the low energy tail is controlled by the parameter β and η is a mixing ratio. This function was designed to fit the small tails caused by charge trapping in germanium detectors, but it should be able to be used for this work. The third fit function tested was the Crystal Ball function, which is commonly used in high energy physics. The function consists of two parts, a Gaussian peak above an energy threshold and a power-law low-end tail below the threshold. The function is given by:

$$y = A \cdot \begin{cases} e^{-\frac{(x-\mu)^2}{2\sigma^2}} & \text{for } \frac{x-\mu}{\sigma} > -a \\ \left(\frac{n}{|\alpha|}\right)^n \cdot e^{-\frac{|\alpha|^2}{2}} \cdot \left(\left[\frac{n}{|\alpha|} - |\alpha|\right] - \frac{x-\mu}{\sigma}\right)^{-n} & \text{for } \frac{x-\mu}{\sigma} \leq -a, \end{cases} \quad (4.5)$$

where α marks the transition to the power-law tail and n is the order of the tail [82]. The final function which was trialled was the Skew Gaussian:

$$y = Ae^{-\frac{(x-\mu)^2}{2\sigma^2}} \cdot \left(1 + \operatorname{erf} \left[\alpha \cdot \frac{x-\mu}{\sigma\sqrt{2}} \right] \right). \quad (4.6)$$

The parameters defined in the function are the standard Gaussian parameters with the extra parameter α controlling the skewness of the function. The functions are trialled by fitting an isolated ^{35}Cl peak on a constant background, the result of this can be seen Figure 4.7. It can be seen that the fit functions all produce good fits with reduced χ^2 values of ~ 1 obtained for all the fits. The centroids extracted from the fits are found to vary with the Landau function, eq. (4.3), having the largest centroid value. Despite this the centroids are found to be consistent within error as are the extracted peak areas. This would suggest that all peaks would be suitable for the full focal plane fits. As multiple peaks will need to be fitted simultaneously it was decided that the number of fit parameters should be minimised. The Crystal Ball, eq. (4.5), and Radware Peak, eq. (4.4), have the largest number of fit parameters so were not chosen. While the Skew Gaussian, eq. (4.6) produces a good fit, the Landau

function, eq. (4.3), has the smallest number of parameters and was formulated to describe the type of energy loss seen in the Q3D. For these reasons the Landau function was chosen as the fit function.

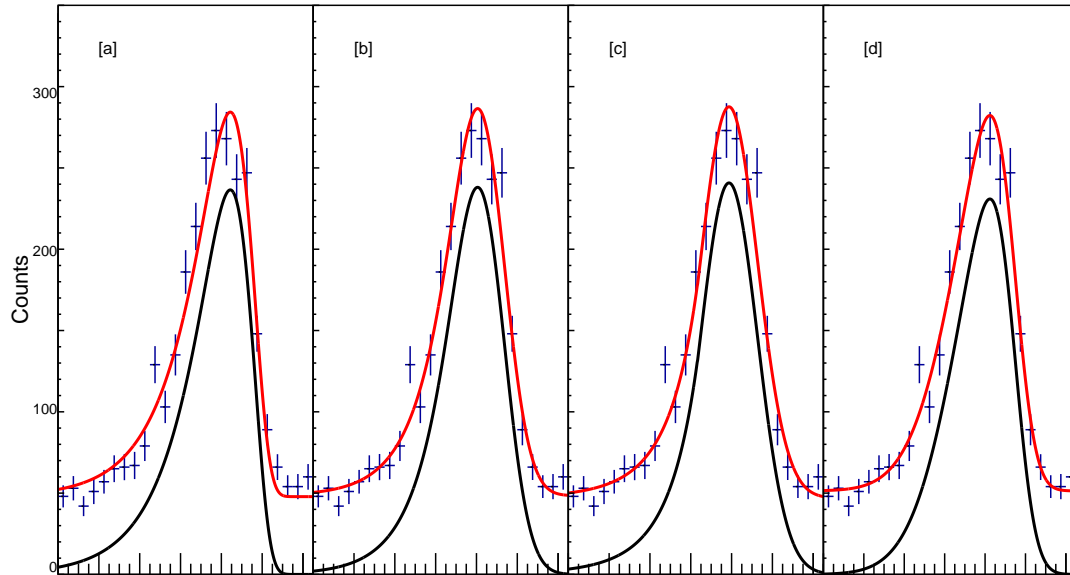


Figure 4.7: Comparison of multiple asymmetric peak function fits on an isolated ^{35}Cl state. Shown are a fit of a peak on a constant background with the extracted peak seen in black. The functions used are detailed in the text and are; a- Landau Function eq. (4.3), b - Radware Peak eq. (4.4), c - Crystal Ball Function eq. (4.5), d - Skew Gaussian eq. (4.6).

4.2.2 Fitting Procedure

The focal plane spectra are fitted with a total spectrum fit consisting of multiple peaks on a linear background. Due to the large number of peaks seen across the focal plane several assumptions are made in order to reduce the number of fit parameters. Minimising the number of fit parameters should reduce the computational time and should prevent erroneous results, e.g reducing the χ^2 value, but using peaks which are non-physical.

With the exception of peaks due to broad resonances, the resolution is expected to be dominated by the detector resolution rather than the intrinsic widths of the populated states. A single parameter, S in eq. (4.3), will be used to control the width of all the peaks which reduces the total amount of fit parameters by a third. The peak position is constrained in a narrow window based on a visible inspection of the spectrum leaving the peak height as the only unconstrained parameter.

The Q3D is set to focus products from a specific reaction while defocussing other reactions. States in ^{35}Cl observed at the focal plane will appear more narrow compared to contaminant states which will be broader and may have an ill-defined peak shape. Those contaminant states which cannot be modelled with a simple peak function are excluded from the total focal plane fit. States in ^{35}Cl which overlap with the contaminants will also be excluded from the fit as it is not possible to extract an accurate peak area without knowing the absolute magnitude of the contaminant state. Specific descriptions of the fitting procedure used at each measurement angle will be discussed below.

4.2.3 Focal Plane Fits

4.2.3.1 Focal Plane fit 5°

The broad 2.365 MeV state in ^{13}N seen at channel ~ 550 in Figure 4.1 cannot be fitted with a simple peak function, therefore the focal plane fit will be performed in two parts.

Region 1 - The first fit region covers channels 680–2450 of the focal plane. Peaks are fitted on a linear background with an exponential contribution from the broad ^{13}N state. Peaks due to reactions on ^{32}S and ^{16}O can be modelled with a Landau peak function and are also included in the fit. Due to the kinematic mismatch it was expected that peaks from reactions on ^{16}O would be broadened and the fact that this state can be fit with a simple peak function is surprising. The width of this peak, however is found to be broader than peaks in ^{35}Cl so there does appear to be an effect from kinematic mismatch. The peak seen at channel ~ 1550 , from reactions on ^{14}N , overlaps with states believed to be from ^{35}Cl . The ^{14}N target content cannot be calculated so the exact magnitude of the peak cannot be determined. Extracted peak areas for the ^{35}Cl states will be incorrect so the region covering channels 1550–1620 are excluded from the fit.

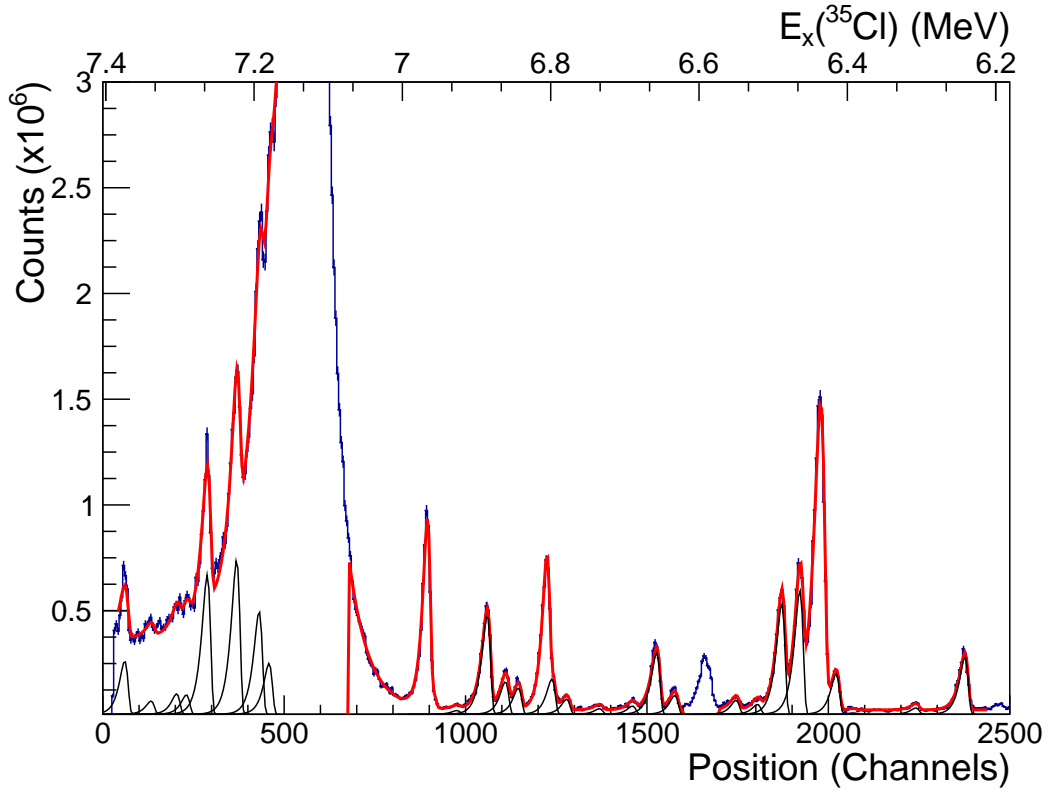


Figure 4.8: Fitted Focal plane spectra at 5° for the Ag_2^{34}S Target. The total fit is seen in red with the individual peaks shown in black. The top axis shows the energy of the excited states in ^{35}Cl from a linear calibration fit and should be taken as approximations only. A detailed description of the fit can be seen in the text.

Region 2 - The second fit region covering channels 30–480 is then fit as peaks on a constant background with an exponential due to the low energy tail of the ^{13}N state. The width parameter, S in eq. (4.3), is not allowed to vary and is fixed from the value obtained in the first fit.

The final result of the fit, showing the individual peak contribution can be seen in Figure 4.8. Once a calibration has been performed, section 4.3, the extracted peak positions will be converted into an excitation energy which is noted in Table 4.1.

4.2.3.2 Focal Plane fit 10°

Figure 4.3 shows the overlay of the experimental targets at 10° to identify the ^{35}Cl states to be fitted. As with the 5° focal plane fit the 10° spectra is fitted in two parts, before and after the broad ^{13}N state.

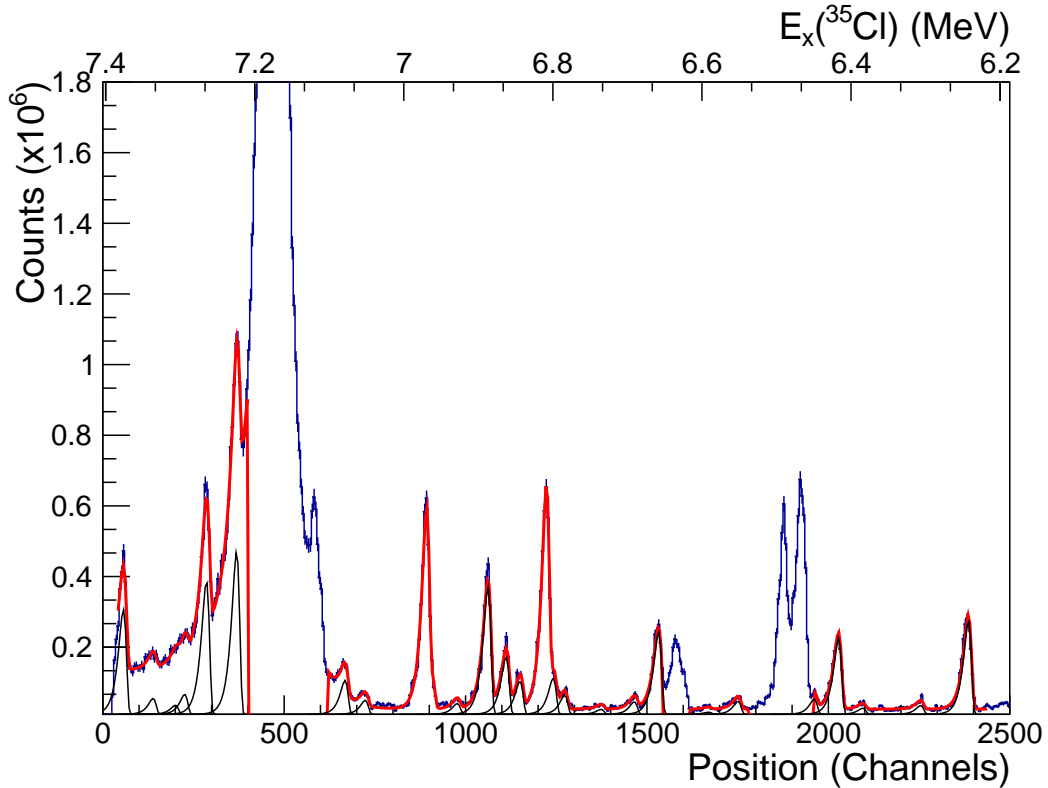


Figure 4.9: Fitted Focal plane spectra at 10° for the Ag_2^{34}S Target. The total fit is seen in red with the individual peaks shown in black. The top axis shows the energy of the excited states in ^{35}Cl from a linear calibration fit and should be taken as approximations only. A detailed description of the fit can be seen in the text.

Region 1 - The region spanning channels 580–2450 are again fit with peaks on a linear background with an exponential contribution from the broad ^{13}N state. The peaks seen at channels 900 and 1200 from states in ^{33}Cl are again included in the fit. Excluded from the fit are the regions spanning channels 1540–1620 and 1780–1960 due to reactions on ^{14}N and ^{16}O which cannot be fitted with a simple peak function.

Region 2 - The second region spans channels 30–480 and is fitted as multiple Landau functions on an exponential background to model low energy tail of the ^{13}N state.

The focal plane fit can be seen in Figure 4.9 with the extracted peak positions converted into an excitation energy and shown in Table 4.1.

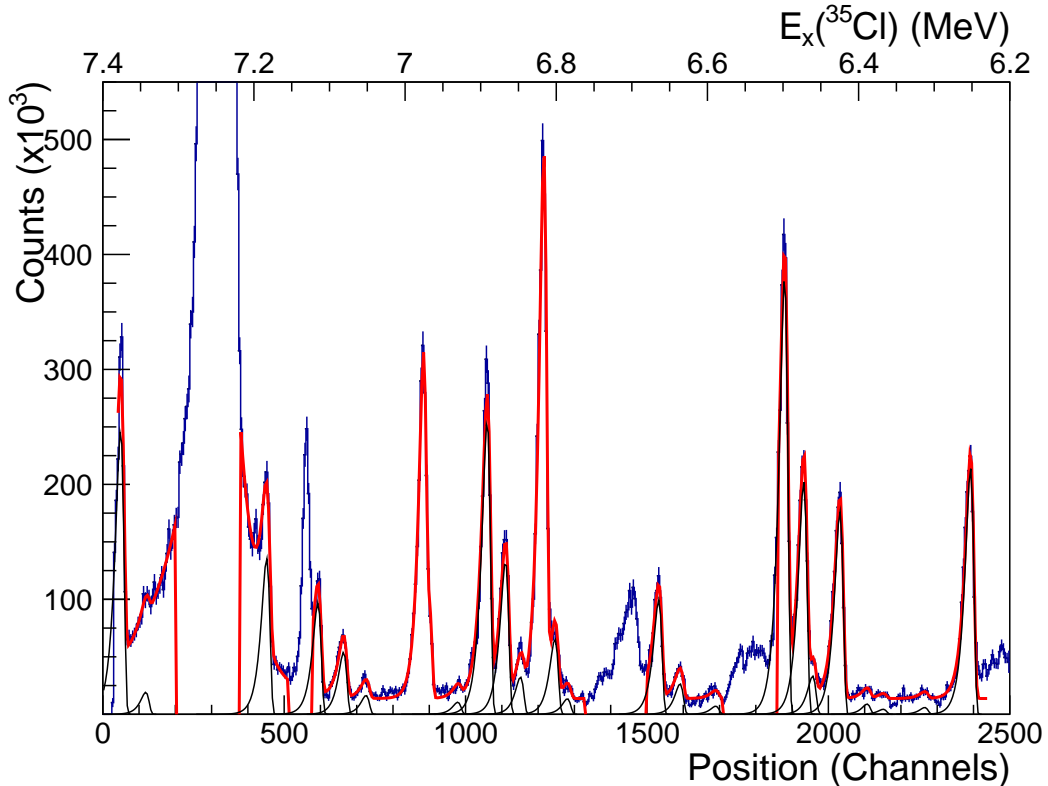


Figure 4.10: Fitted Focal plane spectra at 15° for the Ag_2^{34}S Target. The total fit is seen in red with the individual peaks shown in black. The top axis shows the energy of the excited states in ^{35}Cl from a linear calibration fit and should be taken as approximations only. A detailed description of the fit can be seen in the text.

4.2.3.3 Focal Plane fit 15°

Due to the continued presence of the broad 2.365 MeV ^{13}N state, seen at channel 300 in Figure 4.4 the focal plane fit is again performed in two parts as with the 5° and 10° focal fits. The regions which are fitted are:

Region 1 - Between channels 380 and 2400 excluding the regions 1330–1500 and 1710–1860 which overlap peaks from reactions on ^{14}N and ^{16}O . Additionally a state in ^{14}N can be seen at channel 560 from reactions on ^{13}C present within the carbon backing of the target. While the state appears to be able to be fit with a simple function, its magnitude cannot be determined so the region 510–580 is excluded.

Region 2 - The second fit region is between channels 35–200 and again fit as two Landau peak functions on an exponential background.

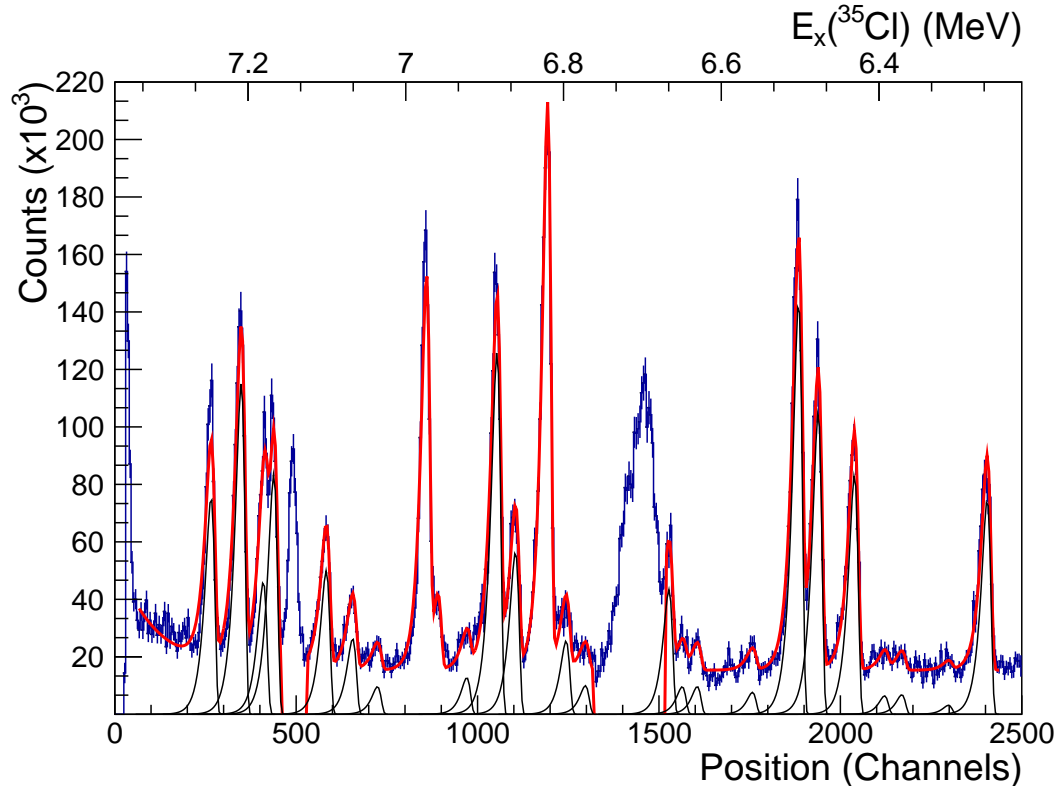


Figure 4.11: Fitted Focal plane spectra at 25° for the Ag_2^{34}S Target. The total fit is seen in red with the individual peaks shown in black. The top axis shows the energy of the excited states in ^{35}Cl from a linear calibration fit and should be taken as approximations only. A detailed description of the fit can be seen in the text.

Figure 4.10 shows the full focal plane fit with the extracted peak positions detailed in Table 4.1.

4.2.3.4 Focal Plane fit 25°

As the broad ^{13}N state has drifted off the focal plane, Figure 4.5, it is no longer necessary to perform the focal plane fit in two parts. A full focal plane fit is performed between channels 65–2450 which can be seen in Figure 4.11. A small exponential background is included due to the high-energy tail of the ^{13}N state still seen at the edge of the focal plane. There is sufficient contribution from reactions on ^{14}N so it is no longer required to exclude regions which overlap with this peak. There are still strong contributions from reaction on ^{13}C and ^{16}O , therefore the regions 460–530 and 1320–1520 are excluded from the fit. Extracted excitation energies for this fit are seen in Table 4.1.

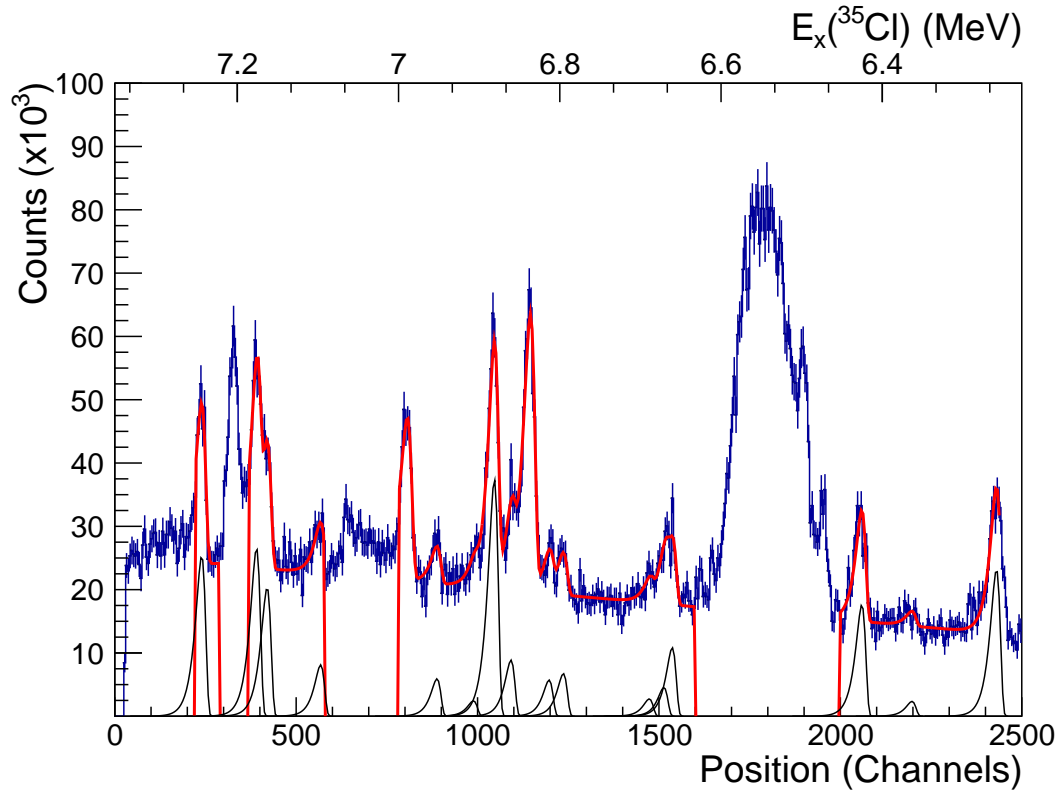


Figure 4.12: Fitted Focal plane spectra at 40° for the Ag_2^{34}S Target. The total fit is seen in red with the individual peaks shown in black. The top axis shows the energy of the excited states in ^{35}Cl from a linear calibration fit and should be taken as approximations only. A detailed description of the fit can be seen in the text.

4.2.3.5 Focal Plane fit 40°

At 40° a large part of the focal plane spectrum begins to overlap with the ^{17}F ground state. Due to the peak shape, seen in Figure 4.6 at channel 1800, which cannot be modelled with a simple function the region spanning channels 1600–2500 of the focal plane are excluded from the focal plane fit. The 0.495 MeV state in ^{17}F is also still present across the focal plane which requires channels 580–780 to be excluded from the fit. Finally, the 7.029 MeV state in ^{14}N , from reactions on ^{13}C , can be seen at channel 350 so the region covering channels 290–370 is excluded from the fit. The ^{33}Cl states are still present at channels 800 and 1100 and are included in the fit as normal. The full fit with the individual state contribution is shown in Figure 4.12, with the extracted excitation energies given in Table 4.1.

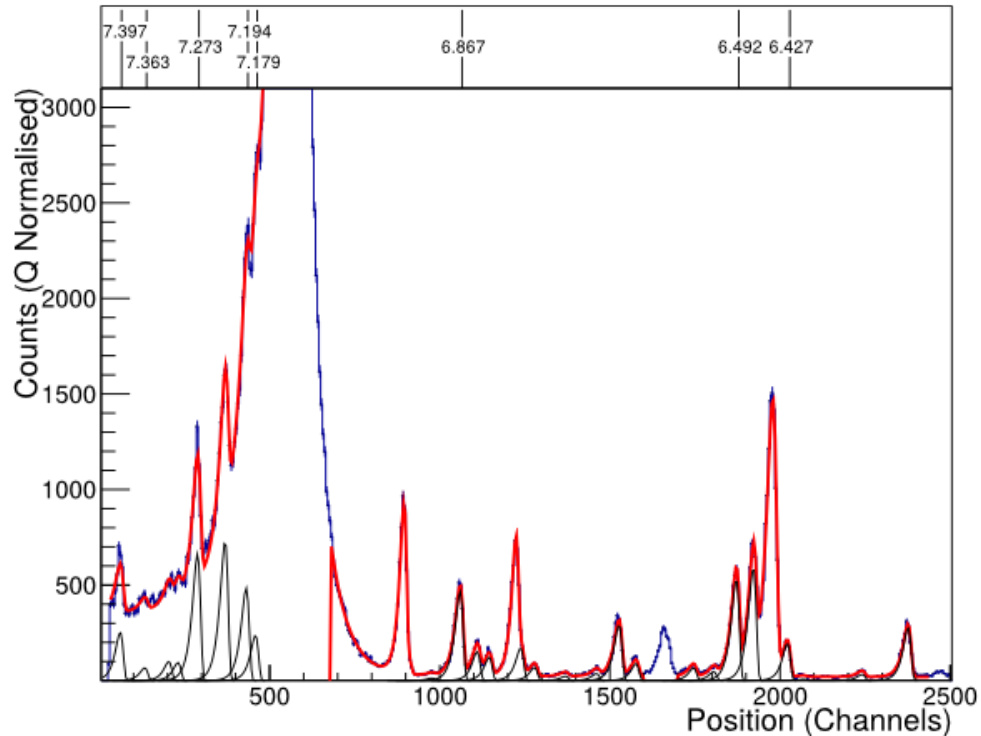


Figure 4.13: States used in the calibration of the focal plane for the $^{34}\text{S}(^3\text{He},\text{d})^{35}\text{Cl}$ reaction. Bottom - 5° fitted focal plane spectra at for the Ag_2^{34}S target showing the individual peak contributions. Top - Previously observed states used in the focal plane calibration. Excitation energies are given in MeV.

4.3 Focal Plane Calibration

An internal calibration of the Ag_2^{34}S target was performed using known states in ^{35}Cl . The advantage of this method is that energy losses through the target can be neglected. Initially the 2.685 and 2.846 MeV states in ^{33}Cl [75, 76] are used to perform a simple two-point calibration as described in section 3.2.4. Using the reaction kinematics it is possible to calculate the energy of the scattered deuteron for specific target excitation energies. The magnetic rigidity $B\rho$ of these deuterons are then calculated from the Q3D magnetic field settings and used to perform a focal plane position to $B\rho$ calibration. From this calibration the peak positions extracted from the focal plane fits, Figures 4.8 to 4.12, are converted into an excitation energy. Due to momentum matching, section 2.1.3.3, the $(^3\text{He},\text{d})$ reaction should populate the same states as in the (p,γ) reaction [29,30]. Using the two-point energy calibration it is possible to identify these states and then use them to perform a second calibration using the states shown in Figure 4.13. This is fitted with a 2^{nd}

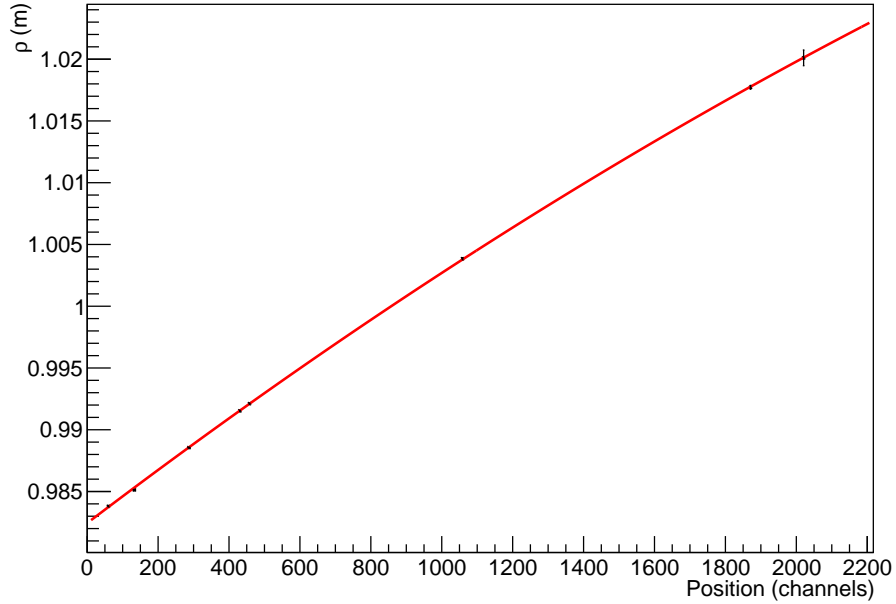


Figure 4.14: 5° $^{34}\text{S}(^3\text{He},d)^{35}\text{Cl}$ Focal Plane Calibration Curve. States known from previous (p,γ) experiments are identified along the focal plane and used to perform a calibration of focal plane position vs deuteron energy which can be related to excitation energy.

order polynomial, the result of this is at 5° is seen in Figure 4.14. The vertical errors are due to the uncertainties in the known excitation energies. These energies are known from (p,γ) reactions and are known to less than 1 keV, with the exception of the 6.427 MeV state which was observed in an (α,p) reaction and has an uncertainty of 4 keV. Separate calibrations are performed at each angle. Table 4.1 shows the energy of the states seen across the focal plane at more than 3 or more angles.

4.4 Angular Distributions

In order to produce angular distributions the extracted peak areas of the fitted states must be converted into a differential cross section. As seen in eq. (2.1) the cross section is the number of reactions per beam current and target atoms. The differential cross section for a peak at specific angle is therefore defined as:

$$\frac{d\sigma}{d\Omega} = \frac{N_{peak}}{N_T I_B d\Omega}, \quad (4.7)$$

Table 4.1: States observed in the $^{34}\text{S}(^3\text{He},\text{d})^{35}\text{Cl}$ reaction. Shown are the excitation energy of the states at each measurement angle in MeV with the average excitation energy given in the first column. A dash indicated that the state was not observed at a particular angle.

E_x (MeV)	5°	10°	15°	25°	40°
7.400(2)	7.400(2)	7.402(2)	7.399(2)	-	-
7.359(2)	7.359(2)	7.356(2)	7.361(2)	-	-
7.273(2)	7.273(2)	7.273(2)	-	7.272(2)	7.274(2)
7.227(2)	7.228(2)	7.227(2)	-	7.227(2)	-
7.194(2)	7.194(2)	-	-	7.194(2)	7.194(2)
7.178(2)	7.179(2)	-	7.178(2)	7.179(2)	7.178(2)
7.103(2)	-	-	7.103(2)	7.102(2)	7.102(2)
7.066(2)	-	7.067(2)	7.066(2)	7.065(2)	-
7.030(2)	-	7.038(2)	7.034(2)	7.030(2)	-
6.907(2)	6.908(2)	6.908(2)	6.906(2)	6.906(2)	-
6.866(2)	6.867(2)	6.866(2)	6.866(2)	6.866(2)	6.867(2)
6.842(2)	6.842(2)	6.841(2)	6.842(2)	6.841(2)	6.845(2)
6.823(2)	6.824(2)	6.822(2)	6.822(2)	-	-
6.778(2)	6.780(2)	6.778(2)	6.776(2)	6.775(2)	6.779(2)
6.761(2)	6.760(2)	6.763(2)	6.760(2)	-	-
6.674(2)	6.674(2)	6.673(2)	-	-	6.672(2)
6.643(2)	6.643(2)	6.642(2)	6.643(2)	6.645(2)	6.645(2)
6.545(2)	6.545(2)	6.545(2)	-	6.545(2)	-
6.491(2)	6.490(2)	-	6.491(2)	6.492(2)	-
6.468(2)	6.468(2)	-	6.468(2)	6.469(2)	-
6.427(2)	6.426(2)	6.427(2)	6.427(2)	6.428(2)	6.429(2)
6.402(2)	6.406(2)	6.399(2)	6.396(2)	6.395(2)	-
6.377(2)	-	-	6.378(2)	6.377(2)	6.377(2)
6.329(4)	6.336(4)	6.335(4)	6.333(4)	6.327(4)	-
6.284(4)	6.283(4)	6.284(4)	6.284(4)	6.287(4)	6.289(4)

where N_{peak} is the area under a peak, N_T is the number of target atoms per unit area and I_B is the beam current. The parameter $d\Omega$ is the solid angle of the Q3D acceptance window and has a value of $5.33 \mu\text{sr}$ at all angles. The differential cross section at each angle are then plotted as angular distributions which will be used to extract angular momentum values and spectroscopic factors when compared to DWBA calculations.

4.4.1 DWBA Calculations

Finite range DWBA calculations were performed using the coupled channel reaction code FRESKO [58]. As an optical potential was not measured in this work, global potentials were used in the calculations. Two global potentials have been previously calculated for an incoming ^3He channel, by Liang *et al.* [83] and Pang *et al.* [84]. The potential of Pang *et al.*, however was calculated with experimental data for targets with $A > 40$ so was not chosen. For the deuteron exit channel an optical potential by Daehnick *et al.* [85] was chosen, which has been used extensively in transfer reaction studies. As only low spin states are expected to be populated in ($^3\text{He},d$) transfer reactions, calculations were performed only for angular momentum values of $\ell=0-3$. Due to the intrinsic spin of the transferred proton, $s=1/2$, DWBA calculations were performed for both $J=\ell+s$ and $J=\ell-s$ angular momentum coupling. It is unlikely, however that definite spin assignments of states in ^{35}Cl can be made. The DWBA calculations were tested by replicating angular distributions and spectroscopic factors of a previous ($^3\text{He},d$) study [86]. Full details of this are given in Appendix A.

4.4.2 $^{32}\text{S}(^3\text{He},d)^{33}\text{Cl}$ Angular Distributions

While no previous studies of the $^{34}\text{S}(^3\text{He},d)^{35}\text{Cl}$ reaction are available for comparison, the $^{32}\text{S}(^3\text{He},d)^{33}\text{Cl}$ reaction has been extensively studied, [75, 76, 87], using DWBA calculations to make spin assignments and extract proton transfer spectroscopic factors for the 2.685 and 2.846 MeV states. The experimental angular distributions and calculations of this work can be compared with the previous studies as a further test of the optical potentials and DWBA calculations used in this work. In addition to the two states populated in previous $^{32}\text{S}(^3\text{He},d)^{33}\text{Cl}$ studies a third state seen at 2.839 MeV has been observed in direct proton capture studies [77–79]. The energy

resolution of the previous $^{32}\text{S}(^3\text{He,d})^{33}\text{Cl}$ studies, $\sim 60\text{keV}$ [75,76,87], is not sufficient to resolve this state so the extracted spectroscopic factors could be overestimated for the 2.846 MeV state.

Differential cross sections are extracted by fitting the spectra obtained using the $\text{Zn}_2^{\text{nat}}\text{S}$ target. Given the superior energy resolution of the Q3D spectrometer there is evidence at all angles of a doublet which is believed to be the 2.846 and 2.839 MeV states in ^{33}Cl . As with the $^{34}\text{S}(^3\text{He,d})^{35}\text{Cl}$ spectra the peaks are fitted simultaneously as three Landau functions on a linear background. The result of the fits at all angles, including the extracted peaks areas can be seen in Figure 4.15.

After extracting the peak areas the differential cross sections at each measurement angle are calculated using Equation (4.7) and used to extract angular distributions. DWBA calculations are performed using FRESKO with the global potentials of Liang *et al.* [85] and Daehnick *et al.* [83]. The calculations are fitted to the experimental data in order to determine the angular momentum transferred. From the fits a scalar parameter is obtained which is the proton transfer spectroscopic factor S . The results of these fits can be seen in Figure 4.16 which show the angular distributions overlaid with the theoretical calculations for $\ell=0-3$ angular momentum transfer. As it is difficult to fully resolve the 2.839 and 2.846 MeV states at 5° the theoretical distributions are not fit at this point. The calculations are performed for both $J=\ell+s$ and $J=\ell-s$ coupling, however only the results from the $J=\ell+s$ are presented here. While the extracted spectroscopic factors, S , differ depending upon the coupling, previous studies present results only for $J=\ell+s$ coupling. For all cases the isospin Clebsch-Gordon coefficient, C^2 has a value of 1.

As can be seen in Table 4.2 the agreement between the present work and the previous results is not good. While the ℓ transfer for the 2.846 MeV state is in agreement with the previous results the extracted C^2S is found to be 2-3 times smaller than previously observed. For the 2.685 MeV state an $\ell=3$ transfer was previously assigned, however χ^2 analysis favours an $\ell=2$ transfer in the present work. For the $\ell = 2$ transfer a χ^2 value of 6 is found from the fit compared to $\chi^2 = 18$ for an $\ell = 3$ transfer. From this it is possible to conclude that an $\ell = 2$ transfer is favoured by over 3σ compared to the $\ell = 3$ assignment. The 2.839 MeV state has not been previously observed in $(^3\text{He,d})$ studies, however proton capture studies have assigned this state as a $5/2^+$ state. [77–79], which is in agreement with this work.

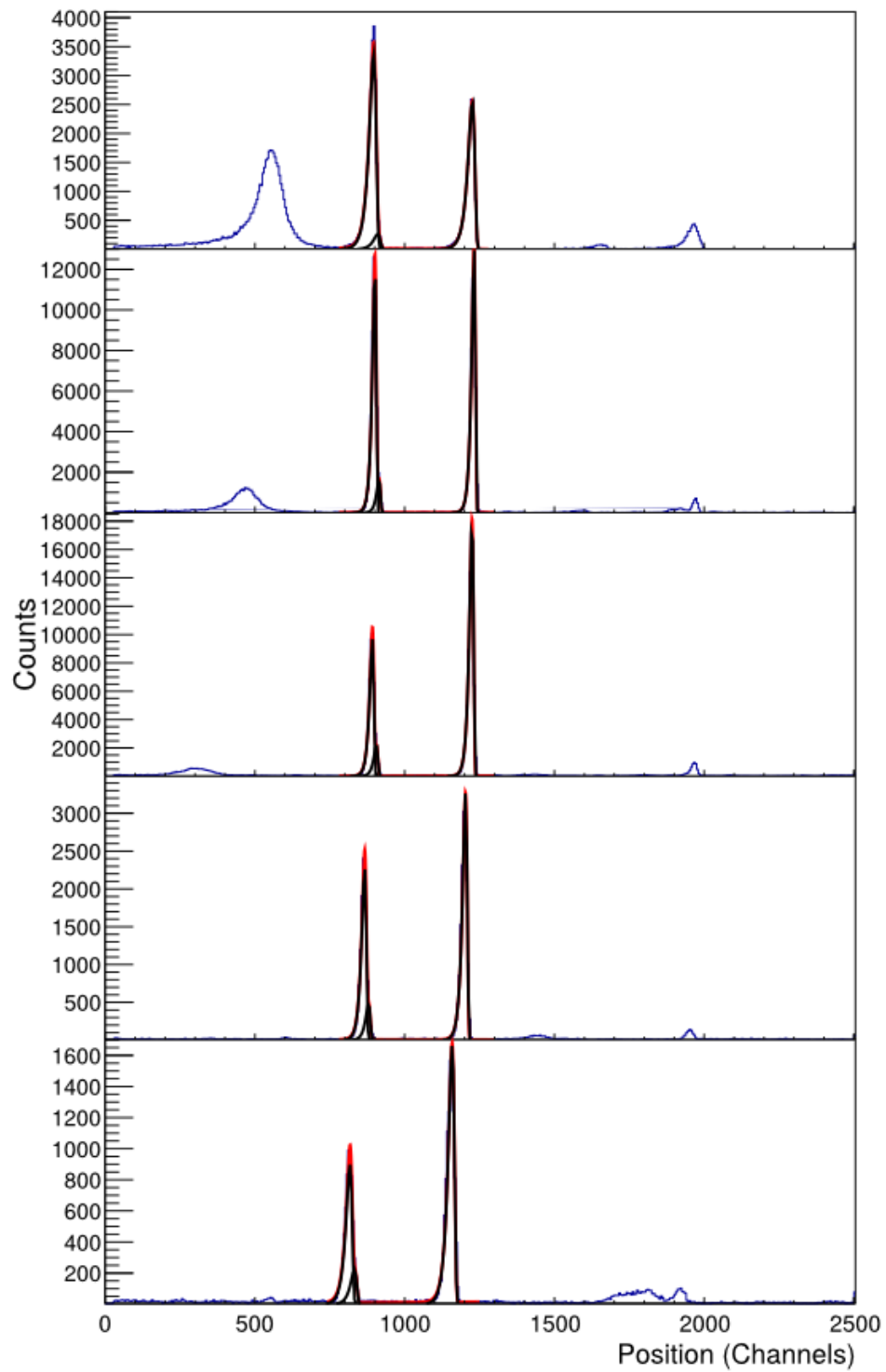


Figure 4.15: Fitted Focal plane spectra for the $\text{Zn}_2^{\text{nat}}\text{S}$ target. In red is the total spectrum fit with the individual peak contribution seen in black. The measurement angle of the spectra from top to bottom are 5, 10, 15, 25 and 40°

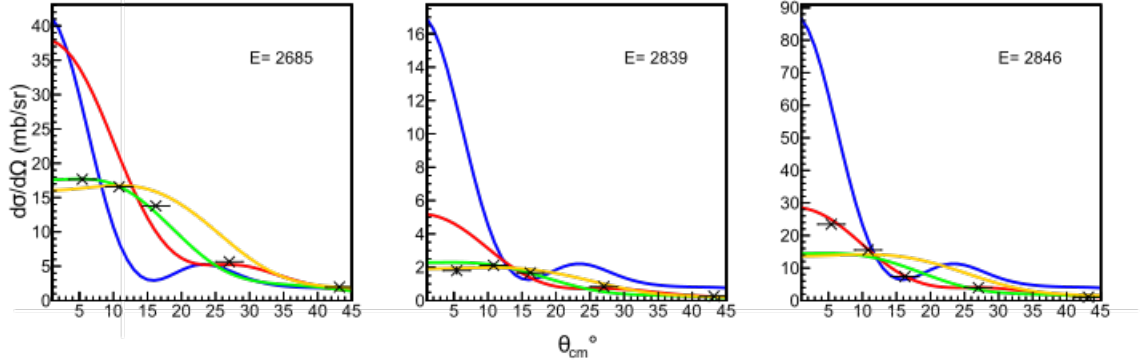


Figure 4.16: Deuteron angular distributions measured with the $^{32}\text{S}(^3\text{He},\text{d})^{33}\text{Cl}$ reaction at 20 MeV for $J=\ell+s$ coupling. Graphs are fitted with calculated DWBA angular distributions for angular momentum transfer $\ell=0$ (Blue), $\ell=1$ (Red), $\ell=2$ (Green), $\ell=3$ (Yellow). Extracted angular momentum transfer and spectroscopic factors from the fits are summarised in Table 4.2

Table 4.2: Summary of ^{33}Cl angular distributions fits. The errors in C^2S are from the fits only. In addition a systematic uncertainty of 20% is expected due to the quoted precision of the experimental target thickness, however this is not shown. Also shown are the results of previous studies [75, 76, 87]. The results of [76] are for two sets of optical potentials.

Ex (MeV)	Previous Studies				Present Work	
	ℓ Transferred	C^2S			ℓ Transferred	C^2S
2.685	3	0.73 [75]	0.50/0.41 [76]	0.52 [87]	2	0.284(8)
2.839	-	-	-	-	2/3	0.038(2)/0.044(2)
2.846	1	0.55 [75]	0.50/0.58 [76]	0.72 [87]	1	0.250(5)

While the present results are not in good agreement with the previous transfer experiments, it is not believed they are incorrect. The energy resolution of the Q3D is far superior than that used in the previous work, which is apparent from the observation of the 2.839 keV state. Given the cleanliness of the spectra; the quality of the fits seen in Figure 4.15; and the understanding of the contaminant states and the χ^2 values it is unlikely that there has been a misidentification of the states. With regards to the DWBA calculations, it has been shown in Appendix A that previous results can be replicated. When fitting the DWBA calculation to the experimental angular distributions the fit results clearly show the assignments shown in Table 4.2. While it is not possible to speculate on the differences between the present and the previous work it is clear that our data favours the present results.

4.4.3 $^{34}\text{S}(^3\text{He},\text{d})^{35}\text{Cl}$ Angular Distributions

Experimental angular distributions for the states seen in Table 4.1 are all drawn and fitted with DWBA calculations. An example of the calculations used to calculate the differential cross sections needed to draw the angular distributions are shown in section B.1. The result of these fits for $J=\ell+s$ coupling are seen in Figure 4.17 with the $J=\ell-s$ coupling shown in Figure 4.18. The best fits for each state, showing angular momentum transfer, ℓ , and spectroscopic factors, C^2S , are summarised in Table 4.3 along with previous assignments where available. Due to the quoted precision of the experimental targets an additional 20% uncertainty, not shown in Table 4.3, should be included. It should be noted that for some states it is not possible to make definite spin assignments and multiple angular momentum transfer values are allowed. It is clear from Figures 4.17 and 4.18 that there is no difference in angular momentum transfer when comparing calculations for $J=\ell+s$ or $J=\ell-s$ coupling. Different spectroscopic factors C^2S are extracted depending upon the type of coupling.

For some states it was not possible to find a satisfactory fit. Notable is the 7.178 and 7.194 MeV states for which no good fit can be found for the later and the former is in disagreement with the previous studies [29, 30] which report the state as a $1/2^+$, $\ell=0$ transfer, opposed to this work where an $\ell=2$ or 3 transfer is needed. A possible explanation for this discrepancy is the existence of a state at 7.185 MeV which has been observed in a $^{36}\text{Ar}(\text{d},^3\text{He})$ study and has a $5/2^+$ spin parity assignment. The existence of this state could account for poor and incorrect spin assignments as it would not be possible to fully resolve the 7.179, 7.185 and 7.194 triplet given the resolution of the Q3D. For this reason our result for the 7.179 MeV and 7.194 MeV state will be disregarded when calculating the reaction rate and the previous results will be used instead.

For other cases where no spin assignments can be made, fits are performed using mixed transitions. For this case the distributions are fitted with a sum of two different ℓ transitions, $\ell=0+2$ and $\ell=1+3$, for which separate C^2S values are extracted. Mixed transitions are only investigated where a state has been observed at 4 or 5 angles, but does not have a good fit. An example is the 6.867 MeV state, which is known from previous studies [88] and observed at all measurement angles. The angular distribution for this state is fitted with an $\ell=0+2$ theoretical distribution with the result seen in Figure 4.19. A comparison of the χ^2 values show

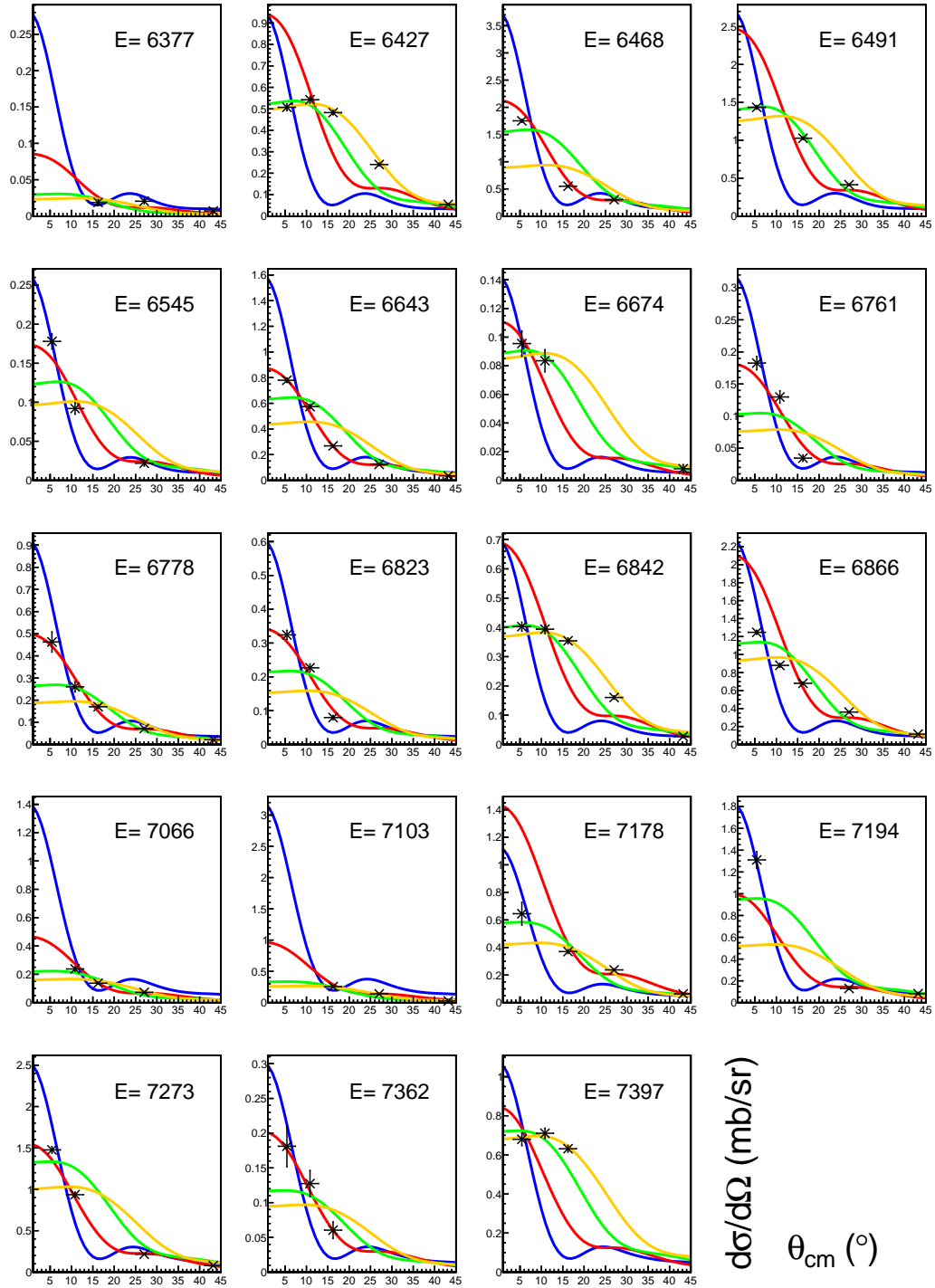


Figure 4.17: Deuteron angular distributions measured with the $^{34}\text{S}(^3\text{He},d)^{35}\text{Cl}$ reaction at 20 MeV for $J=\ell+s$ coupling. Graphs are fitted with calculated DWBA angular distributions for angular momentum transfer $\ell=0$ (Blue), $\ell=1$ (Red), $\ell=2$ (Green), $\ell=3$ (Yellow). Extracted angular momentum transfer and spectroscopic factors from the fits are summarised in Table 4.3.

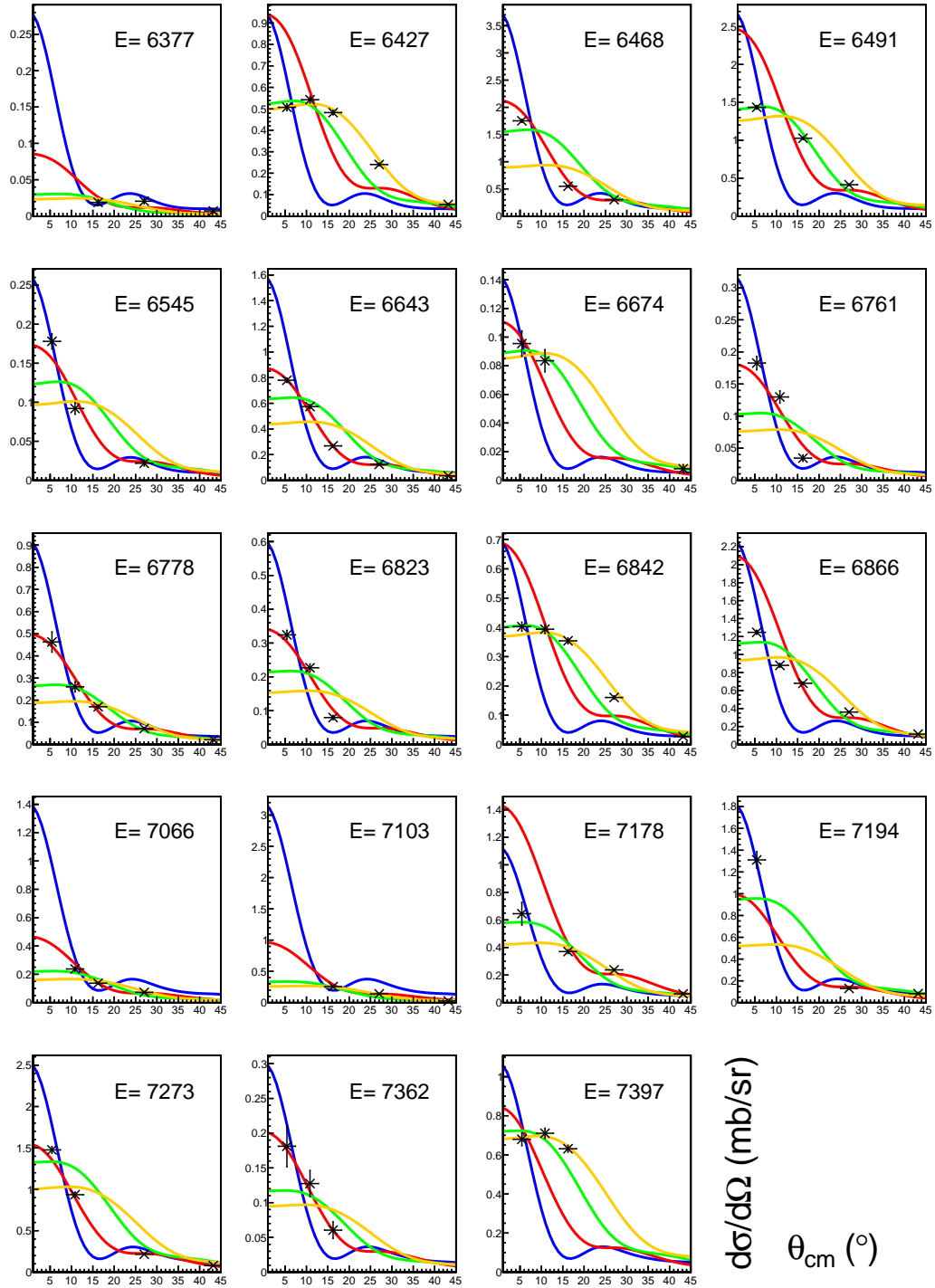


Figure 4.18: Deuteron angular distributions measured with the $^{34}\text{S}(^3\text{He},d)^{35}\text{Cl}$ reaction at 20 MeV for $J=\ell-s$ coupling. Graphs are fitted with calculated DWBA angular distributions for angular momentum transfer $\ell=0$ (Blue), $\ell=1$ (Red), $\ell=2$ (Green), $\ell=3$ (Yellow). Extracted angular momentum transfer and spectroscopic factors from the fits are summarised in Table 4.3.

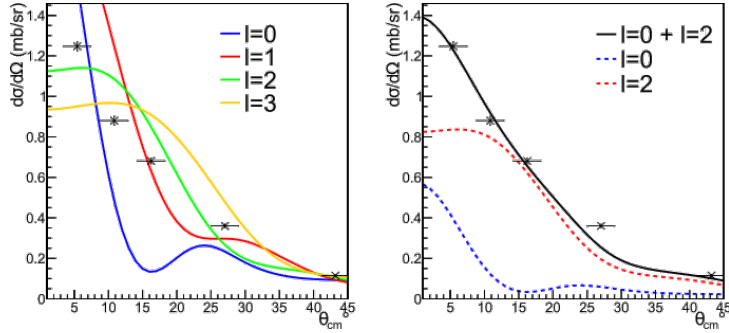


Figure 4.19: Angular distribution for the $E = 6.867$ MeV state in ^{35}Cl fit. Left - The angular distribution has been fitted with calculated DWBA angular distributions for angular momentum transfer $\ell=0$ (Blue), $\ell=1$ (Red), $\ell=2$ (Green), $\ell=3$ (Yellow). Right - The distribution has been fit with a mixed $\ell=0 + \ell=2$ transition. Shown in black is the total fit with the individual $\ell=0$ and $\ell=2$ components seen in blue and red respectively.

a mixed transition is favoured over a pure ℓ transfer. For the case of a pure transition an $\ell = 2$ transfer produces the best fit with a $\chi^2 = 16$, however for a mixed $\ell = 0 + 2$ transition a χ^2 value of 6 is found. From this it is possible to reject the pure $\ell = 2$ transition at the 3σ level in comparison to a mixed $\ell = 0 + 2$ transition.

4.5 Thermonuclear Reaction Rate

After extracting the spectroscopic factors C^2S for the observed states it becomes possible to convert them into resonance strength $\omega\gamma$. The method for this is detailed in section 2.4. As there is no evidence of broad states being seen across the focal plane spectra Figures 4.8 to 4.12, the resonant reaction rate is calculated using the narrow resonances approximation described in section 2.4.2. As the DWBA fits allow for multiple spin assignments a minimum and maximum $\omega\gamma$ is calculated for all observed states. An example of the calculation is given in section B.2. Using these values a minimum and maximum reaction rate will be determined which will provide the uncertainties when calculating the final $^{32}\text{S}/^{34}\text{S}$ ratio in ONe white dwarf novae. The minimum and maximum values of $\omega\gamma$ used in this work are shown in Table 4.4 and compared with previous results where available. In addition to the values used in this work the reaction rate will be calculated with all previously known $\omega\gamma$ values [89].

Reaction rates are calculated using Monte Carlo methods implemented through

Table 4.3: Nuclear structure of ^{35}Cl for states within $6.2 < E_x < 7.4$ MeV. The first two columns give weighted averages of E_x and J^π assignments from previous (p,γ) studies [29, 30]. The final three columns give E_x , ℓ and extracted proton spectroscopic factors C^2S for the adopted orbital angular momentum transfer values ℓ with $J=\ell+s$ coupling, as determined in the present work.

Previous Work [29, 30]		Present Work		
E_x (keV)	J^π	E_x (keV)	ℓ	C^2S
-	-	6284(2)	2	0.0143(3)
-	-	6329(2)	0,1	0.0015(3)/0.0011(1)
6379(3)	-	6377(2)	2,3	0.0002(1)/0.0003(1)
6427(5)	-	6427(2)	3	0.0061(2)
-	-	6468(2)	1	0.0084(3)
6492(2)	-	6491(2)	2	0.0120(3)
-	-	6545(2)	0,1	0.0020(5)/0.0007(1)
-	-	6643(2)	1	0.0036(2)
-	-	6674(2)	1-3	0.0005(1)/0.0008(1)/0.0010(1)
-	-	6761(2)	0,1	0.0028(6)/0.0008(1)
-	-	6778(2)	1	0.0021(2)/0.0023(2)
-	-	6823(2)	1	0.0015(1)
-	-	6842(2)	2,3	0.0036(1)/0.0044(2)
6866.4(6)	$(1/2 - 5/2)^+$	6866(2)	0 + 2	0.0080(1) + 0.0110(1)
7065.9(10)	$5/2^+$	7066(2)	1,2	0.0022(2)/0.0020(2)
7103.4(10)	$3/2$	7103(2)	1,3	0.0046(3)/0.0031(2)
7178.8(10)	$1/2^+$	7178(2)	2	0.0054(5)
7185.0(10)	$5/2^+$	-	-	-
7194.1(10)	$1/2^-$	7194(2)	-	-
7224.5(10)	$5/2$	-	-	-
-	-	7227(2)	0,1	0.0323(8)/0.011(1)
7233.5(10)	$(3/2, 5/2)^+$	-	-	-
7272.8(10)	$1/2^-$	7273(2)	0,1	0.025(6)/0.0075(3)
7362.1(10)	$3/2$	7361(2)	1	0.0010(2)
7397.0(16)	$7/2$	7398(2)	2,3	0.0070(3)/0.0082(3)

Table 4.4: Resonance parameters for the $^{34}\text{S}(p,\gamma)^{35}\text{Cl}$ Reaction. The first two columns list adopted E_x and E_r , as determined using a weighted average of present and previous works (see Table 4.3) and $S_p(^{35}\text{Cl}) = 6370.82$ keV [90]. The third column gives adopted J^π values as found through previous and present constraints. Previously measured (p,γ) resonance strengths $\omega\gamma$ are listed in the fourth column. The last two columns list the minimum and maximum resonance strengths will be used for the reaction rate calculations in this work

Adopted			Previous Work	Present Work	
E_x (keV)	E_r (keV)	J^π	$\omega\gamma$ (eV)	$\omega\gamma_{min}$ (eV)	$\omega\gamma_{max}$ (eV)
6427(2)	56(2)	(5/2 , 7/2) ⁻	-	$6.5(2)\times 10^{-24}$	$2.2(1)\times 10^{-22}$
6468(2)	97(2)	(1/2 , 3/2) ⁻	-	$4.2(5)\times 10^{-14}$	$4.2(5)\times 10^{-14}$
6491.5(8)	120.6(5)	(3/2 , 5/2) ⁺	-	$3.7(1)\times 10^{-13}$	$4.1(1)\times 10^{-13}$
6545(2)	174(2)	(1/2 , 3/2)	-	$7.4(13)\times 10^{-10}$	$4.1(1)\times 10^{-9}$
6643(2)	272(2)	(1/2 , 3/2) ⁻	-	$8.5(10)\times 10^{-6}$	$8.9(10)\times 10^{-6}$
6674(2)	303(2)	(1/2 - 7/2)	-	$2.4(2)\times 10^{-8}$	$4.1(8)\times 10^{-6}$
6761(2)	390(2)	(1/2 , 3/2)	-	$2.4(3)\times 10^{-4}$	$1.5(1)\times 10^{-3}$
6778(2)	407(2)	(1/2 , 3/2) ⁻	-	$9.4(12)\times 10^{-4}$	$1.0(1)\times 10^{-3}$
6823(2)	452(2)	(1/2 , 3/2) ⁻	-	$2.7(3)\times 10^{-3}$	$2.7(3)\times 10^{-3}$
6842(2)	471(2)	(3/2 / 7/2)	-	$3.3(1)\times 10^{-5}$	$7.0(3)\times 10^{-4}$
6866.4(6)	495.5(6)	5/2 ⁺	$2.5(12)\times 10^{-2}$	$3.0(3)\times 10^{-2}$	$4.7(5)\times 10^{-2}$
7065.9(10)	695.1(10)	5/2 ⁺	$7.0(40)\times 10^{-2}$	$2.2(1)\times 10^{-2}$	$2.2(1)\times 10^{-2}$
7103.3(10)	732.5(10)	3/2 ⁻	0.23(12)	$6.0(3)\times 10^{-2}$	1.30(7)
7178.6(10)	807.8(10)	1/2 ⁺	$8.1(4)\times 10^{-2}$	-	-
7185(1)	814(1)	5/2 ⁺	-	-	-
7194.1(10)	823.3(10)	1/2 ⁻	0.38(19)	-	-
7224.5(10)	853.7(10)	5/2	$7.6(38)\times 10^{-2}$	-	-
7233.5(10)	862.7(10)	(3/2 , 5/2) ⁺	0.52(10)	-	-
7272.8(10)	902.0(10)	1/2 ⁻	0.59(12)	11(2)	12(2)
7361.9(10)	991.1(10)	3/2 ⁻	0.85(17)	0.30(4)	3.0(6)
7397.4(16)	1026.6(16)	7/2 ⁻	0.19(10)	0.18(1)	0.19(1)

the STARLIB library [91]. Using resonance energies and strengths along with any associated uncertainties as inputs the STARLIB library is able to determine low, median and high thermonuclear reaction rates referring to the 16th, 50th and 84th cumulative rate distributions at each temperature. It should be noted that in this work the minimum reaction rate will refer to the STARLIB low rate for the minimum $\omega\gamma$ values. Similarly the maximum rate refers to the high rate with the larger $\omega\gamma$ values. Each input parameters is described as a probability density function which is then randomly sampled using standard Monte Carlo techniques and a reaction rate is computed from with eq. (2.19). A minimum sampling of 5000 is required to provide reproducibility to within a few percent.

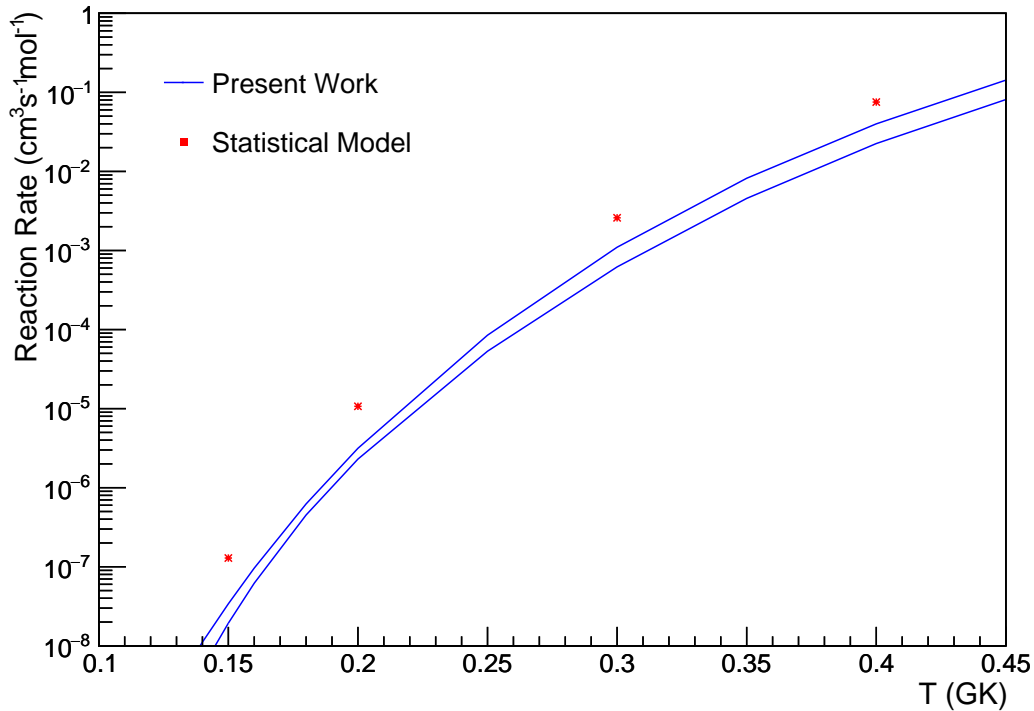


Figure 4.20: Thermonuclear $^{34}\text{S}(p,\gamma)^{35}\text{Cl}$ rates over typical nova peak temperatures. Shown in blue are the low and high rates from the present work and a rate calculated using a statistical model, shown in red [26, 43].

In addition to the resonant contribution, a non-resonant contribution, section 2.4.1, is required to calculate the reaction rate. This has not being previously measured, however Iliadis *et al.* have previously compiled a list of experimental values for other proton capture reactions in this mass region [26]. Values for the non-resonant contribution, $S(0)$ in eq. (2.21), are found to vary between 5 keV b and 400 keV b.

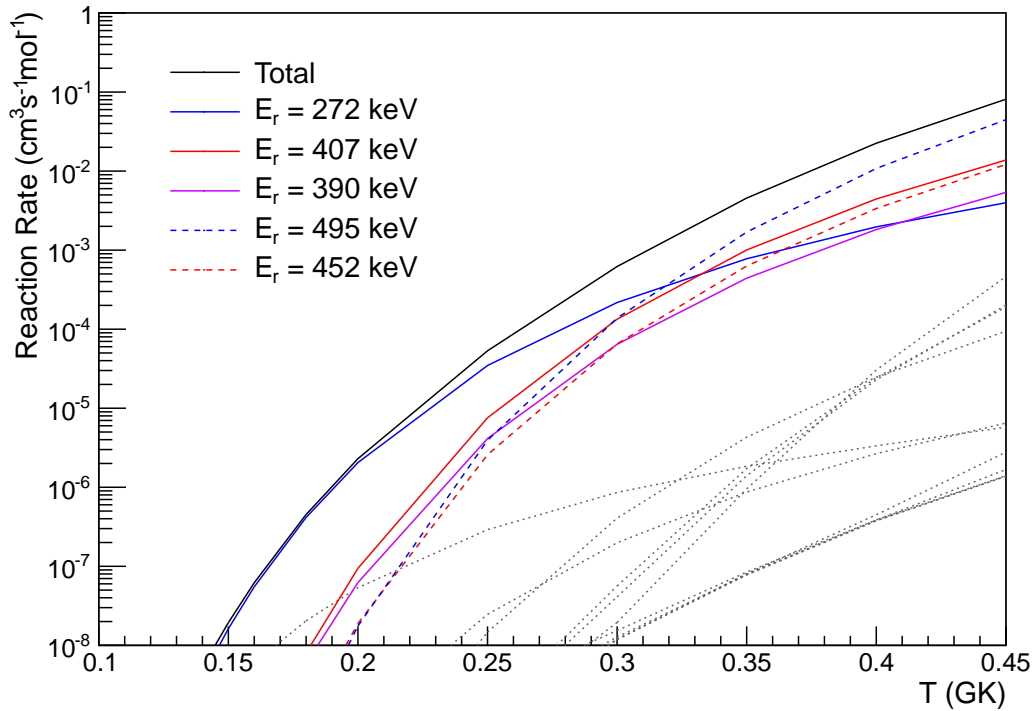


Figure 4.21: Minimum $^{34}\text{S}(p,\gamma)^{35}\text{Cl}$ thermonuclear reaction rate showing the contribution of individual states. In black is the total reaction rate, with the 5 strongest contributors at 0.25 GK labelled. In grey are the weakest contributions over typical nova peak temperatures.

Over typical nova peak temperatures this contribution is expected to be negligible, however multiple values will be trialled to determine the contribution to the reaction rate.

Using the values given in Table 4.4 minimum and maximum reaction rates have been calculated and are plotted in Figure 4.20 with a rate from a statistical model [26,43]. The ratio between the maximum and minimum reaction rate are found to vary between 4 and 1.4 with an average ratio of 1.75. The statistical model appears to overestimate both rates, in some cases by over an order of magnitude.

To investigate which states are the most significant contributors to the total reaction rate, calculations are performed for each individual resonance. As broad resonances were not observed in this work there are no interference terms required and the total reaction rate should be the incoherent sum of individual states. The minimum and maximum reaction rates are then plotted in Figures 4.21 and 4.22 along with

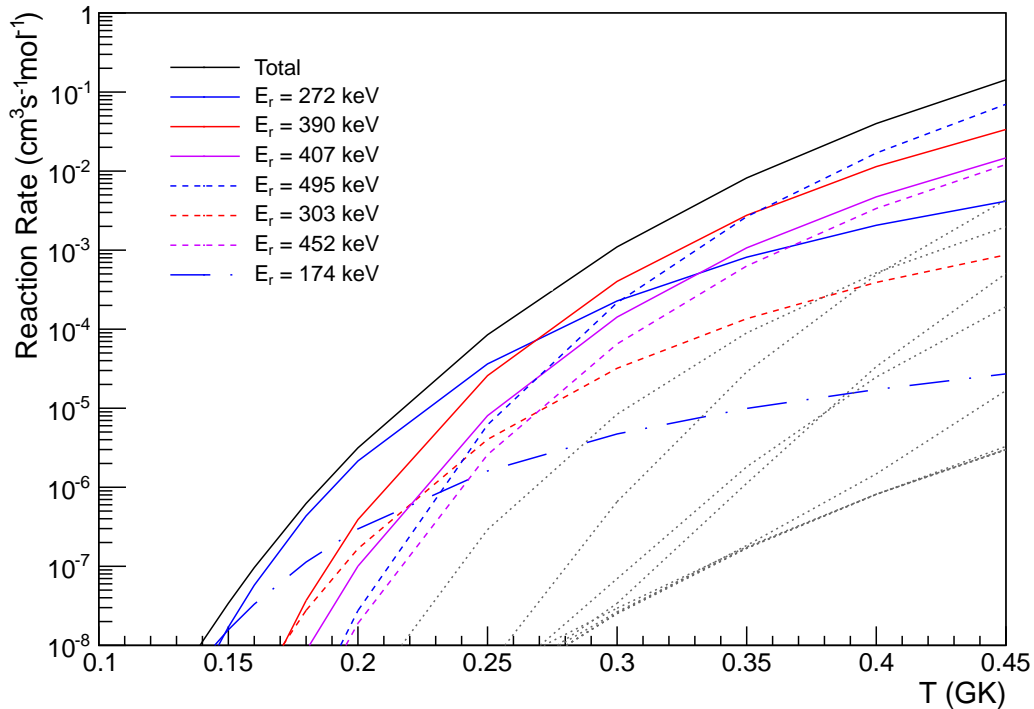


Figure 4.22: Maximum $^{34}\text{S}(p,\gamma)^{35}\text{Cl}$ thermonuclear reaction rate showing the contribution of individual states. In black is the total reaction rate, with the strongest contributors at 0.25 GK labelled. In grey are the weakest contributions over typical nova peak temperatures.

the individual contributions of each state. For the minimum reaction rate over typical nova peak temperatures it is clear that the reaction rate is dominated by five resonance with energies, 272(2), 407(2), 390(2), 495(2) and 452(2) keV. Up to 0.25 GK the rate is entirely dominated by the 272 keV resonance. The situation becomes more complicated for the maximum reaction rate. The same five resonances contribute strongly to the rate, however contributions from other resonances become more dominant. While the minimum reaction rate is dominated below 0.25 GK by the 273 keV resonance; the maximum rate has a significant contribution from the 174 keV resonance. The contribution of this resonance begins to fall after 0.15 GK and becomes insignificant at higher temperatures.

The experimental reaction rate calculated in this work and shown graphically in Figure 4.20 is valid over typical nova temperatures, but becomes invalid at higher temperatures. The reaction rate is based on experimental data, however if the temperature of the environment is too high the reaction would no longer proceed

through the experimentally known states. For example the highest energy state included in the $^{34}\text{S}(p,\gamma)^{35}\text{Cl}$ reaction rate calculation was the 9.194 MeV state, which corresponds to a proton bombardment energy of 2.9 MeV [31]. If the temperature is sufficiently high and protons within the environment have energies > 2.9 MeV the reaction rate can no longer be used. The maximum possible temperature for which the reaction rate is valid, T_{match} , can be calculated using:

$$E'(T_{match}) + \delta E'(T_{match}) = E_{max}, \quad (4.8)$$

where E_{max} is the maximum experimental energy and E' and $\delta E'$ are the location and width of the effective temperature range for which the experimental reaction rate is valid. The values E' and $\delta E'$ can be approximated as the Gamow peak and width eqs. (2.17) and (2.18) to calculate T_{match} [92]. Using eq. (4.8) with the maximum proton energy used in this work, $E_{max} = 2.9$ MeV, it can be seen that the calculated reaction rate is valid up to ~ 2.7 GK.

Beyond this temperature the reaction rate must be calculated using a statistical model. For this the old reaction rate, calculated from a statistical model [26], is normalised to the present experimental minimum and maximum reaction rates. Finally, corrections must be made to the reaction rate to account for reactions involving excited ^{34}S nuclei, see section 2.4.5 for details. The reaction rate is corrected for stellar temperature using the SEFs found in [43]. For the $^{34}\text{S}(p,\gamma)^{35}\text{Cl}$ reaction, however the effect of reactions on excited nuclei, becomes significant only for temperatures $T_9 > 5$ GK and as the statistical reactions rates include the SEFs, the calculated reaction rate does not need to be modified. The new recommended $^{34}\text{S}(p,\gamma)^{35}\text{Cl}$ reaction rate which will be used to calculate the $^{32}\text{S}/^{34}\text{S}$ isotopic ratio is shown in Table 4.5. Using eq. (2.32) a reverse rate is also calculated for the minimum and maximum rate which will be necessary when determining the astrophysical impact of the new experimental rates, as detailed in the following section.

4.6 Astrophysical Impact of the $^{34}\text{S}(p,\gamma)^{35}\text{Cl}$ Reaction Rate

Using the new reaction rates seen in Table 4.5 calculations were performed using a one-dimensional, spherically symmetric, implicit hydrodynamical code, known as

Table 4.5: New recommended Minimum and Maximum Reaction Rate for the $^{34}\text{S}(p,\gamma)^{35}\text{Cl}$. Shown in the first column is the temperature in GK with the minimum and maximum recommended reaction rate in the final columns in units of $N_A \langle \sigma v \rangle \text{ cm}^3 \text{ mol}^{-1} \text{ s}^{-1}$

T ₉ GK	Minimum Reaction Rate	Maximum Reaction Rate
0.01	8.32×10^{-44}	1.92×10^{-42}
0.015	7.97×10^{-35}	2.69×10^{-33}
0.02	3.27×10^{-30}	9.08×10^{-29}
0.03	5.17×10^{-23}	5.42×10^{-23}
0.04	4.27×10^{-19}	4.28×10^{-19}
0.05	9.12×10^{-17}	9.18×10^{-17}
0.06	3.24×10^{-15}	3.37×10^{-15}
0.07	4.32×10^{-14}	5.23×10^{-14}
0.08	3.39×10^{-13}	5.97×10^{-13}
0.09	2.07×10^{-12}	5.59×10^{-12}
0.1	1.12×10^{-11}	3.95×10^{-11}
0.15	1.94×10^{-8}	3.40×10^{-8}
0.2	2.30×10^{-6}	3.15×10^{-6}
0.3	6.20×10^{-4}	1.10×10^{-3}
0.4	2.25×10^{-2}	4.00×10^{-2}
0.5	2.31×10^{-1}	4.09×10^{-1}
0.6	1.19×10^0	2.18×10^0
0.7	4.36×10^0	8.31×10^0
0.8	1.33×10^1	2.55×10^1
0.9	3.53×10^1	6.57×10^1
1	8.14×10^1	1.46×10^2
1.5	1.17×10^3	1.83×10^3
2	4.39×10^3	6.44×10^3
3	1.55×10^4	2.12×10^4
4	3.35×10^4	4.59×10^4
5	5.66×10^4	7.73×10^4
6	8.29×10^4	1.13×10^5
7	1.12×10^5	1.53×10^5
8	1.40×10^5	1.91×10^5
9	1.69×10^5	2.31×10^5
10	1.97×10^5	2.70×10^5

SHIVA [10]. These calculations were not performed by the author and the mechanics of the nova model are beyond the scope of the thesis and will not be discussed in detail. This work is concerned only with the final result of the calculations, however the input parameters and assumptions of the model will be discussed.

The code SHIVA uses a Lagrangian system, where the location of individual particles is tracked, to solve standard differential equations for hydrodynamical evolution. These include the conservation of mass, momentum and energy as well as energy transport by radiation and convection. A diffusion equation is used to model the mixing between adjacent convective shells. Additional corrections are included to account for the optical opacity of the white dwarf with regards to radiation transport. The model is linked to a reaction rate network, for which the new $^{34}\text{S}(p,\gamma)^{35}\text{Cl}$ rate calculated in the present work has been included.

As elements in the Si-Ca mass region are produced only in the heaviest ONe white dwarf stars, calculations are performed for a $1.35 M_{\odot}$ white dwarf accreting matter from a companion star at the rate of $2 \times 10^{-10} M_{\odot} \text{yr}^{-1}$. There is assumed to be pre-mixing, to a level of 50%, of the accreted matter from the companion star and the outer layers of the white dwarf prior to the nova explosion. This level of pre-mixing has previously been found to mimic mixing at the core-envelope level [93]. The total mass of envelope ejected into the ISM was $M_{ej} = 0.00455 M_{\odot}$ or 9.043×10^{27} g. Using these input parameters separate calculations were performed by Jordi José [94] for the old statistical rate [6] and the high and low rates calculated in this work. Results from the calculation are the mass fraction of individual nuclei relative to the total ejected material and are shown in Table 4.6 for all reaction rates.

The new $^{34}\text{S}(p,\gamma)^{35}\text{Cl}$ reaction rate is found to affect the production of nuclei only in the S-Ca mass region. Specifically only nuclei with masses $A = 34-39$ are found to be affected by the new rates with the mass fractions of other nuclei found to be consistent within 1%. Using these mass fractions it is possible to extract a new $^{32}\text{S}/^{34}\text{S}$ isotopic ratio for classical novae of 82–95. The astrophysical implications of this new ratio and the effect of the $^{34}\text{S}(p,\gamma)^{35}\text{Cl}$ reaction rate on nucleosynthesis in classical novae will be discussed further in chapter 5.

Table 4.6: Mean composition of the ejecta from a $1.35 M_{\odot}$ ONe white dwarf novae event. The mass of different nuclei species is given in terms of the mass fraction of the total ejected material in the novae event. Shown are the composition using the old reaction rate derived from a statistical model [6] and the low and high rates from the present work shown in Table 4.5. The $^{34}\text{S}(p,\gamma)^{35}\text{Cl}$ reaction rate is found to affect the production of nuclei only in the S–Ca mass region.

Nuclide	Mass Fractions		
	Old Rate [6]	Low Rate	High Rate
^{31}P	8.73E-03	8.72E-03	8.72E-03
^{32}S	5.26E-02	5.26E-02	5.26E-02
^{33}S	7.99E-04	8.00E-04	8.00E-04
^{34}S	3.62E-04	6.43E-04	5.55E-04
^{35}Cl	3.83E-04	1.79E-04	2.41E-04
^{36}Ar	5.11E-05	2.59E-05	3.42E-05
^{37}Cl	1.43E-04	8.76E-05	1.07E-04
^{38}Ar	2.40E-05	1.93E-05	2.10E-05
^{39}K	5.95E-06	5.78E-06	5.84E-06
^{40}Ca	3.06E-05	3.06E-05	3.06E-05

Chapter 5

$^{34}\text{S}(^3\text{He},\text{d})^{35}\text{Cl}$ Discussion

The $^{34}\text{S}(p,\gamma)^{35}\text{Cl}$ reaction rate was studied using the $^{34}\text{S}(^3\text{He},\text{d})^{35}\text{Cl}$ reaction and a Q3D magnetic spectrometer. The aim of this experiment was to reduce uncertainties in the reaction rate by performing a detailed spectroscopic study of the 6–7 MeV excitation region in ^{35}Cl which is relevant at temperatures seen in classical novae. With a reduced reaction rate it was hoped that it would be possible to use the $^{32}\text{S}/^{34}\text{S}$ isotopic ratio as a diagnostic tool to determine pre-solar grain paternity. A total of 10 states were observed in this work for the first time in the relevant energy region and new spin and parity information is now available for 7 previously observed states. This spectroscopic information was used to calculate the first experimental $^{34}\text{S}(p,\gamma)^{35}\text{Cl}$ reaction rate. A hydrodynamical reaction rate calculation was then performed by Jordi José [94] using the new reaction rate and a $^{32}\text{S}/^{34}\text{S}$ isotopic ratio of 82–95 was found, which is significantly more constrained than the value using the previous reaction rate. With current Type II supernova models predicting a ratio of 19–38, this new ratio it should now be possible to distinguish between pre-solar grains from Type II supernova and classical novae. This chapter will discuss the comparison of the states observed in this work with previous studies and the implications of these results with regards to the $^{34}\text{S}(p,\gamma)^{35}\text{Cl}$ reaction rate and the main sources of uncertainties which should be addressed to further improve this rate.

5.1 Discussion of the Spectroscopy of ^{35}Cl

In total 22 states were observed across the focal plane of which 10 have not previously been observed. Below 6.8 MeV this nucleus has been studied primarily in (α, p) reactions [28]. A comparison of the states seen in the previous study and the present work are shown in Table 5.1. While there is little agreement between states observed in the present ($^3\text{He}, d$) study and the previous (α, p) results this was not unexpected. Due to momentum matching only high spin states would have been populated in the (α, p) reaction, so the discovery of a large number of low spin states is unsurprising. States which were observed in both the (α, p) and ($^3\text{He}, d$) studies were also known to be populated in (p, γ) reactions for which the agreement is good with the present data. With regards to spin and parity the (α, p) study was unable to extract any information so it is not possible to compare this.

Above 6.8 MeV ^{35}Cl has been studied extensively through (p, γ) reactions [29, 30] with (α, p) [28] studies also populating states in this energy region. The comparison of the states populated in different reaction mechanisms can be seen in Table 5.2. It is clear that there is good agreement between the states populated in (p, γ) and ($^3\text{He}, d$) reactions. The comparison of the ($^3\text{He}, d$) and (α, p) reactions are poor, but as has been previously discussed due to momentum matching the two reaction mechanisms should populate different states. This is further supported by disagreements between the (p, γ) and (α, p) data.

The differences between the different reactions can also be explained in the way the states are populated. Both the $^{34}\text{S}(^3\text{He}, d)$ and $^{34}\text{S}(p, \gamma)$ reactions populate states in ^{35}Cl by transferring a single proton. It is possible to conclude that states populated in these reactions are due to a single proton excitation. The $^{32}\text{S}(\alpha, p)$ reaction, however requires 3 particles to be transferred in order to populate states in ^{35}Cl . It is possible that these states are not due to single particle excitations, but involve multiple particle excitations. If the states in the first column of Table 5.1 require multiple particle excitations, a single proton transfer reaction, such as ($^3\text{He}, d$) or (p, γ) , will not be able to populate these states. As the astrophysical $^{34}\text{S}(p, \gamma)$ reaction involves a single proton transfer the states known from the $^{32}\text{S}(\alpha, p)$ [28] are likely not important when calculating the thermonuclear reaction rate.

While the agreement with the (p, γ) studies is good the resolution of this experiment was insufficient to resolve all known states. Examples of this include the states at

Table 5.1: Nuclear structure of ^{35}Cl for states within $6.2 < E_x < 6.8$ MeV. The first column give the energy of states observed in previous (α ,p) studies [28] with the second column giving the energy of states observed in this work.

Previous Work [28]	Present Work
E_x (keV)	E_x (keV)
-	6284(2)
-	6329(2)
6380(4)	6377(2)
6402(4)	-
-	6427(2)
-	6468(2)
6492(4)	6491(2)
-	6545(2)
-	6643(2)
6656(4)	-
-	6674(2)
6681(4)	-
-	6761(2)
-	6778(2)
6783(3)	

7225 keV and 7234 keV which appear as a single peak with an energy of 7228 keV. The triplet of states at 7179, 7185 and 7195 keV lines could not be fully resolved, with only the 7179 and 7195 keV states being observed. Where spin and parity were previously known the agreement with the values extracted from the angular distributions seen in section 4.4 is good and in several cases for states above 7 MeV definite spin and parity assignments can now be made.

5.2 Discussion of the $^{34}\text{S}(\text{p},\gamma)^{35}\text{Cl}$ reaction rate and its role in classical novae

Using the spectroscopic information extracted in this work it was possible to calculate the first experimental $^{34}\text{S}(\text{p},\gamma)^{35}\text{Cl}$ reaction rate. Two rates were calculated, referred to as the high and low rate, which are used to find the uncertainties in the nucleosynthesis of different isotopes. It was found the new rates only affect the production of nuclei in the $A = 34\text{--}39$ mass region. The production of all other nuclei found is to be consistent within 1% between the two rates and the statistical rate.

In particular the production of five different nuclei are found to vary significantly within the present experimental uncertainties. These nuclei have been extracted from Table 4.6 and reproduced in Table 5.3 for clarity. While only a few species of nuclei are found to be affected significantly by the new rate this result is unsurprising and was predicted by a sensitivity study [6]. The reduction of uncertainties in the production of these nuclei, however is significantly different than seen in the sensitivity study. The production of all nuclei with $A = 34\text{--}39$ varies by less than a factor of 2 between the low and high rates. Comparing this with uncertainties from the old statistical model, shown graphically in Figure 1.2, it is clear that the new spectroscopic information extracted in the present work has had a significant effect on the $^{34}\text{S}(\text{p},\gamma)^{35}\text{Cl}$ reaction rate. Given that the observational uncertainties of pre-solar grains are a similar factor it is clear that the $^{34}\text{S}(\text{p},\gamma)^{35}\text{Cl}$ reaction rate is now sufficiently well constrained for current classical nova-model predictions. It should be noted, however this result is only for a single nova model and other models may predict a different result. A full 3D hydrodynamical calculation would be required to determine the effect of the new rate.

Table 5.2: Energy of ^{35}Cl states within $6.8 < E_x < 7.4$ MeV excitation energy. The first two columns the energies of states observed in previous (p, γ) [29,30] and (α ,p) studies. The final column shows the energy of states observed in this work.

Previous Work		Present Work
E_x (keV) (p, γ) [29,30]	E_x (keV) (α ,p) [28]	E_x (keV)
-	6802(4)	-
-	-	6823(2)
-	-	6842(2)
6866.4(6)	6866(4)	6866(2)
-	6894(4)	-
-	6947(4)	-
-	6989(4)	-
7065.9(10)	-	7066(2)
7103.4(10)	7103(4)	7103(2)
-	7121(4)	-
7178.8(10)	7179(4)	7178(2)
7185.0(10)	-	-
7194.1(10)	-	7194(2)
-	7210(4)	-
7224.5(10)	-	-
-	-	7227(2)
7233.5(10)	-	-
7272.8(10)	-	7273(2)
-	7348(4)	-
7362.1(10)	-	7361(2)
7397.0(16)	-	7398(2)

Table 5.3: Mean composition of the ejecta from a 1.35 M_{\odot} ONe white dwarf novae event. This table is a reproduction of Table 4.6, but showing only the species of nuclei where the differences between the low and high reaction rate are $>1\%$. As before the mass of the different nuclei is given in terms of the mass fraction of the total ejected material in the novae event and the rates shown are from a statistical model [6] and the low and high rates from the present work.

Nuclide	Mass Fractions		
	Old Rate [6]	Low Rate	High Rate
^{34}S	3.62E-04	6.43E-04	5.55E-04
^{35}Cl	3.83E-04	1.79E-04	2.41E-04
^{36}Ar	5.11E-05	2.59E-05	3.42E-05
^{37}Cl	1.43E-04	8.76E-05	1.07E-04
^{38}Ar	2.40E-05	1.93E-05	2.10E-05

The experimental $^{34}\text{S}(p,\gamma)^{35}\text{Cl}$ reaction rate calculated in the present work is found to be at some temperatures an order of magnitude less than the reaction rate calculated from the statistical model. This result is not unsurprising as there are several cases where statistical models fail to reproduce experimental reaction. Iliadis *et al.* [26] presented several cases where the statistical model overestimates experimental reaction rates. The main assumption of the statistical model is that there is a sufficiently high level density in the compound nucleus for which reactions can proceed through. This criteria is not always true and the statistical models are presented with a lower limit temperature below which the statistical model should not be used. For example the statistical $^{34}\text{S}(p,\gamma)^{35}\text{Cl}$ reaction rate is given with a lower limit temperature of 0.025 GK [43] which suggests that this rate should be suitable for modelling classical nova events. A comparison with the experimental reaction rate shows this is clearly not true, with the statistical model overestimating the reaction rate over nova temperatures. At higher temperatures, however the statistical and experimental reaction rates are comparable. This suggests that the statistical model is valid at high temperatures, however the assumptions used to determine the lower temperature limit should be revised.

The main aim of this experiment was to determine whether the paternity of pre-solar grains could be determined by measuring the $^{32}\text{S}/^{34}\text{S}$ isotopic ratio. With the present data it can be concluded that it is now possible to distinguish between pre-solar grains

from a classical novae and a Type II supernova. By using this isotopic ratio in conjunction with others such as the $^{32}\text{S}/^{33}\text{S}$, $^{12}\text{C}/^{13}\text{C}$, $^{14}\text{N}/^{15}\text{N}$ and $^{29,30}\text{Si}/^{28}\text{Si}$ ratios, it may now be possible to devise a robust test of isotopic measurements which can be used to determine pre-solar grain paternity.

The largest source of discrepancy between the high and low rates is due to the uncertainty in the spin assignments of three resonances with energies $E_r = 174$, 390 and 495 keV. As shown in section B.2 the $\omega\gamma$ values are dependent upon the angular momentum transferred by the proton. This affects both the extracted spectroscopic factors and the penetrability factor P_ℓ . For cases where multiple angular momentum transfer values are possible $\omega\gamma_{min}$ and $\omega\gamma_{max}$ can differ by several orders of magnitude. The difference between the minimum and maximum rate is almost entirely due to the inability to make definite spin parity assignments for all the states, particularly the $E_r = 174$, 390 and 495 keV resonances. A precise determination of these spin states could further be used to constrain the prediction of the nova model. In addition the resonance strengths of all the states in this work was calculated using assumptions to determine a value for the proton partial widths of the states. Both of these issues could be addressed by performing a direct measurement of the (p,γ) reaction where the resonance strengths $\omega\gamma$ are measured directly. Now the energies of these states are known it may be possible to measure this reaction directly using the DRAGON spectrometer [95] at TRIUMF or with a similar spectrometer. It should be noted that as the present uncertainties of the reaction rate are comparable to the observational uncertainties a direct measurement will not further constrain the nova model.

Chapter 6

$^{26}\text{Mg}(^3\text{He},\text{d})^{27}\text{Al}$ Analysis and Results

The results of the spectroscopic studies of ^{27}Al through $(^3\text{He},\text{d})$ and (α,t) transfer reactions will be presented in two parts. This chapter will present the results of the $^{26}\text{Mg}(^3\text{He},\text{d})^{27}\text{Al}$ reaction performed at the MLL facility in Garching using the Q3D magnetic spectrometer. The results of the (α,t) study will be discussed separately in chapter 7. The implication of the results in regards to the $^{26}\text{Al}(\text{n},\text{p}/\alpha)$ reaction rate will then be discussed together in chapter 8. The $^{26}\text{Mg}(^3\text{He},\text{d})^{27}\text{Al}$ reaction was performed using a 20 MeV ^3He beam which was accelerated and impinged on the targets listed in Table 3.3, primarily an enriched $20\ \mu\text{g}/\text{cm}^2$ ^{26}MgO target on a carbon backing of $8\ \mu\text{g}/\text{cm}^2$ thickness which was used for the main measurements. Scattered particles were analysed at the focal plane of a Q3D magnetic spectrometer. Reaction products were measured at 5 angles, 5, 10, 15, 20, and 25 degrees with the aim of identifying excited states and extracting angular distributions. This should allow low spin states to be identified which will be used with other experimental data, particularly the $^{26}\text{Al}(\alpha,\text{t})$ study, to improve reaction rates for the $^{26}\text{Al}(\text{n},\text{p}/\alpha)$ reactions.

6.1 Focal Plane Identification

As discussed in section 4.1, states cannot be identified without first using particle gates to identify the deuteron reactions channels. Figure 6.1 shows the 5° spectrum

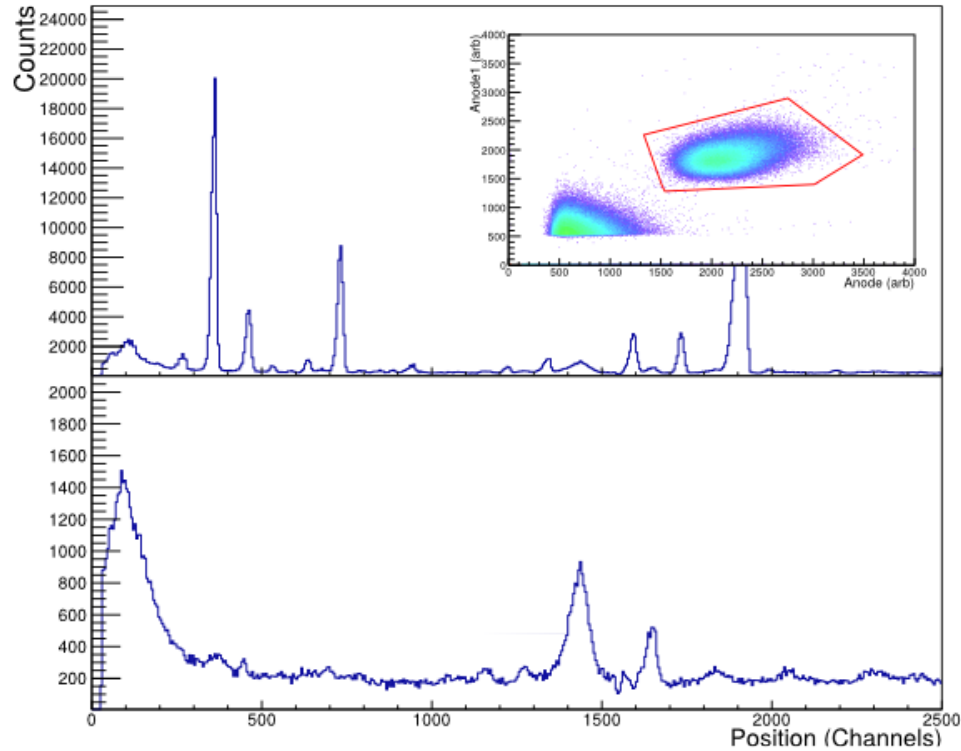


Figure 6.1: Focal plane spectrum for ^{26}MgO at target 5° . Top: ungated focal plane spectrum showing all reaction products. Inset: MWPC1 Anode charge versus MWPC2 Anode charge, a gate is placed around the deuteron locus, the second particle locus (bottom left) is protons. Bottom: deuteron gated focal plane spectrum for ^{26}MgO at 5° . Peaks seen in this spectrum are due to $(^3\text{He},d)$ reactions on the experimental target.

for the ^{26}MgO target, both before and after deuteron particle gates have been applied. It should be noted that while only a δE versus δE gate is shown in the inset a δE versus E gate has also been applied. Two loci are seen in the PID plot corresponding to the $(^3\text{He},p)$ and $(^3\text{He},d)$ reaction channels. It is expected that inelastic reaction products are seen at the focal plane, however it is not possible to see these reactions in the PID plot due to the preamplifier settings used to set up the MWPCs.

Contaminant peaks can be observed in the spectra most notably from reactions on the carbon backing and the oxide layer of the target. It is also necessary to identify states from reactions on ^{24}Mg present within the target. These states were identified by performing measurements on a $27.8\mu\text{g}/\text{cm}^2$ ^{nat}C target and a $40\mu\text{g}/\text{cm}^2$ ^{nat}MgO target on $8.6\mu\text{g}/\text{cm}^2$ carbon backing. The overlay of the three targets showing the primary contaminant states can be seen in Figure 6.2. An important feature that

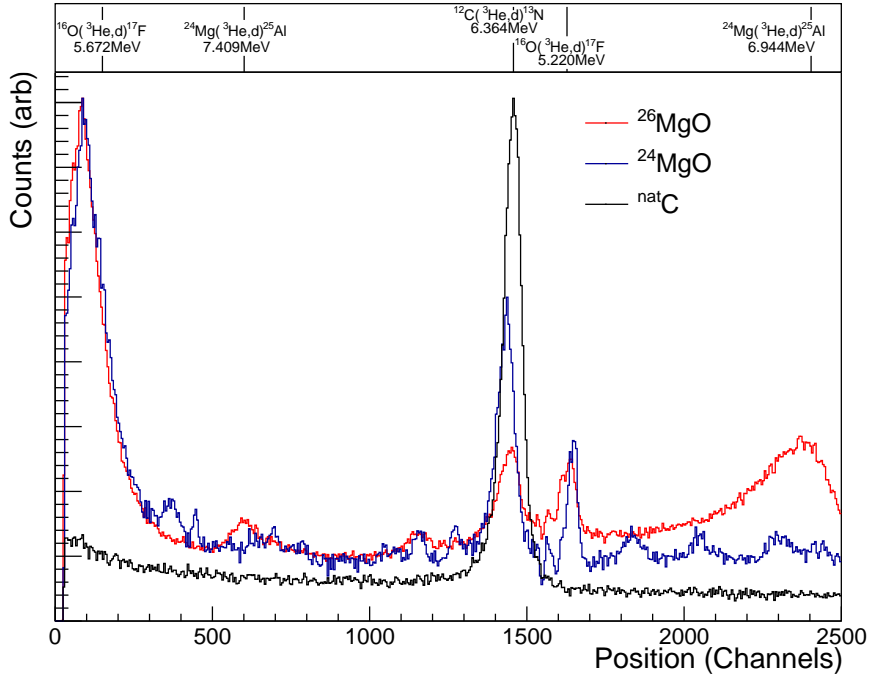


Figure 6.2: Bottom: 5° focal plane spectra for ^{26}MgO (blue), ^{24}MgO (red) and ^{nat}C (black) targets. The spectra have been scaled to appear on the same plot. Top: predicted position of primary contaminant states on the Q3D focal plane calculated using the nukestim code [74].

can be seen in Figure 6.2 is the dip in intensity around channel ~ 1550 . This is observed in the same position for all targets and measurement angles and is believed to be caused by incomplete charge collection of a cathode strip in the MWPC which determines position. This region is subsequently excluded when fitting spectra.

6.1.1 Background Subtraction

Before fitting the spectra, background subtraction is first performed. The shape and magnitude of the background is unknown and the fit result will be invalid without any prior subtraction. It can be assumed that the background in the spectra is a result of individual states as well as a flat or linear background from the target contaminants. This linear background is attributed to the population of broad high energy states in the contaminant nuclei [96]. The particles observed at the focal plane detector would therefore be seen over a wide range of energies giving rise to a linear background.

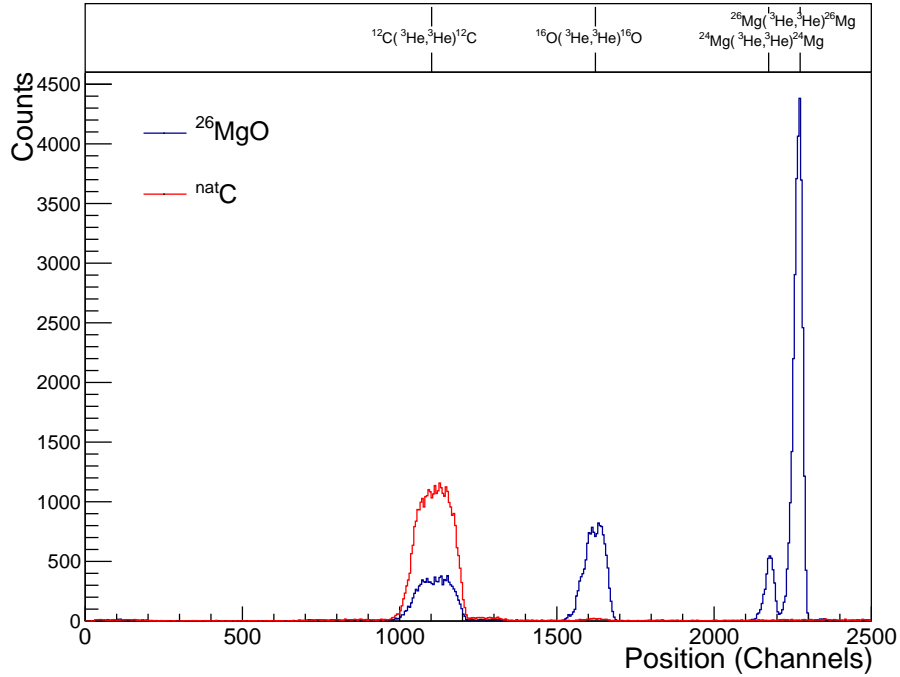


Figure 6.3: Focal plane spectrum at 30° with the beam optics set to focus the elastically scattered ^3He beam. Shown is the elastic scattering of ^3He on ^{26}MgO (blue) and ^{nat}C (red) targets. The ratio of peaks in the two spectra is used for target characterisation.

As mentioned in the previous section the primary sources of background are expected to be due to ^{12}C , ^{16}O and ^{24}Mg . These sources will be removed from the spectra in sequence to produce a spectrum free of contaminant background. It should be noted that due to the target thickness the position of narrow states will be shifted and broadened between the different spectra. As the position of narrow individual states cannot be subtracted directly without over/under-subtraction of the spectra so only the linear background will be removed from the spectra. For broad states, however the effect of target thickness is negligible and these will be removed from the spectra. The procedure for background subtraction will be discussed below specifically for the 5° spectra, but has been performed at all angles.

6.1.1.1 Carbon Background subtraction

The first background to be removed will be from carbon contaminants. This can be accomplished by removing a proportion of the ^{nat}C target spectrum determined by the relative carbon content. The amount of carbon which should be subtracted

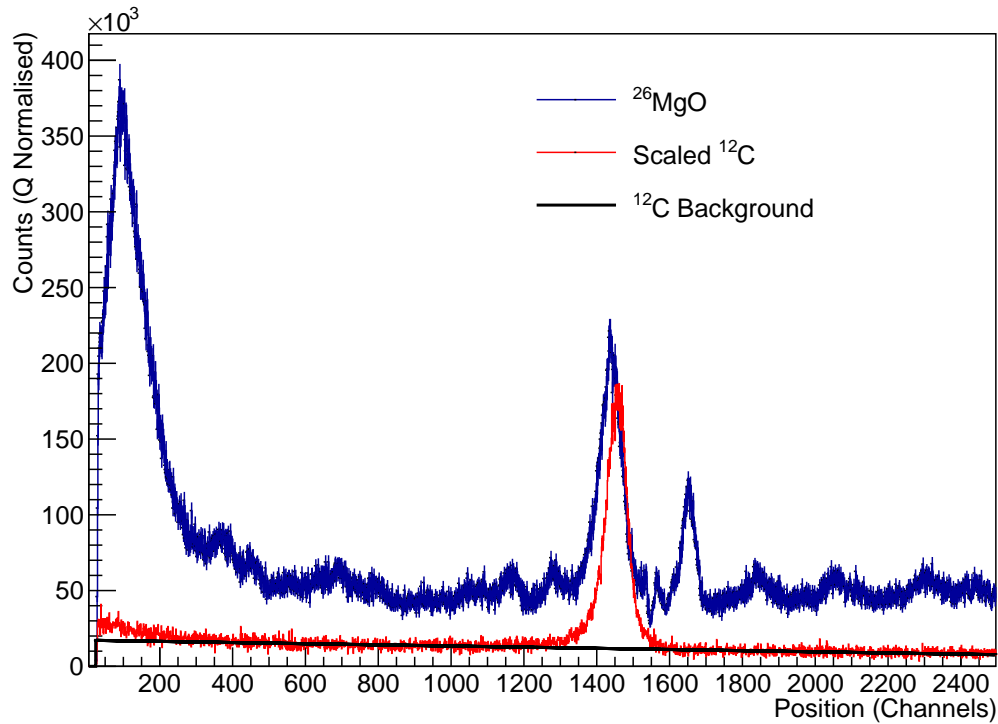


Figure 6.4: Overlay of charge normalised deuteron focal plane spectra for ²⁶MgO (blue) and ^{nat}C (red) targets. The carbon spectra has been scaled to estimate the carbon contribution to the background for the ²⁶MgO target. In black is the estimated carbon background obtained from a fit of the ^{nat}C target data, which will be subtracted from the ²⁶MgO spectrum.

can be estimated based on the thickness of carbon in the targets. Based on the quoted carbon target thickness, $8\mu\text{g}/\text{cm}^2$ for the ²⁶MgO target $27.8\mu\text{g}/\text{cm}^2$ for the ^{nat}C, it would be expected that the relative carbon content is 0.29. A more accurate measurement can be obtained, however from elastic scattering data. Figure 6.3 shows focal plane spectra for the elastic scattering of ³He nuclei off the ²⁶MgO and ¹²C targets. The ratio of the carbon peaks in the two targets will be used to calculate the magnitude of the carbon background which must be removed from the ²⁶MgO spectrum. Integrating the two peak areas and normalising to the beam current gives a relative carbon content of 0.422(4). While the two calculated values are significantly different which suggests the quoted target thickness were inaccurate. The two values, however should be consistent within the two sigma level.

The carbon spectra is scaled by 0.42 and is overlaid with the ²⁶MgO spectrum in Figure 6.4. The effect of target thickness can be seen in the shifting of the carbon

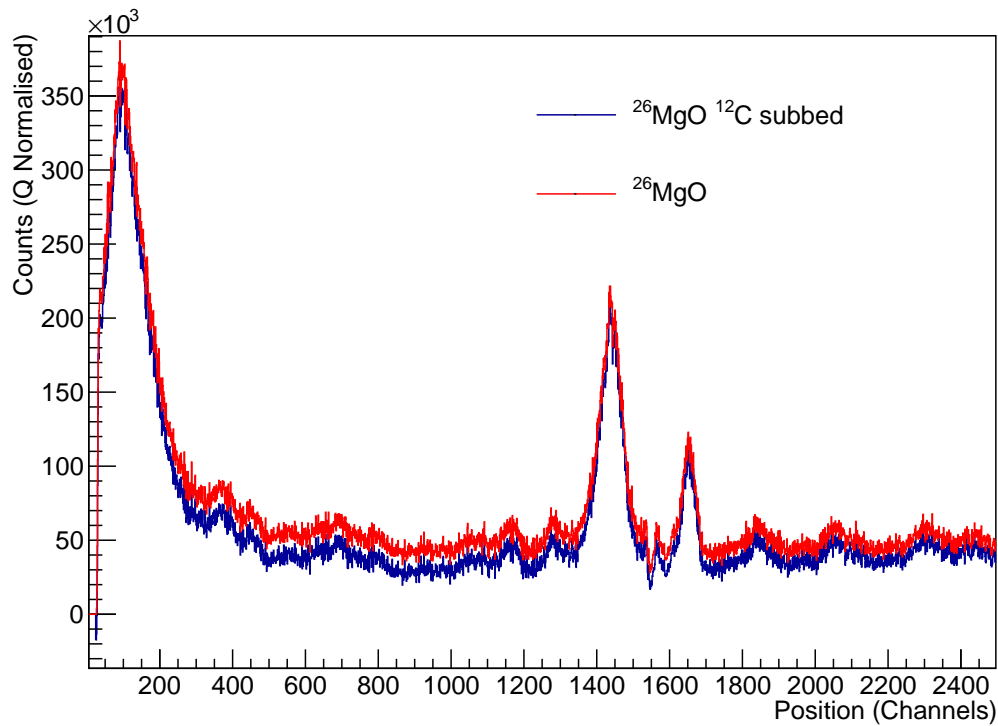


Figure 6.5: Deuteron focal plane spectra for ^{26}MgO target before (red) and after carbon background subtraction. The black fit seen in Figure 6.4 has been subtracted from the ^{26}MgO spectra to produce the spectrum seen in blue.

peak position. For this reason the full scaled spectrum will not be subtracted. Instead the background is fitted with a peak plus polynomial background, the result of this fit can be seen as a solid black line in Figure 6.4. The polynomial background obtained from this fit is then subtracted from the ^{26}MgO spectrum with the final result seen in Figure 6.5. The same approach must also be applied to the ^{24}MgO spectrum to prevent over subtraction of carbon when the ^{24}Mg content is removed.

6.1.1.2 Oxygen Background subtraction

It was found that the background due to oxygen could not be effectively be removed from the spectra. Measurements on a SiO target were performed for calibration purposes and to measure the oxygen background. The $(^3\text{He},d)$ spectra on the SiO target can be seen in Figure 6.6. Several broad states in ^{29}P can be seen in this spectra which makes it difficult to determine the shape of the oxygen background.

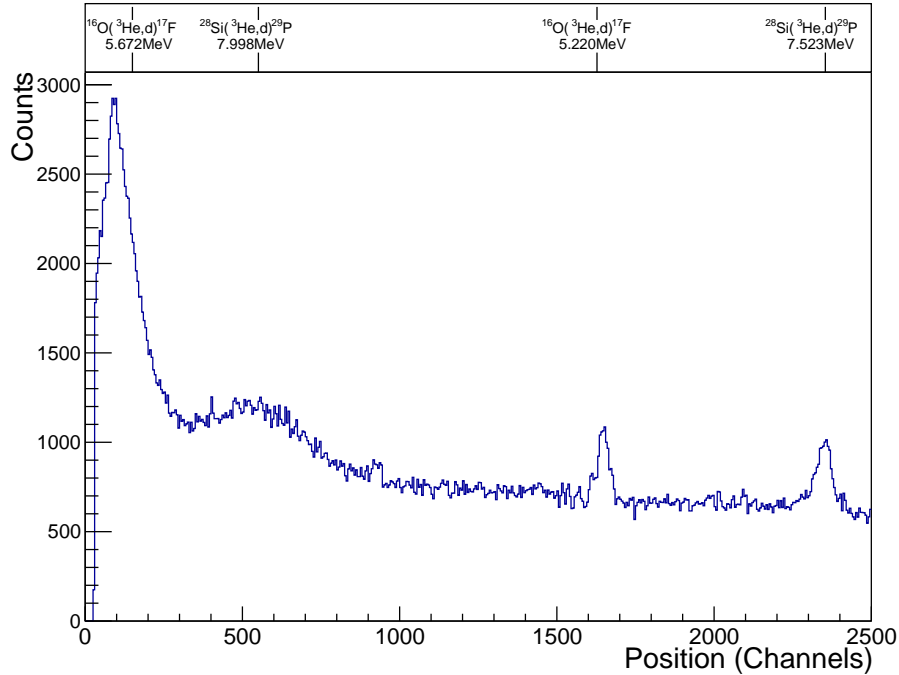


Figure 6.6: Focal plane spectrum for $(^3\text{He},d)$ reactions on a SiO Target. Marked in the top panel are the major states observed at the focal plane.

As the background shape cannot be determined, it was decided not to subtract the oxygen background from the ^{26}MgO spectrum.

6.1.1.3 ^{24}MgO Background Subtraction

Using inelastic scattering data it was possible to calculate the amount of ^{24}Mg present within the enriched ^{26}MgO target. From the ratio of ^{24}Mg inelastic peaks, seen in Figure 6.7, it was deduced the ^{26}MgO target was comprised of 95% ^{26}Mg and 5% ^{24}Mg . The states populated in the $^{24}\text{Mg}(^3\text{He},d)^{25}\text{Al}$ reaction are found to be sufficiently broad that target effects are expected to be negligible. Scaling the spectra obtained using the ^{24}MgO target and subtracting it should remove the ^{24}Mg contribution from the ^{26}MgO carbon background subtracted spectrum. Figure 6.8 shows the initial carbon-subtracted ^{26}MgO spectra and the proportion of the ^{24}MgO which is subtracted. Removing this spectrum will also remove some of the unknown oxygen background as well as a small proportion of ^{26}Mg present within the ^{24}MgO target. Cross sections of ^{26}Mg states would therefore be expected to be underestimated, however when accounting for other sources of uncertainties such as target thickness this is expected to be negligible. The final spectra which

will be fitted to identify states can be seen in Figure 6.9 overlaid with the original un-subtracted spectra for comparison. Similar plots are produced at all angles, but are not presented here.

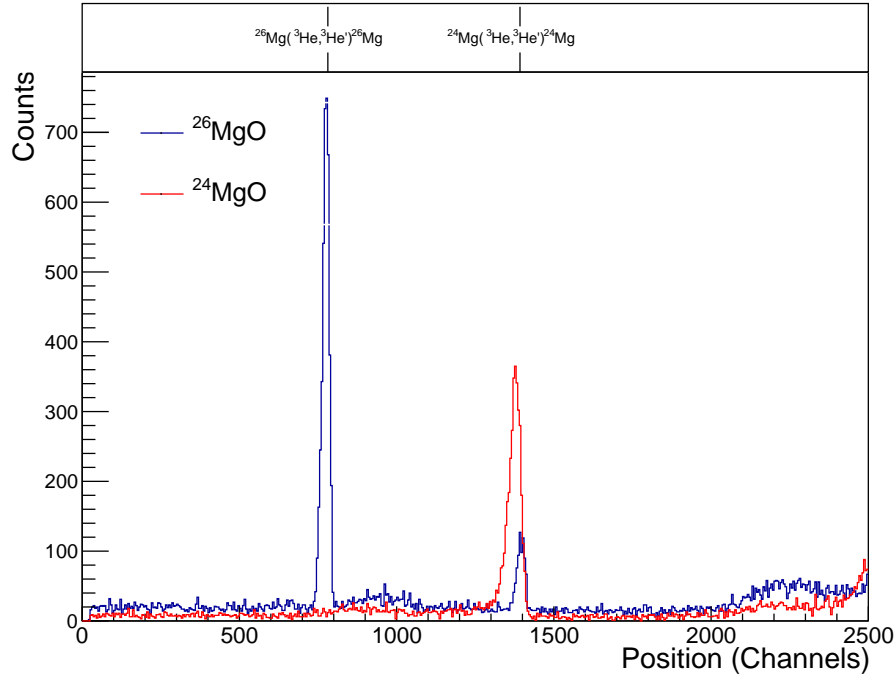


Figure 6.7: Inelastic scattering of ^3He off ^{26}MgO (blue) and ^{24}MgO (red) targets. The ratio of ^{24}Mg peaks in the two spectra are used for target characterisation.

6.2 Focal Plane Calibration

Unlike the data, presented in chapter 4, it is not possible to perform an internal calibration of the ^{26}MgO target. The density of states in ^{27}Al is too high at the covered energy region, $\sim 13\text{-}13.5$ MeV, and the nucleus has only been studied previously using non-selective reaction mechanisms. It is not possible to predict which states will be populated using the $(^3\text{He},d)$ reaction, so an internal calibration of the target using states in ^{27}Al cannot be performed. There are also insufficient narrow states known for any of the targets to perform a calibration using the $(^3\text{He},d)$ reaction. Instead other competing reactions must be used. The states populated in inelastic scattering measurements are too broad, which leaves the $(^3\text{He},p)$ reaction as the only source available for an accurate focal plane calibration. Unfortunately no states are presently known for the $^{26}\text{Mg}(^3\text{He},p)^{28}\text{Al}$ reaction, in the required energy

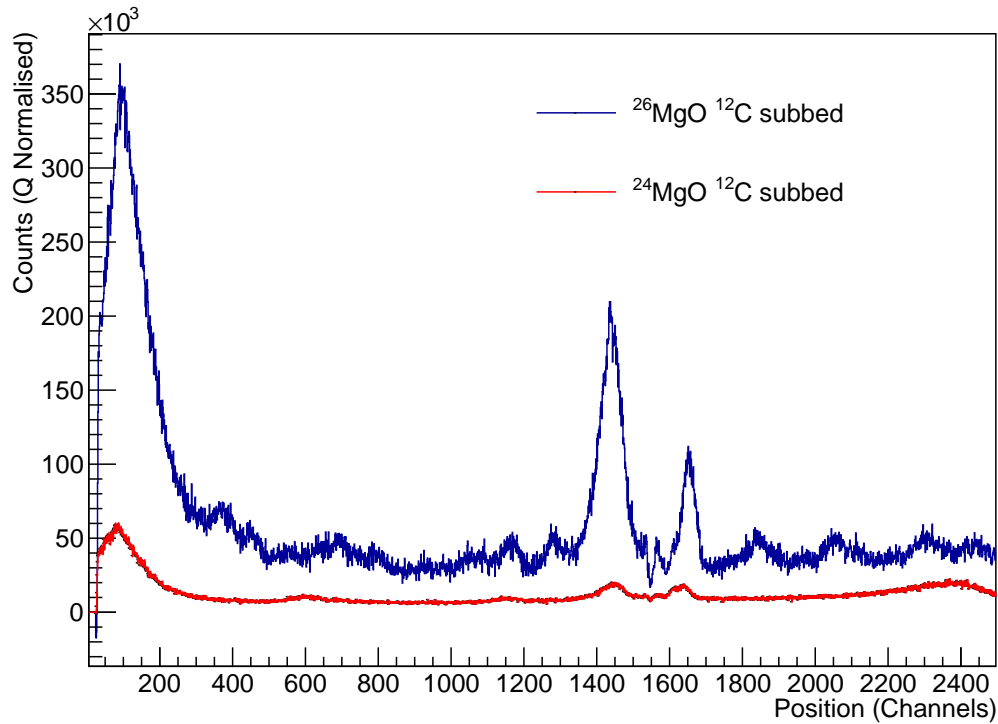


Figure 6.8: Overlay of charge normalised deuteron focal plane spectra for ^{26}MgO (blue) and ^{24}MgO (red) targets. The ^{24}MgO spectra have been scaled to match the ^{24}Mg content in the ^{26}MgO target.

region, so the calibration must be performed using transfer reactions on carbon [97] and oxygen [98]. The states used in the calibration are seen in Figure 6.10. Before obtaining a plot of magnetic rigidity versus focal plane position it is necessary to calculate energy losses through targets. For an internal calibration these can be ignored, however when calibrating using different targets and reactions these become important. Energy losses were calculated using the code SRIM [99] making the assumption that the reaction will occur in the centre of the targets. A plot of rigidity versus focal plane position is plot as described in section 4.3 and can be seen in Figure 6.11. The vertical errors are due to uncertainties in the excitation energies of the calibration states which are known to less than 1 keV. Separate plots are produced at each angle.

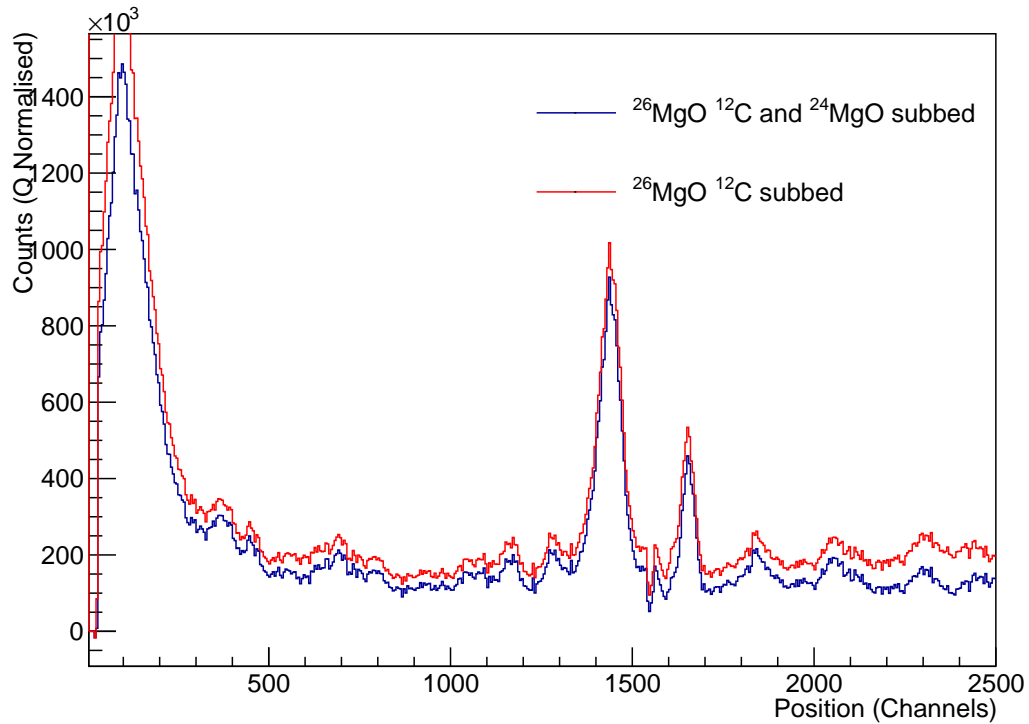


Figure 6.9: Deuteron focal plane spectra for ^{26}MgO target before (red) and after (blue) the subtraction of the scaled ^{24}MgO spectrum seen in Figure 6.8.

6.3 Focal Plane Fitting

In order to identify the states populated in the $^{26}\text{Mg}(^3\text{He},d)^{27}\text{Al}$ reaction and extract angular distributions a full focal plane spectrum fit will be performed. The fit functions and procedures used are the same as described in chapter 4. A few differences will arise, however due to the higher expected state density and the unknown level of oxygen background contaminant. The expected background from oxygen should be a first-order polynomial with a negative gradient. While it was not possible to determine the exact shape of the oxygen background from Figure 6.6, it appears to have a negative gradient. Leaving the background fit parameters to freely vary in the fit, however results in the fit minimising to positive gradient. The cause of the linear background is due to the population of broad high energy states [96], which would produce a background with a negative gradient. A positive background gradient would be both non-physical and contrary to what is seen with the SiO target data as shown in Figure 6.6. If the background is contained to a negative gradient, the fit no longer minimises or overestimates the level of the background.

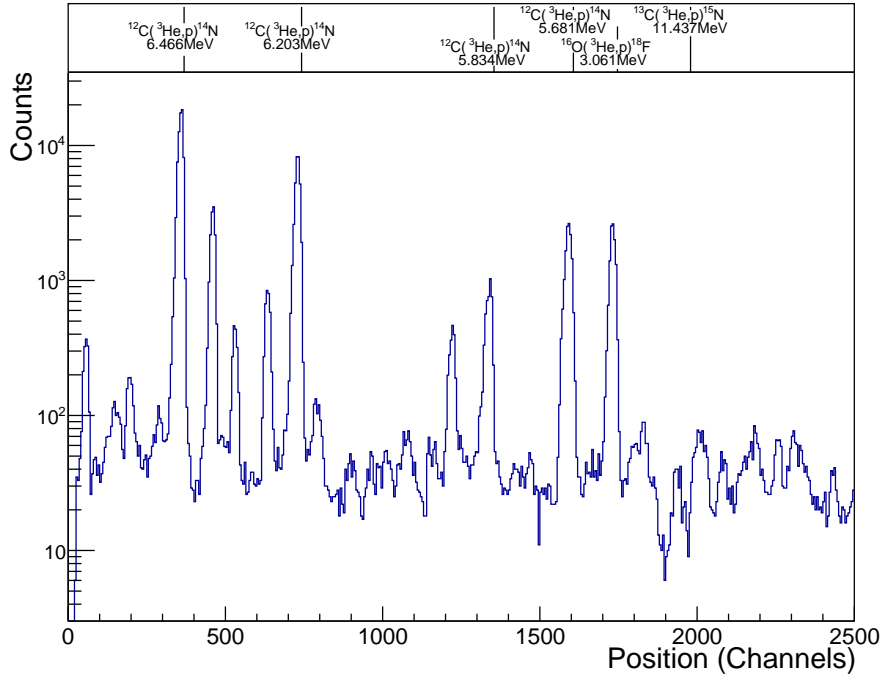


Figure 6.10: 5° focal plane spectrum for $(^3\text{He},p)$ reactions on a ^{26}MgO target. The top panel shows the states used for the calibration of the focal plane.

While it is difficult to understand the level of background contribution from oxygen, it is not actually necessary in order to accomplish the experimental aims. The states populated in this work are identified by fitting peaks and extracting their centroids which should be independent of the level of background. When extracting angular distributions from the fit, the level of background in the fit will affect the magnitude of the $d\sigma/d\Omega$ values, however the shape of the distribution should be unaffected. The differential cross section from the fit $d\sigma/d\Omega_{fit}$ is the sum of the peak and the background contributions:

$$\frac{d\sigma}{d\Omega_{fit}} = \frac{d\sigma}{d\Omega_{peak}} + \frac{d\sigma}{d\Omega_{back}}. \quad (6.1)$$

The differential cross section for the seemingly constant background contribution appears to be independent of the angle however, so provided similar proportions of background are used at all fit angles it should still be possible to extract ℓ transfer values. Without absolute values of the background it will not be possible to extract spectroscopic factors, C^2S , but these will not provide useful information for studying the $^{26}\text{Al}(n,p/\alpha)$ anyway. Any C^2S extracted in this work will be proton-transfer spectroscopic factor, however it is the neutron transfer spectroscopic

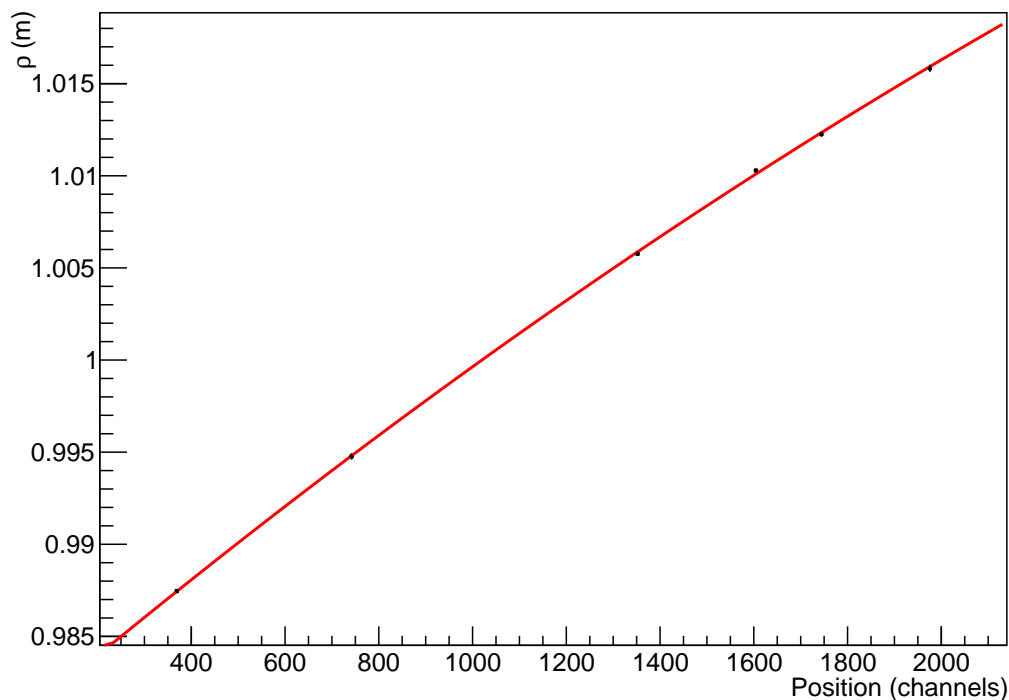


Figure 6.11: 5° $^{26}\text{Mg}(^3\text{He},\text{d})^{27}\text{Al}$ Focal Plane Calibration Curve. States known from previous $(^3\text{He},\text{p})$ reactions from target contaminants are identified along the focal plane and used to perform a calibration of focal plane position vs deuteron energy which can be related to excitation energy.

factors which would be of interest for the $^{26}\text{Al}(\text{n},\text{p}/\alpha)$ reactions. Only energy levels and spin-parities are therefore sought in this work.

For the focal plane fits it was decided to use a fixed constant background, with the focal plane spectrum fitted at multiple background levels. If the centroids of the peaks do not vary it is likely that they are real states. While the expected background should be linear, it was decided trying to fix the gradient to a non-zero value would introduce too much additional uncertainty. Specific descriptions of the fits at each angle will be discussed below.

6.3.1 Focal Plane Fits

6.3.1.1 Focal Plane fit 5°

The primary contaminants seen in 5° spectrum are due to reactions on ^{12}C and ^{16}O . Between channels 1420 – 1725 there are two broad peaks due to the 6.364 MeV ^{13}N state and 5.220 MeV ^{17}F state. As there does not appear to be any visible states from reactions on ^{26}Mg , this region is excluded from this fit. Exponential functions are used to account for both the broad 5.625 MeV state in ^{17}F observed at the edge of the focal plane as well the low-energy tail of the 6.364 MeV ^{13}N state. The fit is performed at three fixed background levels with the fit result and individual peak contributions shown in Figure 6.12. It is clear that while the height of the peaks vary depending upon the background the centroids remain consistent within their uncertainties. Using the calibration curve seen in Figure 6.11 the centroids are converted into excitation energy and are presented in Table 6.1.

6.3.1.2 Focal Plane fit 10°

The 10° focal plane spectrum is fitted in the same way as the 5° spectrum. The region 1280 - 1630 is excluded from the fit due to the presence of the 6.364 MeV ^{13}N state and 5.220 MeV ^{17}F contaminant states. As before exponential functions are used to fit the low-energy tail of the 6.364 MeV ^{13}N state and the high-energy tail of the broad 5.625 MeV ^{17}F state. Figure 6.13 shows the result of the focal plane fit at multiple fixed background levels along with the contributions from the individual peaks. The centroid position of the peaks can be seen to be consistent at different background levels and been converted into excitation energy and presented in Table 6.1.

6.3.1.3 Focal Plane fit 15°

Unlike the previous focal plane spectra the 15° spectrum fit is performed in two parts as it is now possible to identify ^{27}Al states between the 6.364 MeV ^{13}N state and 5.220 MeV ^{17}F contaminant states. The fit is performed using three fixed background levels for the following two regions:

Region 1 - The first fit region uses the same fitting conditions as described in

sections 6.3.1.1 and 6.3.1.2. The region between channels 1100 and 1625 are excluded from the fit and exponential functions are used to fit the high-energy tail of the 5.625 MeV ^{17}F state and low-energy tail of the 6.364 MeV ^{13}N state. While there now appears to be peaks visible between channels $\sim 1550 - 1625$ it was decided not to fit this region for several reasons. First is the drop in intensity which is seen in all focal plane spectra and is believed to be due to incomplete charge collection of the MWPC cathode strips. Second the region overlaps with a known state from reactions on ^{24}Mg . While the contribution from ^{24}Mg has been subtracted, see section 6.1.1.3, it is still possible a small amount may remain in the target. Given the high expected level density it could be easy to falsely identify a state as belonging to ^{27}Al . For this reason if there is uncertainty as to the origin of the peaks observed across the focal plane they are either excluded, or fit and not identified as a ^{27}Al state.

Region 2 - Between the 6.364 MeV ^{13}N state and 5.220 MeV ^{17}F contaminant states the spectra is fitted as a series of peak functions on a constant background with two exponentials fitting the high and low-energy tails of the main contaminant states. The width parameter, S in eq. (4.3), and the background are fixed from the fit of region 1.

The result of the focal plane fit can be seen in Figure 6.14, with the centroids converted into excitation energies and presented in Table 6.1.

6.3.1.4 Focal Plane fit 20°

The 20° focal plane fit is performed, like the 15° spectrum, in two parts:

Region 1 - The spectrum is fitted in the same as all other spectra, excluding the region outside the 6.364 MeV ^{13}N state and 5.220 MeV ^{17}F contaminant states covering channels 800 – 1625. As with the 15° fit the region between channels 1500 – 1625 is excluded due to uncertainties over the exact origins the peaks and the drop in intensity, believed to be from incomplete charge collection. It is possible that there are two peaks present between channels 1400 – 1500 which may belong to states in ^{27}Al , however it was decided not to include them in the focal plane fit. This is, because we require a state to be observed at three angles and there is no evidence of these peaks in the previous spectra, due to overlapping contaminant states.

Region 2 - This fit region spans channels 940 – 1330 and consists of 3 landau functions on a background consisting of two exponential functions and a constant background,

fixed from the previous fit.

Figure 6.15 shows the result of this focal plane fit with the individual peak contribution for multiple background levels. Excitation energies are extracted from the fit and presented in Table 6.1.

6.3.1.5 Focal Plane fit 25°

The final fit of the 25° focal plane spectra is again performed in two parts, inside and outside the 6.364 MeV ^{13}N state and 5.220 MeV ^{17}F contaminant state:

Region 1 - The first fit region has two exclusion regions between channels 520 – 1220 and 1375 – 1620. The first exclusion region is as before due to the contaminant states, however peaks between these contaminant states will be fitted in the second fit region. Channels 1375 – 1620 are excluded for the same reasons as the 20° fit: the drop in intensity due to incomplete charge collection, uncertainty in peak origin and possible ^{26}Mg states unobserved at other angles.

Region 2 - Between channels 620 – 1140 the spectra is fitted with multiple peak functions on a constant background with exponential functions used to fit the high and low-energy tails of the 6.364 MeV ^{13}N state and 5.220 MeV ^{17}F contaminant states.

The result of the fit at multiple background levels is seen in Figure 6.16 with the centroids of the individual states converted into an excitation energy and given in Table 6.1.

6.3.2 Observed ^{27}Al Energy Levels

After the focal plane fit has been performed the centroid of the individual peaks are converted into an excitation energy. In total 26 states belonging to ^{27}Al were observed across the focal plane at multiple angles. The energies at each angle are compared and used to calculate a mean energy which is presented in Table 6.1. In addition to the excitation energy the number of angles at which the state was observed is noted. Also shown in the table is the comparison with the previous work. It should be noted that the previous measurements [47] shown in Table 6.1 are not a complete list of the 43 states seen in this excitation region, but rather states where there may be agreement.

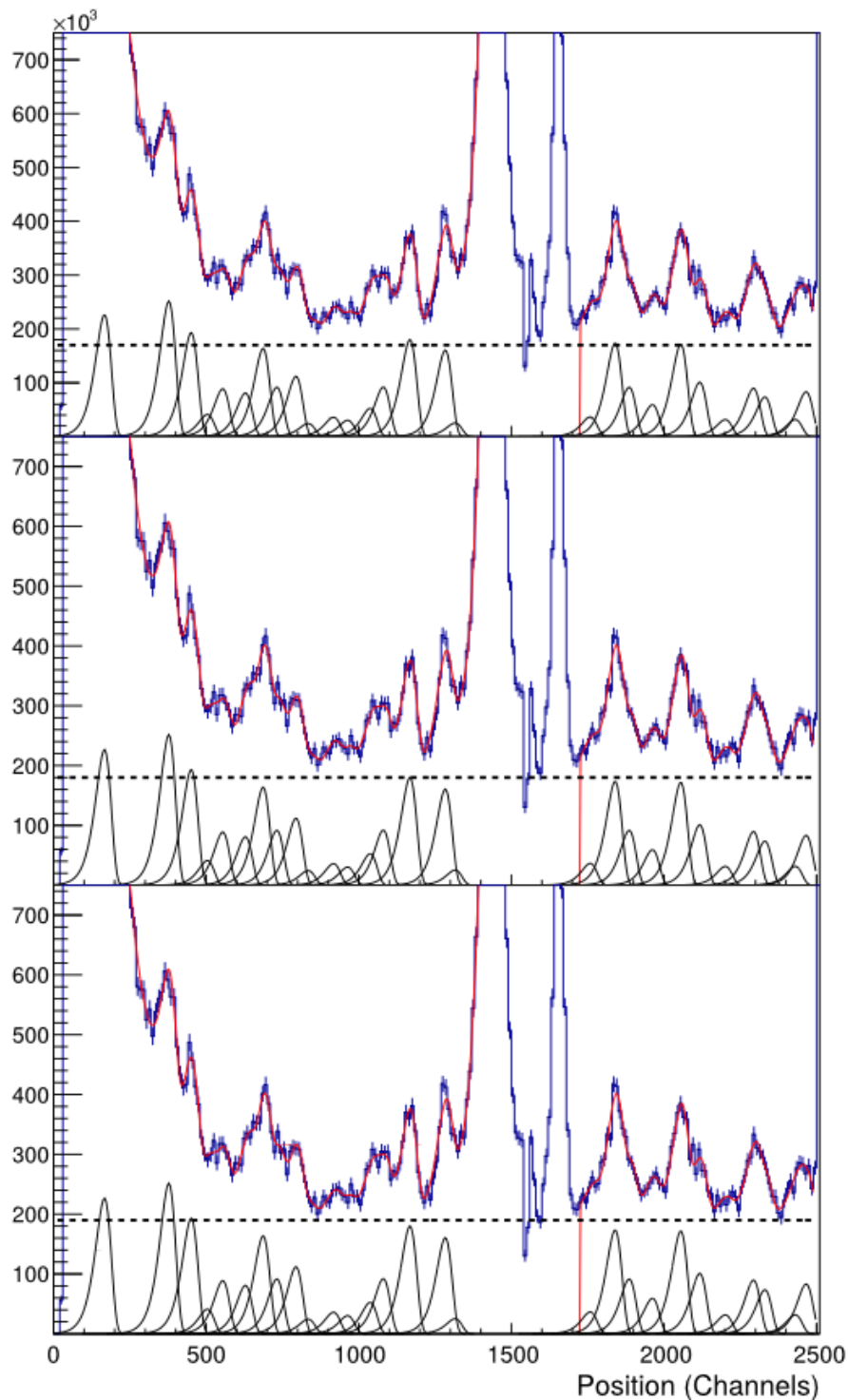


Figure 6.12: Fitted Focal plane spectra at 5° for the ^{26}MgO target. The spectrum has been fitted at three different background levels. The total fit is seen in red, with the background seen as a dashed black line and the individual peaks contribution shown in black. A detailed description of the fitting procedure is given in the text. The top axis shows the energy of the excited states in ^{27}Al from a linear calibration fit and should be taken as approximations only. A detailed description of the fit can be seen in the text.

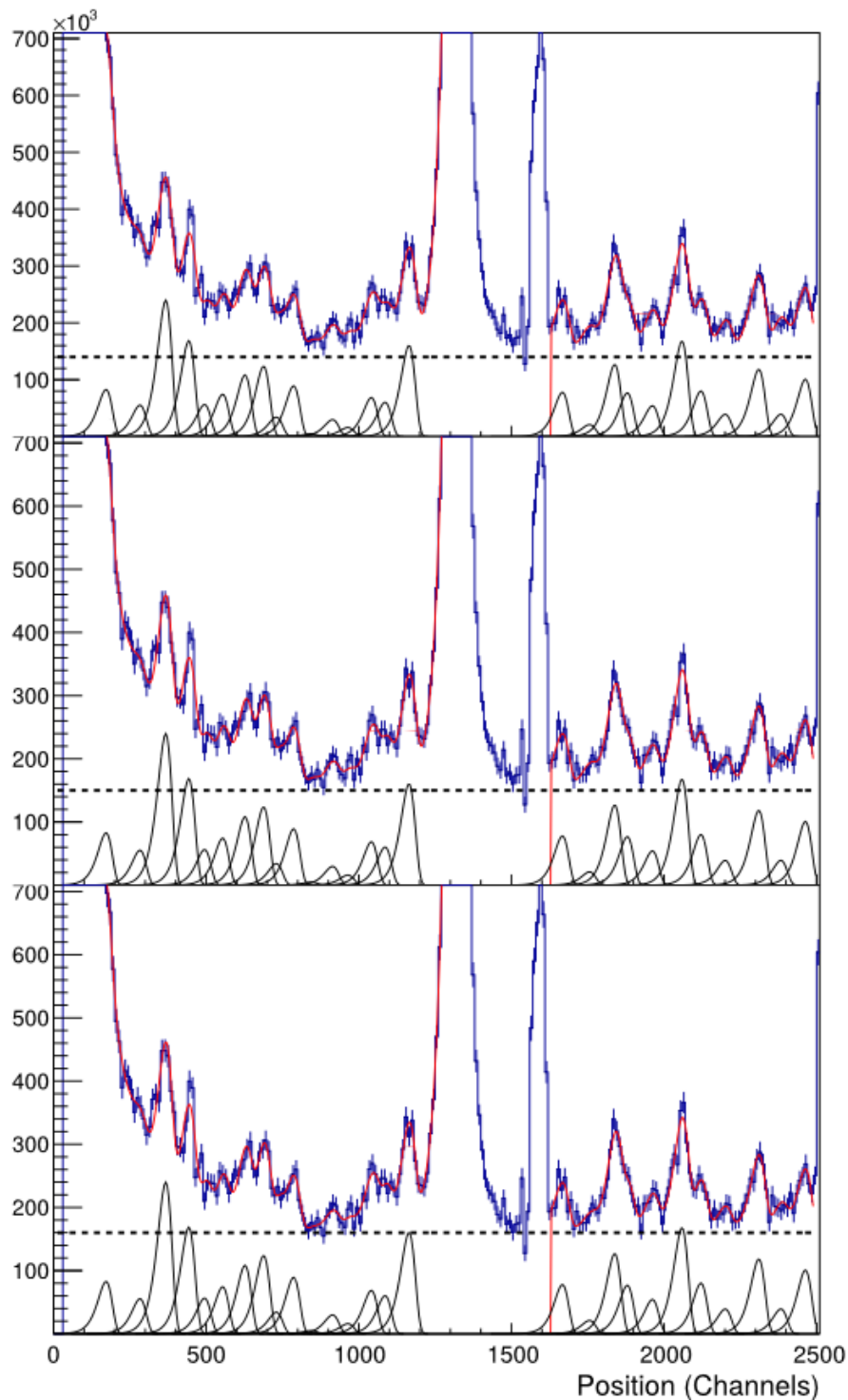


Figure 6.13: Fitted Focal plane spectra at 10° for the ^{26}MgO target. The spectrum has been fitted at three different background levels. The total fit is seen in red, with the background seen as a dashed black line and the individual peaks contribution shown in black. A detailed description of the fitting procedure is given in the text. The top axis shows the energy of the excited states in ^{27}Al from a linear calibration fit and should be taken as approximations only. A detailed description of the fit can be seen in the text.

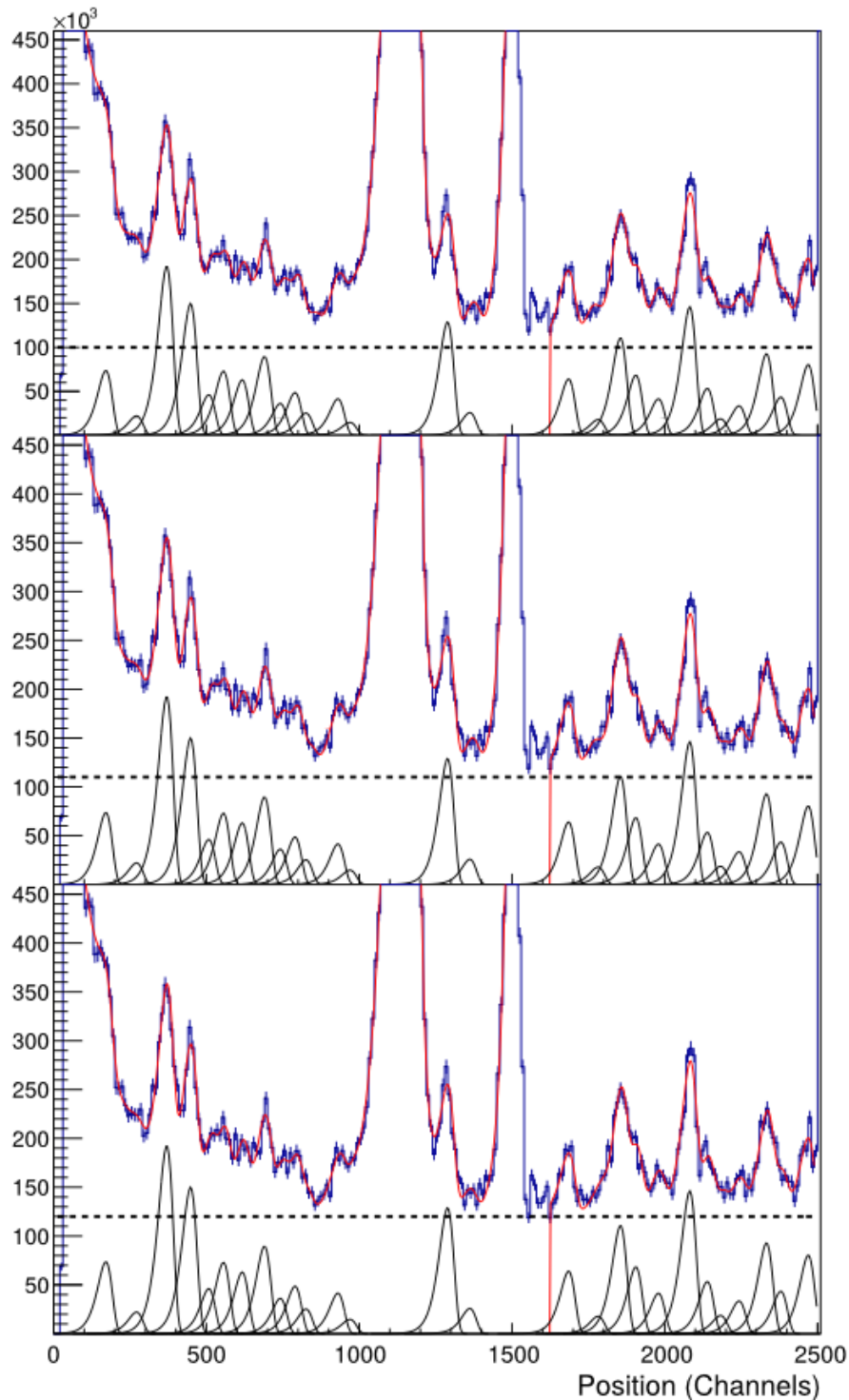


Figure 6.14: Fitted Focal plane spectra at 15° for the ^{26}MgO target. The spectrum has been fitted at three different background levels. The total fit is seen in red, with the background seen as a dashed black line and the individual peaks contribution shown in black. A detailed description of the fitting procedure is given in the text. The top axis shows the energy of the excited states in ^{27}Al from a linear calibration fit and should be taken as approximations only. A detailed description of the fit can be seen in the text.

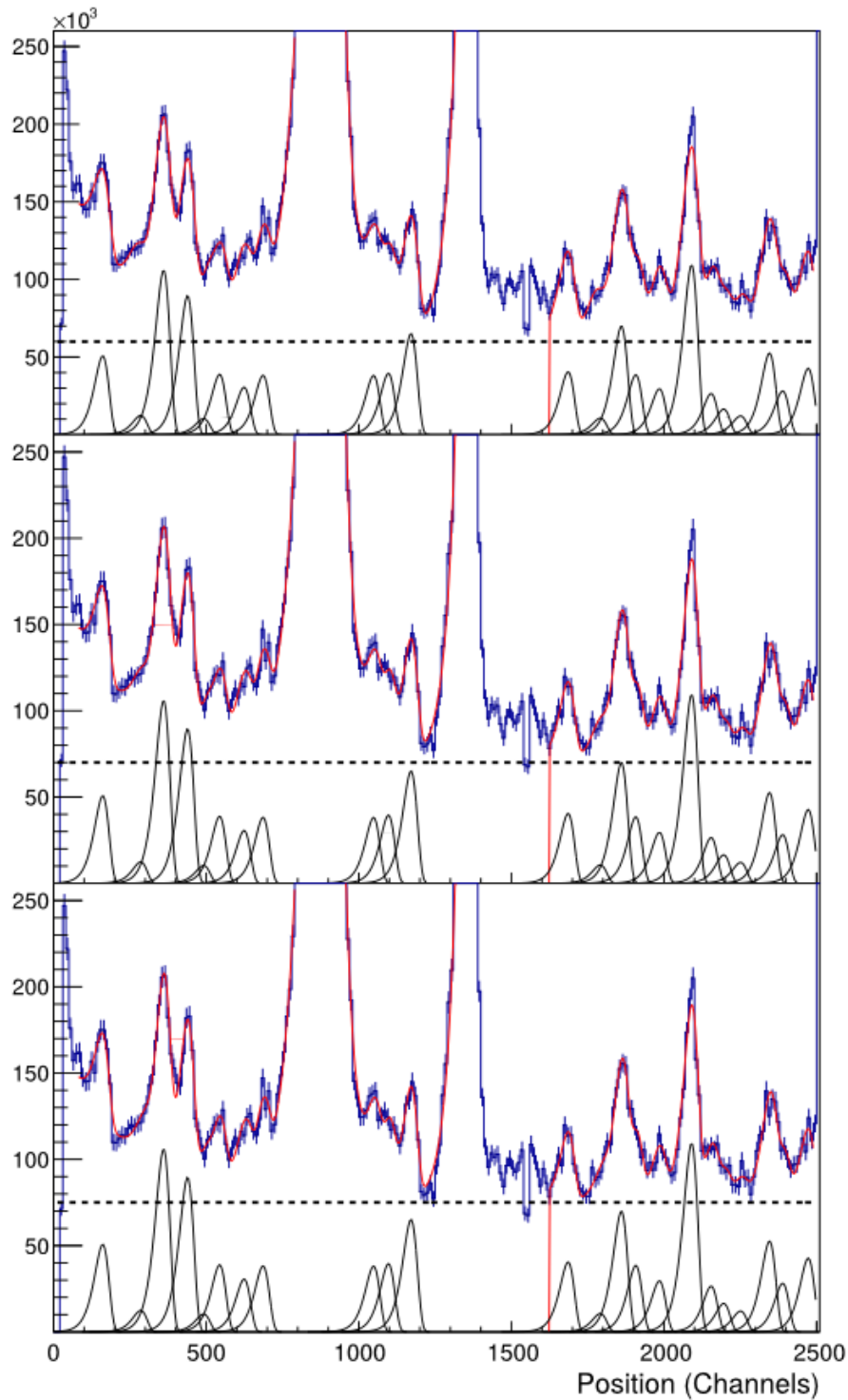


Figure 6.15: Fitted Focal plane spectra at 20° for the ^{26}MgO target. The spectrum has been fitted at three different background levels. The total fit is seen in red, with the background seen as a dashed black line and the individual peaks contribution shown in black. A detailed description of the fitting procedure is given in the text. The top axis shows the energy of the excited states in ^{27}Al from a linear calibration fit and should be taken as approximations only. A detailed description of the fit can be seen in the text.

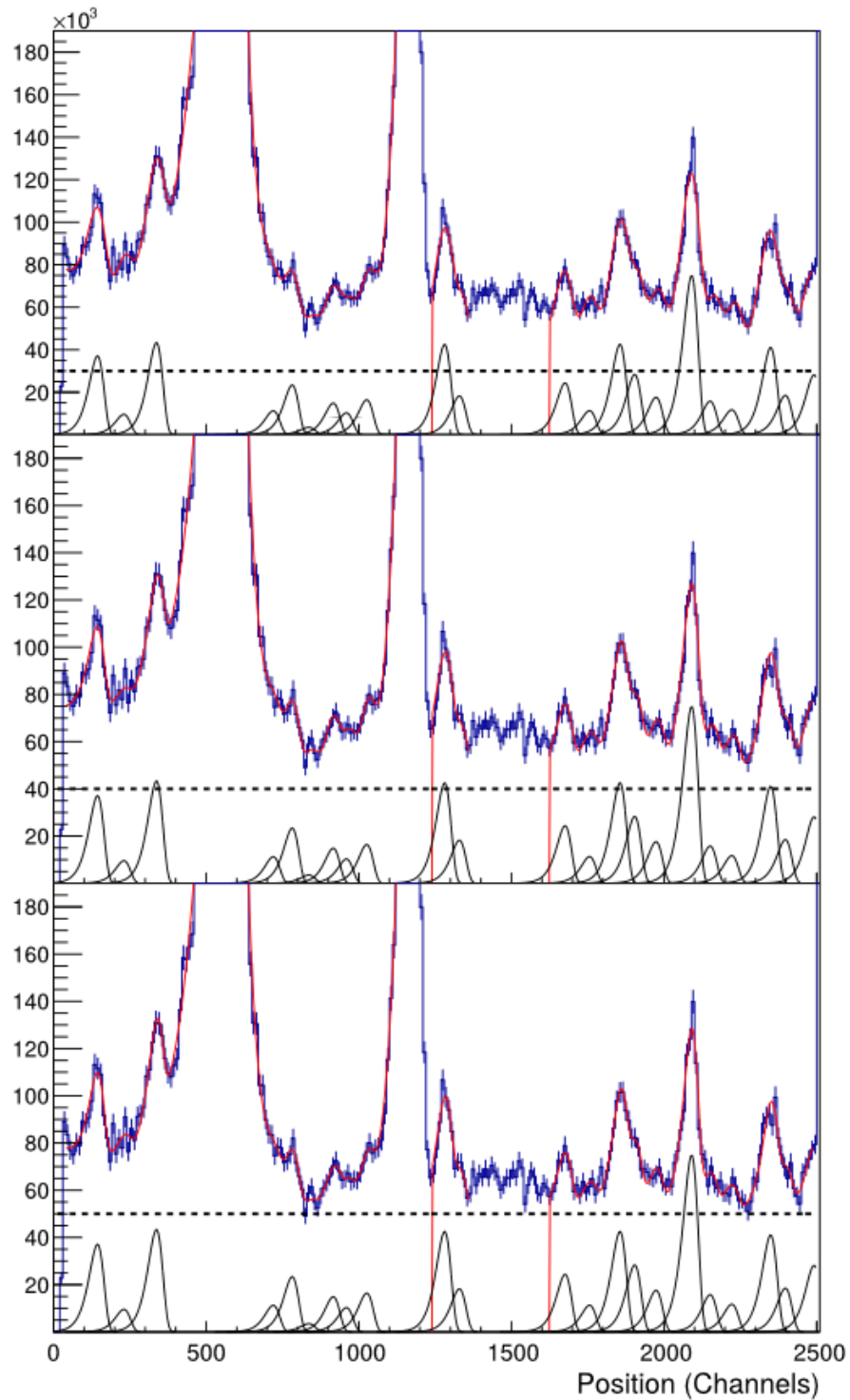


Figure 6.16: Fitted Focal plane spectra at 25° for the ^{26}MgO target. The spectrum has been fitted at three different background levels. The total fit is seen in red, with the background seen as a dashed black line and the individual peaks contribution shown in black. A detailed description of the fitting procedure is given in the text. The top axis shows the energy of the excited states in ^{27}Al from a linear calibration fit and should be taken as approximations only. A detailed description of the fit can be seen in the text.

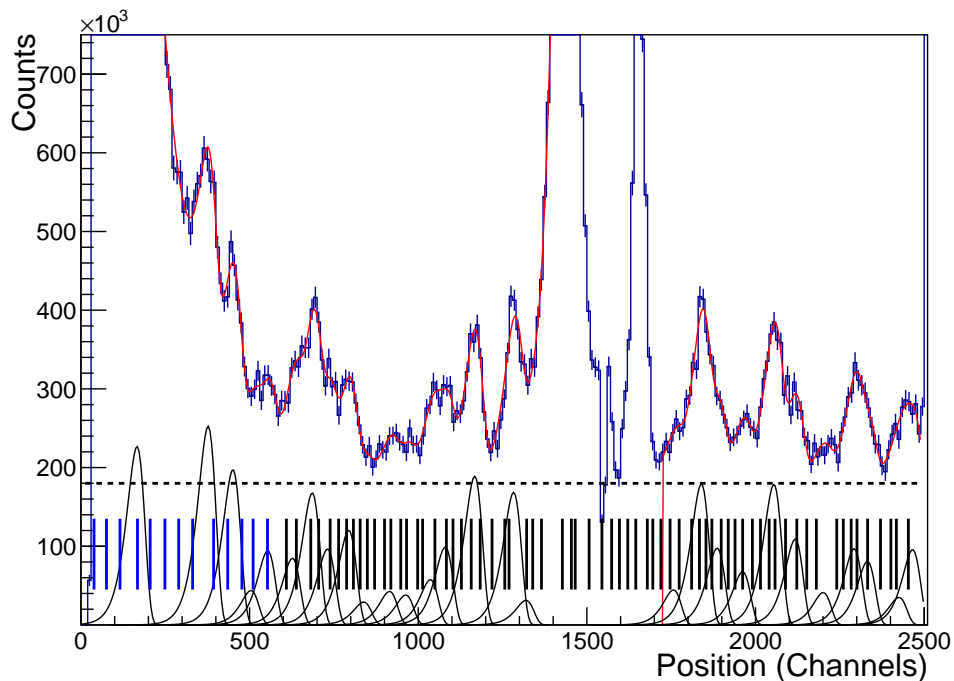


Figure 6.17: Fitted Focal plane spectra at 5° for the ^{26}MgO target. In addition to the total fit the individual peaks contributions can be seen in black with the background shown as dashed horizontal black line. The vertical lines show the predicted position of states observed in two previous (p,p') measurements, using the Munich Q3D (black) and the Orsay Split Pole (Blue).

In parallel to this work a new (p,p') measurement was performed at the MLL facility using the Q3D spectrometer [100]. This measurement was a repeat of the previous Orsay (p,p') measurement [47], but using the Q3D spectrometer to both confirm the previous results and to more accurately determine the excitation energies. The measurements of this work will be compared primarily with the newer Q3D data except above 13500 keV where only Split-Pole data is available.

At first it appears that the agreement between the previous and present work is poor. There is some agreement between the observed energy levels, however several states have either no obvious candidate to compare with or several. While it is possible that the discrepancies are the result of a poor calibration, it is more likely that the states cannot be resolved. To test this hypothesis the previous energy levels were converted to a focal plane position to predict where they would be observed if they were seen in this work. This is then overlaid with the result of the focal plane fit from this work with the result at 5° , seen in Figure 6.17. It is clear from this figure

that it is likely the peaks observed in this work are not single states but multiple unresolvable states which are known from (p,p') measurements [47, 100]. The (p,p') reaction populates all levels regardless of spins, opposed to the (³He,d) employed in this work which preferentially populates low spin states. This makes it difficult to identify which states are populated in this work and to perform a direct comparison of the present and previous data to identify individual energy states. Instead the conclusion that can be drawn is that the peaks extracted from the focal plane fits are potentially groups of states with at least one being a low spin state. Regardless of which states may have been populated in this work there is evidence that several of the previously observed energy states have no comparison, which itself may be an indication they are high spin states. The implication of this on the ²⁶Al(n,p/α) reaction rate will be discussed further in chapter 8.

6.4 Angular Distributions

As it does not appear to be possible to resolve individual energy states the information extracted from angular distributions will be limited. They can, however be used to show which state/s exhibit low spin behaviour which could be of use when designing later experiments. As with the ³⁵Cl data, angular distributions are drawn and fit with finite range DWBA calculations performed with the coupled-channel reaction code FRESKO [58]. The calculations are performed with the optical potentials of Liang *et al.* [83] and Daehnick *et al.* [85] for the ³He and deuteron channels respectively. As C²S values will not be extracted from this work calculations will be performed for J=ℓ+s coupling only.

6.4.1 Low Energy Angular distributions

While there is presently no data at ~ 13 MeV to compare angular distributions to, ²⁷Al has previously been studied at a lower excitation energy, ~ 7-8 MeV using a (³He,d) reaction [101]. This data was also recorded with a Q3D spectrometer which makes it ideal to compare with the present work. Data in the 7-8 MeV excitation region were recorded in the present work at two angles, 5 and 10° with the 10° spectrum seen in Figure 6.18. Also shown in the figure is the previous spectrum at 10° for comparison. It is clear that the agreement between the two spectra is very

Table 6.1: States observed in the $^{26}\text{Mg}(^3\text{He,d})^{27}\text{Al}$ reaction. Shown in the first column are the excitation energy of the states in keV with the second column showing the number of angles the state is observed at. In the final columns are the previously measured excitation energies from (p,p') measurements using the Orsay Split-Pole¹ [47] and the Munich Q3D² [100].

Present Work		Previous Work [47,100]		
E_x (keV)	Angles	E_x (keV)	(p,p')	
13647(4)	5	13643(4) ¹	13656(4) ¹	
13615(3)	4	13614(4) ¹		
13582(3)	5	13579(4) ¹		
13555(3)	4	13551(4) ¹		
13541(3)	4	13540(4) ¹		
13524(3)	4	13526(4) ¹		
13500(3)	4	13498 ²	13508 ²	13508(4) ¹
13476(3)	4	13477 ²	13478(4) ¹	
13446(3)	4	13444 ²	13450 ²	13449(4) ¹
13403(6)	4	13400 ²	13409 ²	
13395(3)	4	13395 ²	13397(4) ¹	
13365(3)	4	13369 ²	13365(5) ¹	
13356(3)	3	13353 ²	13359 ²	13354
13333(3)	3	13329 ²	13337 ²	
13297(3)	3	13304 ²	13306(4) ¹	
13186(3)	4	13184 ²	13188 ²	13184(5) ¹
13166(4)	5	13163 ²	13170 ²	13168(4) ¹
13142(3)	5	13142 ²	13147 ²	
13130(3)	5	13130 ²		
13111(3)	5	13106 ²	13114 ²	13106(4) ¹
13084(3)	5	13081 ²	13089 ²	13082(4) ¹
13069(3)	5	13066 ²	13073 ²	13063(4) ¹
13047(4)	5	13044 ²	13047(4) ¹	
13024(3)	5	13022 ²	13030 ²	
13010(3)	5	13006 ²	13013 ²	13016(4) ¹
12989(3)	5	12994 ²	12986(4) ¹	

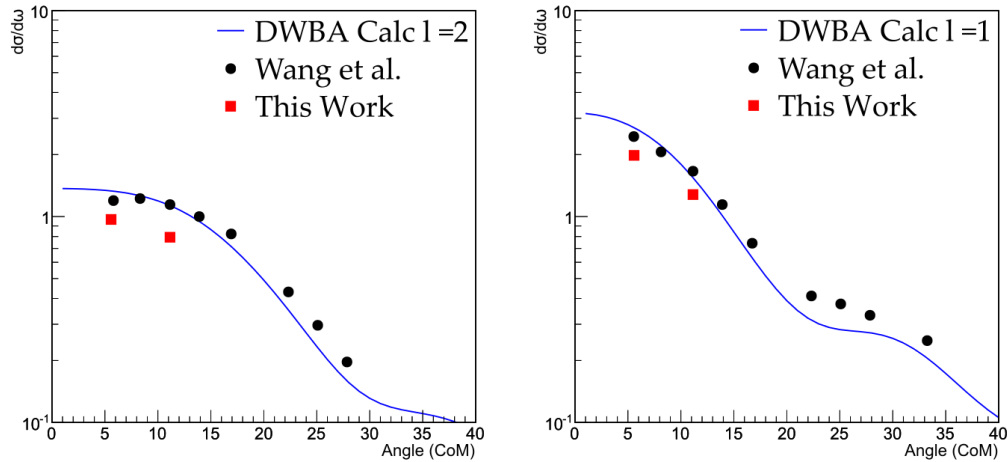


Figure 6.19: Angular distributions of Wang *et al.* [101], fitted with DWBA calculations performed here using FRESCO. Shown are the 8066 keV state (left) and the 8183 keV state (right). Differential cross sections have been extracted from the present work (red squares) and overlaid with the previous results (black dots). Statistical errors are drawn, but are smaller than the marker size.

6.4.2 ^{27}Al Angular distributions

Using eq. (4.7) the peak areas of the states seen in Table 6.1 are converted into differential cross sections and plot as angular distributions. These are then fitted with DWBA calculations performed with FRESCO with the results shown in Figure 6.20 for $J=\ell+s$ coupling. The best fits for each state are summarised in Table 6.2 which shows the adopted excitation energy and angular momentum transfer ℓ . It should be noted that for some states it is not possible to make definite ℓ assignments and multiple angular transfer values are allowed.

While it is not possible to make definite spin assignments for a large number of states it is clear that they exhibit low spin behaviour. Within the present experimental uncertainties, many of the states seem to agree with an $\ell=2$ or $\ell=3$ transfer. This could be an indication that the distributions which have been fitted are in fact the sum of several states, rather than an individual state. This will be discussed further in chapter 8.

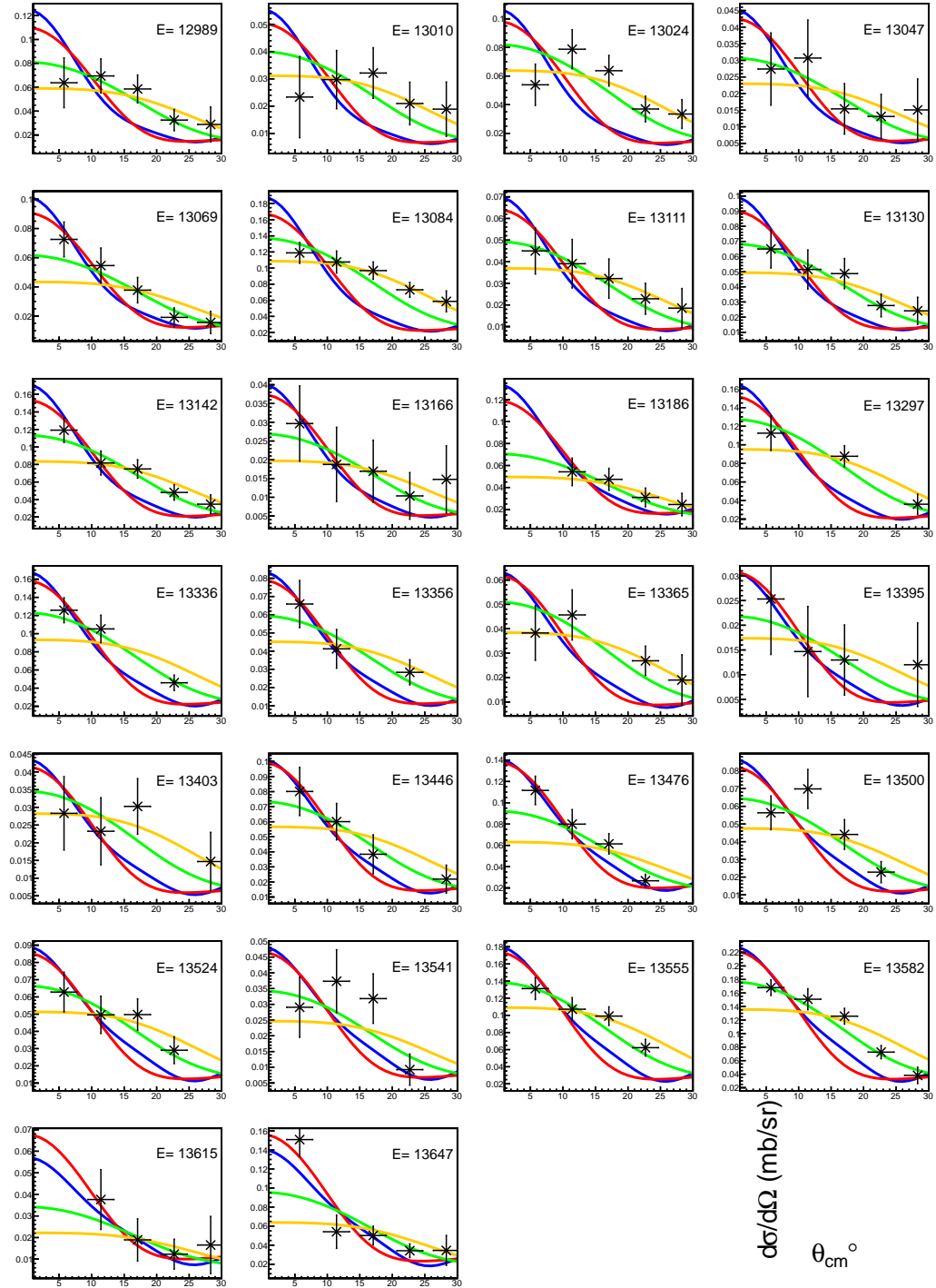


Figure 6.20: Deuteron angular distributions measured with the $^{26}\text{Mg}(^3\text{He},d)^{27}\text{Al}$ reaction at 20 MeV for $J=\ell+s$ coupling. Graphs are fitted with calculated DWBA angular distributions for angular momentum transfer $\ell=0$ (Blue), $\ell=1$ (Red), $\ell=2$ (Green), $\ell=3$ (Yellow). Extracted angular momentum transfer and spectroscopic factors from the fits are summarised in Table 6.2.

Table 6.2: Nuclear structure of ^{27}Al for states within $13 < E_x < 13.7$ MeV. The first two columns give weighted averages of E_x from the present work and the adopted orbital angular momentum transfer values ℓ , as determined in the present work. If the distributions agree with multiple ℓ transfers all values are given.

E_x (keV)	ℓ transferred	E_x (keV)	ℓ transferred
13647(4)	1	13333(3)	2
13615(3)	0-3	13297(3)	2,3
13582(3)	2,3	13186(3)	2,3
13555(3)	2,3	13166(4)	0-3
13541(3)	2	13142(3)	2
13524(3)	2,3	13130(3)	2,3
13500(3)	-	13111(3)	2,3
13476(3)	0,1	13084(3)	2,3
13446(3)	0-2	13069(3)	0-2
13403(6)	2,3	13047(4)	0-3
13395(3)	0-3	13024(3)	2,3
13365(3)	2,3	13010(3)	2,3
13356(3)	2	12989(3)	2,3

Chapter 7

$^{26}\text{Mg}(\alpha,t)^{27}\text{Al}$ Analysis and Results

The spectroscopic study of ^{27}Al was performed using two transfer reactions, ($^3\text{He,d}$) and (α,t), the former of which was been detailed in chapter 6. This chapter will present the results of the $^{26}\text{Mg}(\alpha,t)^{27}\text{Al}$ reaction performed at the MLL facility in Garching using the Q3D magnetic spectrometer. The implications of the results with regards to the experimental outcomes are discussed in chapter 8. The $^{26}\text{Mg}(\alpha,t)^{27}\text{Al}$ reaction was performed using a 35 MeV ^4He beam, which was accelerated and impinged on the targets listed in Table 3.2, primarily an enriched $50\ \mu\text{g}/\text{cm}^2$ ^{26}MgO target on $8\ \mu\text{g}/\text{cm}^2$ carbon backing, with the scattered particles analysed at the focal plane of a Q3D magnetic spectrometer. Due to low cross sections and limited beam-time reaction products were measured at only 3 angles, 5.5, 10 and 15 degrees. As a consequence of the beam time availability it was not possible to perform runs of each target at all measurement angles. The aim of this study was to be identify high spins states which will be used with other experimental data, which aimed to measure particle widths, to improve reaction rates for the $^{26}\text{Al}(n,p/\alpha)$ reactions, however due to various factors discussed below this aim was not achieved.

7.1 Focal Plane Identification

Using the δE versus δE and δE versus E methods and the MWPCs it is possible to identify tritons across the focal plane. Placing a gate on the triton locus, seen

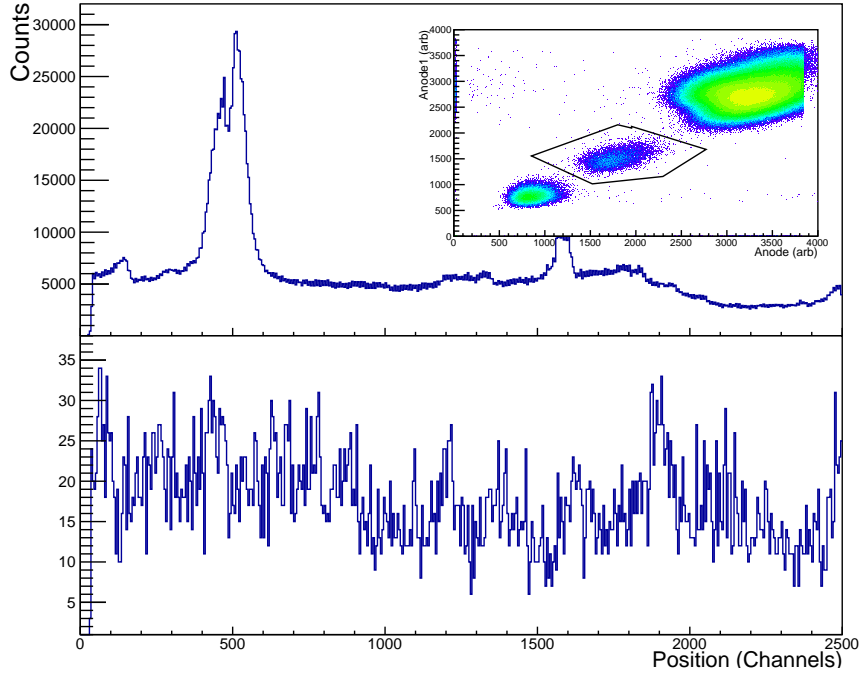


Figure 7.1: Focal plane spectrum for the $50 \mu\text{g}/\text{cm}^2$ ^{26}MgO target at 10° . Top: Ungated focal plane spectrum showing all reaction products. Inset: MWPC1 Anode charge versus MWPC2 Anode charge, a gate is placed around the triton locus. The other loci belong to alpha particles (top right) and deuterons (bottom left). Bottom: Triton gated focal plane spectrum for the $50 \mu\text{g}/\text{cm}^2$ ^{26}MgO at 10° . Peaks seen in this spectrum are due to (α,t) reactions on the experimental target.

in the inset of Figure 7.1, allows for the identification of (α,t) reaction channels with the resulting spectrum at 10° for a single run file of the $50 \mu\text{g}/\text{cm}^2$ ^{26}MgO target seen in the bottom panel of Figure 7.1. Other reaction channels which can be seen at the focal plane are inelastic (α,α') scattering and (α,d) transfer reactions. Comparing the ungated and triton-gated focal plane spectra in Figure 7.1 it is clear that the (α,t) cross section is very weak in comparison to the total reaction cross section. While the spectrum in Figure 7.1 is only a single run file it contains $\sim 1/4$ of the total accumulated data at 10° . Given the low level of statistics seen in the spectra the identification of individual states and ultimately the extraction of differential cross sections to fit with DWBA calculations will be difficult. The total accumulated experimental data at all measurement angles can be seen in Figure 7.2.

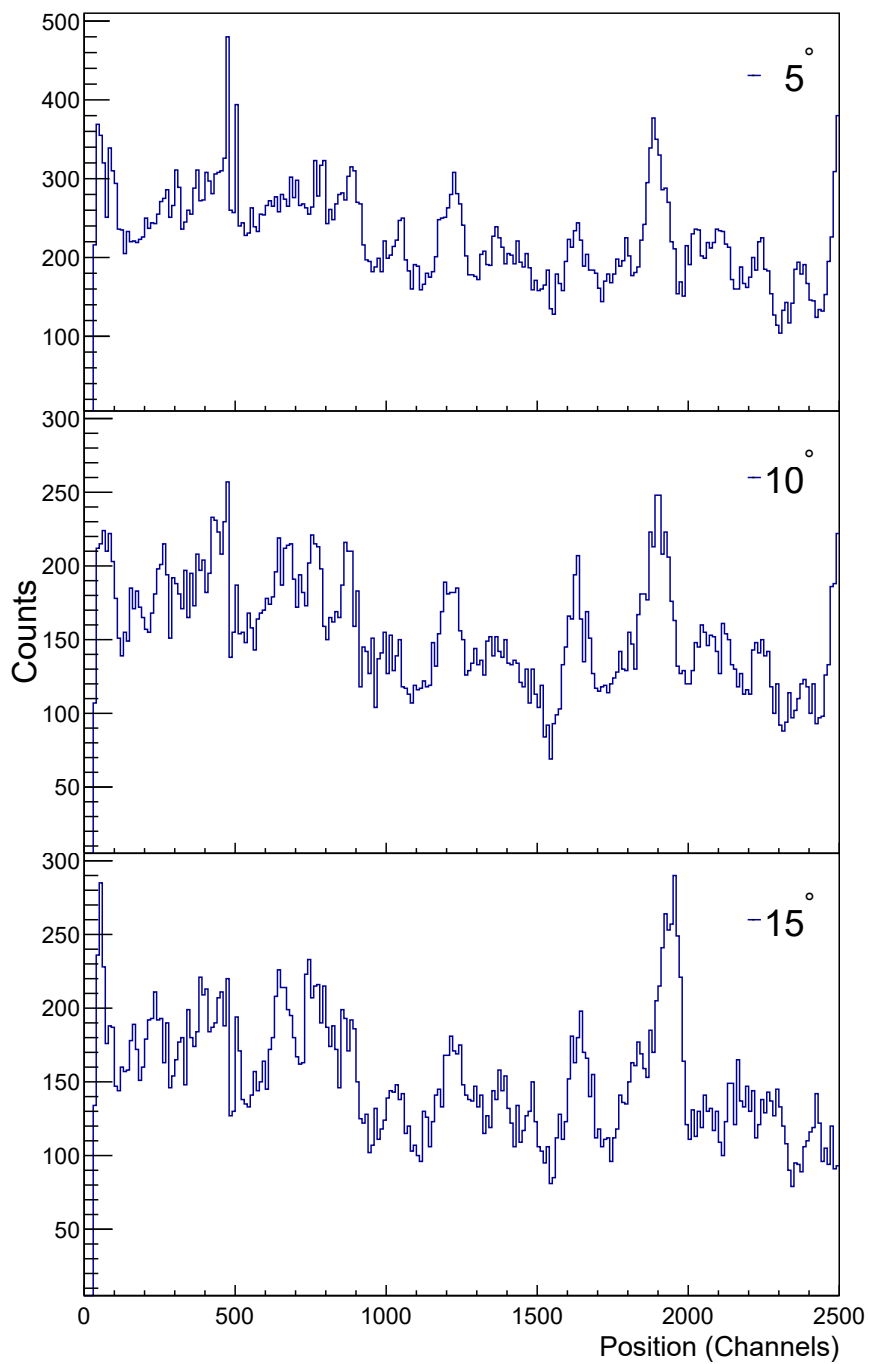


Figure 7.2: Total accumulated $^{26}\text{Mg}(\alpha, t)^{27}\text{Al}$ data using a $50 \mu\text{g}/\text{cm}^2$ ^{26}MgO target. Shown are spectra containing all of the data at the measurement angles, 5.5° (top panel), 10° (middle panel) and 15° (bottom panel).

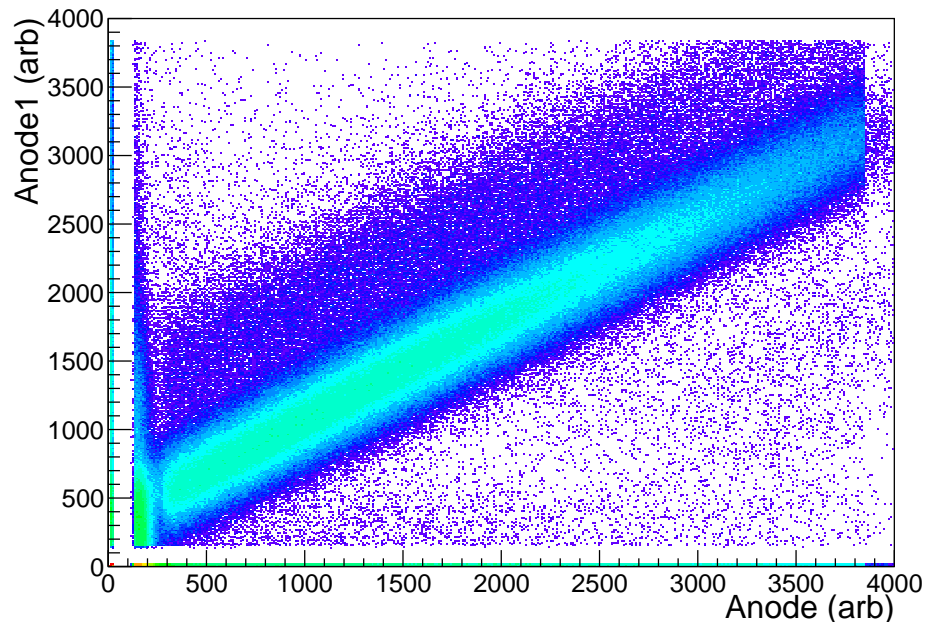


Figure 7.3: MWPC1 Anode charge versus MWPC2 Anode charge for the ^{nat}C target. It can be seen that the particle loci, seen in the inset of Figure 7.1, are no longer visible. This suggests the target has been broken with reaction products observed at the focal plane being a result of multiple scattering.

7.1.1 Background Contaminants

Due to the low statistics identifying individual states is very difficult. While it is possible all the data seen in Figure 7.2 is from states in ^{27}Al , it is more likely contamination is present in the form of individual contaminant states and linear background from the population of broad high-energy states in the contaminant nuclei [96]. From the analysis of the $(^3\text{He},d)$ data in Chapter 6, the primary contaminants are expected to be ^{12}C , ^{16}O and ^{24}Mg .

Unfortunately it was not possible to identify states in ^{13}N from $^{12}\text{C}(\alpha,t)$ reactions or to determine the contribution of carbon to the spectrum background. While a ^{nat}C target was placed in position 6 of the target ladder, Table 3.2, it was found to have been damaged once removed from the target chamber. This breakage can be seen in the data by observing the δE versus δE particle ID spectra for the carbon target in Figure 7.3. Unlike the particle ID spectra seen in the inset of Figure 7.1, there is no distinct particle loci which suggests the particles seen in the focal plane were the result of random scattering off a damaged target.

Similarly to the ($^3\text{He},d$) data it is not possible to identify the background contribution due to oxygen present within the target. Measurements using an SiO target could potential be used to determine the oxygen background, however data were recorded only at 15° and with a limited run time and only 4 events were collected from this measurement and it is not possible to identify either states or a background. This could be an indication that contributions from oxygen are not significant and do not need to be accounted for. With a limited run time, however it is not sensible to draw this conclusion, as low cross sections are seen for measurements with all targets. With the ^{26}MgO target measurements performed over a period of hours, the possibility of a large oxygen contribution to the resulting focal plane spectrum cannot be excluded based on a single, (10 min), measurement.

Finally, there was no data recorded for a ^{nat}MgO target so it is not possible to identify states from reactions on ^{24}Mg . While the targets are known to be enriched to approximately 95% ^{26}Mg content, it was seen in section 6.1.1.3 that the 5% of ^{24}Mg still present within the target is significant. Reactions on ^{24}Mg would populate states in ^{25}Al at an excitation energy of 6.5 – 7.5 MeV. With over 15 states presently known in this energy region, [102], it is possible that ^{25}Al states could be falsely identified as belonging to ^{27}Al .

Given the lack of contaminant information it is not possible to identify either the proportion or shape of the background due to contaminants. While the contaminant background in the ($^3\text{He},d$) spectra was also unknown it was at least possible to quantify several of the contaminants and account for the unknown contributions by fitting the spectra at multiple background levels. For the spectra in Figure 7.2 however, it appears that the states are on top of a large linear background and assumptions used in section 6.3 are invalid. While it may be possible to fit the spectra and extract centroid position to determine excitation energies, it will not be possible to use the data to draw and fit angular distributions in order to extract ℓ values.

7.2 Focal Plane Calibration

With the high level density known to exist in ^{27}Al , [47, 100], it will not be possible to perform an internal calibration of the ^{26}MgO target. While a SiO and a ZnS

target were employed for calibration purposes they were measured at 15° only and the run times were too short to accumulate enough statistics. As a result of the low cross sections seen in the (α, t) data other reaction channels must be used to perform a calibration. The remaining reaction channels, however each have their own problems.

Placing a gate on the α particle locus in Figure 7.1 produces the spectrum seen in bottom panel of Figure 7.4. It is clear from this spectrum that the (α, α') reaction populates several broad states. The top panel of Figure 7.4 shows the expected position of states which could be populated from reactions on the ^{26}MgO target. Based on the expected target composition, reactions would be expected from ^{26}Mg , ^{24}Mg and ^{16}O with additional reactions from the nuclei ^{12}C and ^{13}C from the targets' carbon backing. The positions are calculated using the nukesim code [74] for an Enge-Split pole spectrometer [48] and as a result should not be taken as exact positions as this data was recorded with a Q3D spectrometer which has different ion optics. Given the non-selectivity of the inelastic scattering mechanism all known states would be expected to be populated so it is difficult to assign individual states as many would be expected to overlap. As shown in the top panel of Figure 7.4 there are multiple cases where observed states would overlap, for example at channel 500 a doublet is seen which could be states in ^{26}Mg , ^{12}C or ^{16}O . Access to additional data for reactions on a ^{nat}MgO or ^{nat}C target would be useful for this purpose, however as no data was recorded for the former and the second was damaged it is not possible to identify these states. In addition it is also difficult to accurately extract centroid position from the broad states seen in the spectrum. Without accurate centroid positions it is not possible to perform a calibration which can be used to identify states in a region with the high level density known to exist in ^{27}Al . As shown in the bottom panel of Figure 7.5, the (α, d) reaction channel does appear promising for calibration purpose with several narrow peaks seen across the focal plane. It is very difficult, however to identify what these peaks are. It can be seen in the top panel of Figure 7.5 that there are no known states in the 10.3 - 11.3 MeV region in ^{28}Al which would be populated in the $^{26}\text{Mg}(\alpha, d)^{28}\text{Al}$ reaction. There appears to be no agreement between the experimental peaks and states which would be populated in are to many states in (α, d) reactions on ^{12}C , ^{13}C and ^{16}O nuclei. While there is some agreement between the positions of the focal plane peaks and the expected position of states in ^{26}Al , many would be expected to overlap which would make the extraction of centroids difficult. It is likely that several of the isolated peaks

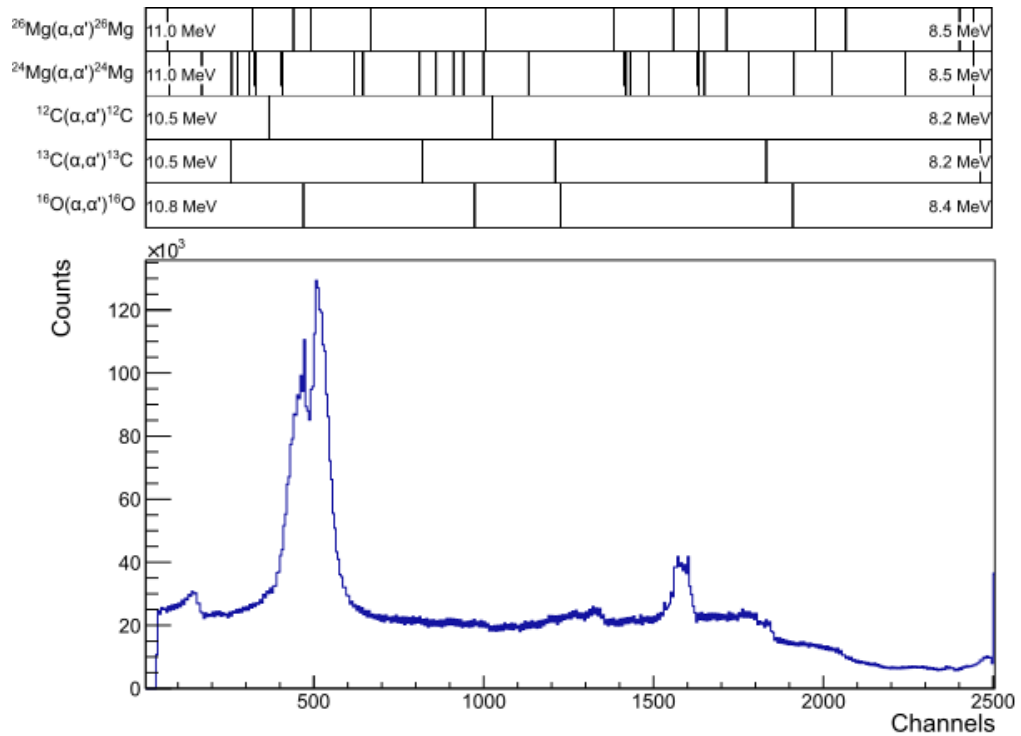


Figure 7.4: Comparison of observed and known states from (α, α') reactions on a ^{26}MgO target. Bottom - 10° focal plane spectrum for (α, α') reactions on a $50 \mu\text{g}/\text{cm}^2$ ^{26}MgO target. Top - The predicted position of states from reactions on ^{26}Mg , ^{24}Mg , ^{12}C , ^{13}C and ^{16}O . For clarity the energies of the states are not shown, however the energy region which would be seen across the focal plane is marked. The positions are calculated from the nukesim code [74] for an Enge-Split pole spectrometer [48] and should be used as estimated rather than exact positions.

Chapter 8

Discussion of $^{26}\text{Mg}(^3\text{He,d})^{27}\text{Al}$ and $^{26}\text{Mg}(\alpha,\text{t})^{27}\text{Al}$ results

The $^{26}\text{Al}(\text{n,p}/\alpha)$ reaction rates were studied using the $^{26}\text{Mg}(^3\text{He,d})^{27}\text{Al}$ and $^{26}\text{Mg}(\alpha,\text{t})^{27}\text{Al}$ at the MLL facility using the Q3D magnetic spectrometer. Previous (p,p') measurements [47,100] have identified the states in ^{27}Al in the astrophysically relevant energy region and the aim of the measurements in this thesis was to identify which of these states are populated using more selective reaction mechanisms. The spin of states in ^{27}Al were to be deduced using a comparison of ($^3\text{He,d}$) and (α,t) transfer reactions which populate low and high spin states respectively. In addition, each reaction was studied at multiple angles with the aim of extracting angular distributions and using these in conjunction with DWBA calculations to assign spin to previously known states.

As discussed in chapters 6 and 7 however, it was not possible to accomplish the experimental aims. The resolution of the spectrometer was not sufficient for the ($^3\text{He,d}$) reaction to resolve individual states and the energies and angular distributions extracted likely describe groups of states. Regardless it is possible to conclude that many of the states in the relevant energy region of ^{27}Al are in fact low spin states and may not be relevant to the overall $^{26}\text{Al}(\text{n,p}/\alpha)$ reaction rates. This will be discussed in more detail in section 8.1. For the (α,t) reaction, however a variety of issues prevented any useful information from being extracted. Despite these issues, it is still believed that a study of states in ^{27}Al using the (α,t) reaction could provide nuclear information relevant for the $^{26}\text{Al}(\text{n,p}/\alpha)$ reaction rates. Knowing the problems encountered during this measurement it will be

possible to correct these issues for a repeat study with the details given below.

8.1 Discussion of $^{26}\text{Mg}(^3\text{He,d})^{27}\text{Al}$ Results

The main results of this work are summarised in Tables 6.1 and 6.2. In total 26 states, or groups of states, were populated in the ($^3\text{He,d}$) reaction and from angular distributions it can be seen that they appear to show low spin behaviour matching DWBA calculations for spin transfers of $\ell = 0 - 3$. This measurement populated states in the energy region of $\sim 13 - 13.6$ MeV for which there are presently 78 levels known from the two previous (p,p') studies [47, 100] performed using the Orsay Split-Pole and Q3D magnetic spectrometers. The energies of the Q3D are more accurate and are used for comparison. however 10 states above 13.5 MeV are known only from the Orsay Split-Pole measurement.

A comparison of this work and the (p,p') measurement performed at the Q3D shows that there are 23 previously known states for which there is no obvious comparison with this work. Similarly, comparing with the known levels above 13.5 MeV from the Split-Pole there are three known states for which there is no clear candidate in the present work. These levels are given in Table 8.1. It should be noted due to persistent carbon and oxygen contamination between channels 1300 - 1600 of the focal plane there is no information from this work for states between 13190 - 13290 keV excitation energy. There are 12 states known in this region, however it is not possible to comment on the spin of these states. Given the selectivity of the ($^3\text{He,d}$) reaction it can be argued that the levels given in Table 6.1 are low spin states, with the argument further strengthened by the angular distributions. This would make the levels in Table 8.1 high spin states, however further measurements would be required to conclude this.

With regards to the effect of these levels to the $^{26}\text{Al}(n,p/\alpha)$ reaction rates, the presence of a centrifugal barrier inhibits astrophysical reaction rates, therefore nuclear reactions will typically proceed through states where there is a smaller ℓ transfer. The high ground state spin of ^{26}Al , 5^+ , however would require high-spin states in ^{27}Al to be populated in the reaction for a low- ℓ neutron transfer. It is likely then that the states found to be populated in the ($^3\text{He,d}$) reaction are not important to the neutron destruction rate of ^{26}Al . This result is not unexpected and in fact proves that while many states do exist above the neutron threshold, $\sim 2/3 - 3/4$ of

Table 8.1: Known states in ^{27}Al not observed in this work. Shown in this table is the energies of states populated in (p,p') measurements [47,100] which have no analogue with this work. This may be an indication that they are high spin states.

E_x (keV)	E_x (keV)
13628	13319
13600	13307
13565	13177
13484	13153
13466	13137
13458	13125
13438	13119
13431	13100
13424	13094
13415	13059
13385	13039
13380	13034
13346	13002

all the known states appear to show low spin behaviour and as a result will have little effect on the reaction rate. The previous reaction rate was calculated with a statistical model [43], which requires a high level density. If many of the states are low spin, which this work appears to show, the assumptions of the statistical model may be invalid.

The primary source of uncertainty when assigning spin is due to the unknown oxygen contaminant background in the fits and repeat measurements would require some way to quantify this to improve results. Despite this it is unlikely that a further ($^3\text{He},d$) study could be used to improve the reaction rate. Ultimately, the level density is too high and without improved energy resolution it will not be possible to resolve individual states. While this work will not directly improve the reaction rate, it highlights the need for further experimentation and hints at several states that may be important and should be studied further.

8.2 Discussion of $^{26}\text{Mg}(\alpha,t)^{27}\text{Al}$ Results

As was already discussed in chapter 7 has already discussed the difficulties studying this reaction and the inability to accomplish the experimental aims. Primarily the biggest issue with this study was the availability of beam time which was given to study both reactions. The (α,t) measurement was performed prior to the ($^3\text{He},d$) measurement and given the lower than expected cross sections it was decided to focus the remaining beam time on the ($^3\text{He},d$) reaction. As a result of this there was not enough time to measure the (α,t) reaction at more angles or perform measurements on the other experimental targets.

While many issues arose during this experiment, the study of the $^{26}\text{Al}(n,p/\alpha)$ reaction rates could benefit from a repeat of this measurement. The peaks seen in the (α,t) spectra in Figure 7.2 appear to be more isolated than in the ($^3\text{He},d$) spectra which may be an indication that fewer states are populated in the reaction. If the peaks are from states in ^{27}Al it may be possible to resolve and identify individual states. Due to momentum matching the (α,t) transfer reaction should populate high spin states, therefore these peaks may be important to the study of the $^{26}\text{Al}(n,p/\alpha)$ reaction rates.

If the (α,t) measurement were repeated it would need all available beam time in order to obtain sufficient statistics to extract the necessary nuclear information. The results

of this work have shown that given the low reaction cross sections, more time is needed to both measure the reaction at multiple angles and to perform measurements on other experimental targets. The analysis of the ($^3\text{He},d$) data benefited from the inclusion of ^{nat}C and ^{24}MgO targets in both determining background contributions and identifying individual states and any new (α,t) measurement should include these targets. Using a Mylar or another metallic oxide target may be useful for determining the effect of reactions on oxygen. This was the biggest source of uncertainty for the ($^3\text{He},d$) analysis and it is likely it will have a significant effect on any (α,t) analysis. Finally a reliable way must be found for calibrating the focal plane spectra. While SiO and ZnS targets were used for calibration purposes in this work they were not run for enough time to obtain sufficient statistics. A reliable way must be found in advance of a measurement to calibrate this spectra either using the (α,t) reaction or the (α,α') and (α,d) which are also found to be focussed on the focal plane. Accounting for these, a repeat measurement should be both successful and beneficial to the study $^{26}\text{Al}(n,p/\alpha)$ reaction rates.

Chapter 9

Conclusions and Future Work

In this thesis two experiments have been described using proton transfer reactions to study astrophysical reaction rates through indirect method. These have been discussed in the proceeding chapters and the main conclusions of this work will be summarised below.

The first experiment measured the $^{34}\text{S}(^3\text{He},\text{d})^{35}\text{Cl}$ reaction with the aim of reducing uncertainties in the $^{34}\text{S}(\text{p},\gamma)^{35}\text{Cl}$ reaction rate. With reduced uncertainties it was hoped the $^{32}\text{S}/^{34}\text{S}$ isotopic ratio could be used as a diagnostic tool to determine pre-solar grain paternity. A spectroscopic study of ^{35}Cl was performed identifying 10 new levels in the relevant energy region. Using these states a new reaction rate was calculated and an isotopic ratio of 82–95 was extracted for the case of an ONe novae. As present Type II supernova models predict a ratio of 18–38 it should be possible to distinguish between pre-solar grains from the two different events. There is ongoing work using this new isotopic ratio in conjunction with other common isotopic ratios $^{12}\text{C}/^{13}\text{C}$, $^{14}\text{N}/^{15}\text{N}$ and $^{29,30}\text{Si}/^{28}\text{Si}$ to identify a pre-solar grain from a classical nova.

The second experiment studied states in ^{27}Al relevant to the $^{26}\text{Al}(\text{n},\text{p}/\alpha)$. Two selective proton transfer reactions, $^{26}\text{Mg}(^3\text{He},\text{d})^{27}\text{Al}$ and $^{26}\text{Mg}(\alpha,\text{t})^{27}\text{Al}$, were used to identify low and high spin states above the neutron threshold. The resolution of the $(^3\text{He},\text{d})$ reaction was unable to resolve individual states, however it is possible to conclude that many of the known states appear to exhibit low spin behaviour. In addition there are 23 known states for which there is no direct comparison. Given the selectivity of the reaction this may indicate that they are high spin. Many difficulties

arose during the $^{26}\text{Mg}(\alpha,t)^{27}\text{Al}$ measurement which prevented the experimental aims from being met. Despite these difficulties a repeat of this measurement would be beneficial to the field. Fewer levels appear to be populated in this reaction and they are expected to be high spin states which may be important to the study of the $^{26}\text{Al}(n,p/\alpha)$ reaction rates. The problems studying this reaction have been identified and solutions given which would be useful if the measurement were to be repeated.

Appendix A

DWBA Calculations

In order to determine the validity of the DWBA calculations performed in this work, a replication study was performed. This study involved fitting previously published results with new DWBA calculations performed using FRESKO and comparing the results to the previous work. The results which were selected for replication was a study of states in ^{23}Na using the $^{22}\text{Ne}(^3\text{He},\text{d})$ reaction by Hale *et al.* The reasons for selecting this study were that the experiments used the same type of transfer reaction and were performed at the same beam energy, 20 MeV, with the reaction products analysed using a magnetic spectrometer. In addition both reactions involve the same isospin transfer and will populate levels in the sd and $f_{7/2}$ shells. The structure of this appendix is as follows: the parameters used in the optical model will be described and used in DWBA calculations to extract angular distributions which will be compared to the results from a previous study.

A.1 Optical Potential Parameters.

As was discussed in chapters 4 and 6 the DWBA calculations were performed using the FRESKO code with the global optical potentials of Liang *et al.* [83] and Daehnick *et al.* [85] for the ^3He and deuteron channels respectively. These potentials are calculated by fitting a large number of elastic scattering data sets to get a common set of parameters which can be used to create a complex optical potential $U(r)$. The

form of this potential was shown in eq. (2.11) and is presented again here:

$$\begin{aligned}
U(r) = & -V_r f_{ws}(r, R_0, a_0) - iW_v f_{ws}(r, R_w, a_w) \\
& -iW_s(-4a_w) \frac{d}{dr} f_{ws}(r, R_w, a_w) \\
& -2(V_{so} + iW_{so}) \left(-\frac{1}{r} \frac{d}{dr} f_{ws}(r, R_{so}, a_{so}) \right) \\
& +V_c.
\end{aligned} \tag{A.1}$$

Here V and W refer to real and imaginary potentials with R and a being the radius and diffuseness parameters of these potentials. The subscripts r, v, s, so and c refer to the real, volume, surface, spin orbit and Coulomb potentials respectively. For the ^3He optical potential of Liang *et al.* these parameters are extracted from the following relations:

$$\begin{aligned}
V_r = & V_0 + V_1 E_p + V_2 E_p^2 + V_3 \frac{(N_T - Z_T)}{A_T} + V_4 \frac{Z_T}{A_T^{1/3}}, \\
W_v = & W_{v0} + W_{v1} E_p + W_{v2} E_p^2, \\
W_s = & W_{s0} + W_{s1} E_p + W_{s2} \frac{(N_T - Z_T)}{A_T} + W_{s3} A_T^{1/3}, \\
V_{so} = & V_{so0} + V_{so1} A_T^{1/3}, \\
R_i = & r_i A_T^{1/3}, \\
r_i = & r_{i0} + r_{i1} A_T^{-1/3}, \\
a_i = & a_{i0} + a_{i1} A_T^{1/3}, \\
& (i = 0, v, s, so).
\end{aligned} \tag{A.2}$$

The parameters in the above equations have the same definitions as in eq. (A.1) with E_p being the projectile energy, and Z_T N_T and A_T being the number of proton, neutron and nucleons in the target nuclei. The numbered subscripts (0-4) refer to specific constants from the fits of elastic scattering data which can be found in [83]. For this set of optical potentials the imaginary volume and surface potentials have separate radius and diffuseness parameters opposed to eq. (A.1) which have common parameters r_w and a_w for both.

The global optical potentials for the deuterons interacting with the reaction product,

by Daehnick *et al.*, can be calculated from the following set of equations:

$$\begin{aligned}
V_r &= 88.5 - 0.26E_p + 0.88Z_T A_T^{-1/3}, \\
W_v &= (12.2 + 0.026E_p)(1 - e^\beta) \quad (\beta = (-E_p/100)^2), \\
W_s &= (12.2 + 0.026E_p)e^\beta \quad (\beta = (-E_p/100)^2), \\
V_{so} &= 7.33 - 0.029E_p, \\
R_i &= r_i A_T^{1/3}, \\
r_0 &= 1.17, \\
r_w &= 1.325, \\
r_{so} &= 1.07, \\
a_v &= 0.709 + 0.017E_p, \\
a_w &= 0.53 + 0.07A_T^{1/3} - 0.04 \sum_i e^{-\mu_i}, \\
a_{ls} &= 0.66.
\end{aligned} \tag{A.3}$$

The parameter μ_i in the definition of the imaginary diffuseness parameter a_w refers to the magic numbers ($\mu_i = 8, 20, 28, 50, 82, 126$).

A.2 $^{22}\text{Ne}(^3\text{He}, d)^{23}\text{Na}$ Angular distributions

Angular distributions were selected for five states seen in ^{23}Na which cover a 1 MeV energy region and involve multiple ℓ transfers. Other states were compared, but are not presented here. At each of these energies finite range DWBA calculations were performed using an optical potential calculated with eqs. (A.2) and (A.3). Data points were read from the published angular distributions and fit with the DWBA calculations. The results of these fits can be seen in Figure A.1 with the extracted spectroscopic factors summarised in Table A.1.

It can be seen in Figure A.1, that the comparison of the old and new calculations is good. The data matches the ℓ transfer assignments and shapes of the distribution look similar. Spectroscopic factors are not given directly in the paper, however the value $(2J_f+1)C^2S$ is and the agreement between these values and the present calculations, as seen in Table A.1 is good. With the exception of the 9252 keV state all values are in agreement within uncertainties. Differences in the distributions can be attributed to the fact the study by Hale *et al.* did not use a global potential

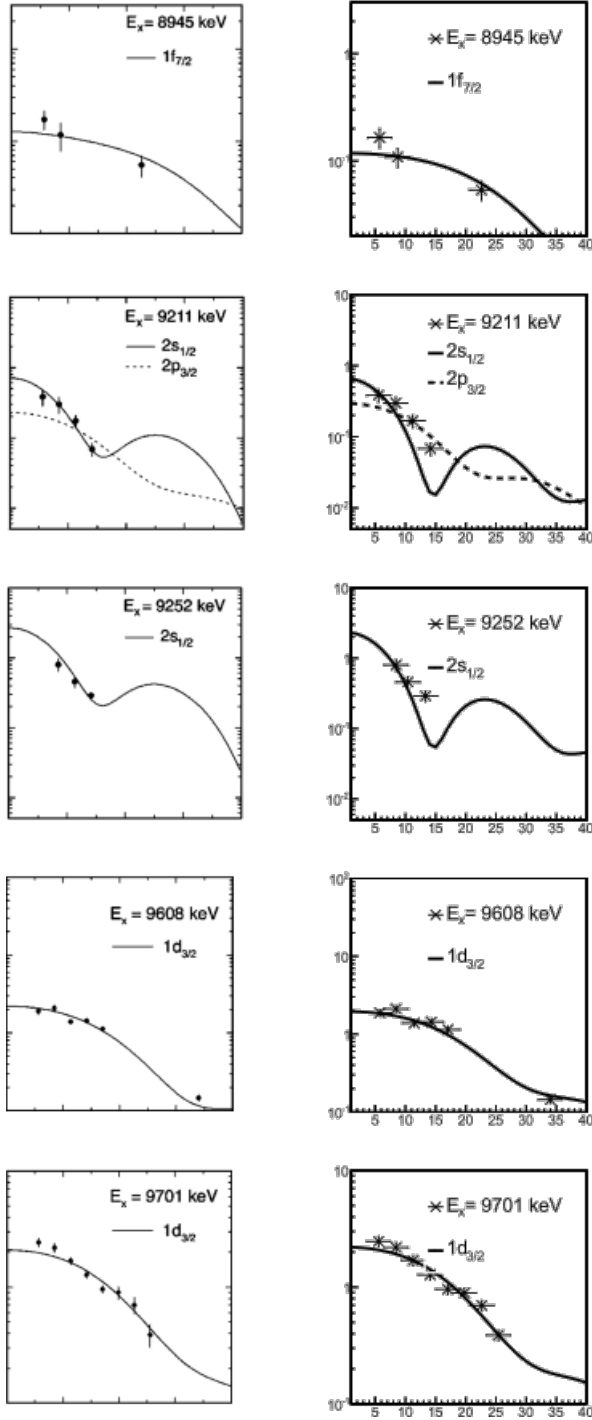


Figure A.1: Comparison of $^{22}\text{Ne}(^3\text{He},d)^{23}\text{Na}$ angular distribution fits. The distributions on the left of the figure are the fits from the previous study [86]. To the right are reproductions of the distributions fit with new calculations performed in this work. The extracted results are summarised in Table A.1.

Table A.1: Summary of DWBA fits and extracted spectroscopic factors. The information in this table are extracted from the angular distribution seen in Figure A.1. The fourth column shows the spectroscopic factors from the previous study [86] which can be compared with the results in the final column which were extracted calculations performed in this work.

E_x (keV)	J^π	ℓ	$(2J_f+1)C^2S$	
			Previous Work	This Work
8945	$7/2^-$	3	$\leq 8.7 \times 10^{-3}$	0.0076(7)
9211	$1/2^+$	0	0.02	0.018(4)
	$3/2^-$	1	3.9×10^{-3}	$5.2(8) \times 10^{-3}$
9252	$1/2^+$	0	0.079	0.065(6)
9608	$3/2^+$	2	0.082	0.079(5)
9701	$3/2^+$	2	0.084	0.089(6)

for the incoming channel. Parameters in their potential were modified to fit the measured $^{22}\text{Ne}(^3\text{He},^3\text{He})^3\text{He}$ elastic scattering data, which should provide a better fit to the data. Other differences could arise due to the different type of transfer coupling employed in the calculations. The present calculations were performed using finite range coupling, whereas the previous study used zero range coupling which then require an overall normalization factor to account for the finite range effects [103]. Despite this the comparison between this data is good enough to give confidence in the DWBA calculations performed in this work.

Appendix B

Example Calculations

B.1 Differential Cross Section Calculation

As discussed in chapters 4 and 6 parameters extracted from the focal plane fits are used to calculate angular distribution. In this section an example calculation will be performed, detailing how the fit parameters are used to calculate differential cross sections.

The differential cross sections for a transfer reaction is calculated using the equation;

$$\frac{d\sigma}{d\Omega_{CM}} = \frac{N_r}{I_B \cdot n_T \cdot d\Omega \cdot jac(\theta)}, \quad (\text{B.1})$$

where N_r is the number of reacted particles, I_B is the total integrated beam current, n_T is the number of target atoms per cm^2 and $d\Omega$ is the solid angle reacted particles are scattered into. The experimental cross sections are converted from the laboratory to the centre of mass frame using the Jacobian, $jac(\theta)$ which is given by;

$$jac(\theta) = \frac{[1 + 2\gamma \cdot \cos(\psi) + \gamma^2]^{3/2}}{1 + \gamma \cdot \cos(\psi)}, \quad (\text{B.2})$$

where ψ is the scattering angle in the centre of mass frame, which is related to the

Table B.1: Table of fit parameters for the 6.867 MeV state in ^{35}Cl at all angles. The fit parameters are for a landau function of the form seen in eq. (4.3).

A	A_{error}	μ	E_x	S	Integral
760681	13650	1059.74(20)	6867	-7.86(11)	$3.00(5)\times 10^6$
588358	14802	1061.85(20)	6866	-7.26(10)	$2.11(5)\times 10^6$
415761	8677	1059.44(2)	6866	-7.90(10)	$1.64(3)\times 10^6$
207160	4807	1053.56(3)	6866	-8.70(13)	$8.99(21)\times 10^5$
59608	2570	1046.1(6)	6867	-9.22(38)	$2.74(12)\times 10^5$

laboratory scattering angle with the expression;

$$\tan(\theta) = \frac{\sin(\psi)}{(\gamma + \cos(\psi))} \quad (\text{B.3})$$

$$\gamma = \left[\frac{M_A M_C}{M_B M_D} \right]^{1/2} \cdot \left(\frac{E_i}{E_f} \right).$$

$M_{A,B,C,D}$ is the mass of the beam and target particles before and after the reaction, E_i is the beam energy and E_f is the energy of the scattered particle.

Using these equations an example calculation will be for the 6.867 MeV state in ^{35}Cl . All reactions are performed using the $20 \mu\text{g}/\text{cm}^2$ Ag_2^{34}S target, $n_T = 3.79 \times 10^8$, where the deuterons are scattered into a solid angle of 5.33×10^{-3} sr. From the total spectrum fits the peak parameters for the 6.867 MeV peak are extracted and presented at all angles in Table B.1. Also shown in the table is the peak area from the integral of the peak function and the integral error calculated from the uncertainties in the fit parameters. The spectra which are fit in chapters 4 and 6 are normalised by the total integrated beam current so this integral is the charge normalised peak area, N_r/I_B in eq. (B.1). Using these integral values the differential cross sections are calculated at all angles and are given in Table B.2.

B.2 $\omega\gamma$ Calculation

The $^{34}\text{S}(p,\gamma)$ thermonuclear reaction rate is calculated assuming that the reaction rate proceeds through narrow resonances. This requires that the resonance strength $\omega\gamma$ must be calculated for each state which the reaction state can proceed through.

Table B.2: Experimental differential cross sections for the 6.867 MeV state in ^{35}Cl .

Q3D angle (θ)	$d\sigma/d\Omega$ (mb/sr)
5	1.25(2)
10	0.88(2)
15	0.68(2)
25	0.360(8)
40	0.115(5)

The resonance strength is calculated using eq. (2.25) which is presented here again for the $^{34}\text{S}(p,\gamma)$ reaction.

$$\omega\gamma = \frac{2J_r + 1}{(2J_p + 1)(2J_T + 1)} \frac{\Gamma_p \Gamma_\gamma}{\Gamma_{Tot}}. \quad (\text{B.4})$$

For a classical novae the $^{34}\text{S}(p,\gamma)$ reaction proceeds through narrow resonances within 600 keV of the proton threshold in ^{35}Cl . At this excitation energy it is assumed that the (p,γ) reaction channel is dominant so that $\Gamma_\gamma \gg \Gamma_p$. Using this assumption the expression in eq. (B.4) simplifies to;

$$\omega\gamma = \frac{2J_r + 1}{(2J_p + 1)(2J_T + 1)} \Gamma_p, \quad (\text{B.5})$$

where the proton partial width Γ_p is calculated using,

$$\Gamma_p = \frac{2\hbar^2}{\mu r^2} C^2 S P_\ell \theta_{sp}^2, \quad (\text{B.6})$$

The penetrability factors P_ℓ are calculated using the COULFG code [60], for specific angular momentum transfer values which are extracted from the DWBA fits of the angular distributions in section 4.4.3. The single particle reduced widths θ_{sp} have been previously calculated for specific orbitals in this region by Iliadis et al. [61]. In addition to the angular momentum transfer value the fit of the DWBA calculations to the angular distribution values allows for the extraction of the spectroscopic factor S . Finally the isospin Clebsch-Gordan coefficient C^2 is calculated to have a value of 2/3 for all states populated in the $^{34}\text{S}(p,\gamma)$ reaction.

An example of the $\omega\gamma$ calculation for the 6.842 MeV is presented here. For this state the angular distribution could be modelled as either an $\ell = 2$ or 3 transfer with

spectroscopic values $S = 0.0081(2)$ and $0.0066(2)$ respectively. These two values are used to calculate the minimum and maximum resonance strengths $\omega\gamma_{min}$ and $\omega\gamma_{max}$. The value of $\omega\gamma_{min}$ is calculated for an $\ell = 3$ transfer with $J = \ell + S$ coupling. Using these values the penetrability factor is calculated from the COULFG code [60] with a value

$$P_{\ell=3} = 1.89 \times 10^{-9}.$$

The transferred proton is placed in a $f_{7/2}$ orbital which has a single particle reduced width of

$$\theta_{sp} = 0.32.$$

Using these values with the reduced mass of the core+particle system, $\mu = 1.63 \times 10^{-27}$, the interaction radius, $r = 5.3$ fm and the spectroscopic factor $S = 0.0066(2)$ the proton partial width is calculated as,

$$\Gamma_p = 8.15 \times 10^{-6}.$$

Finally $J_T = 0^+$, $J_p = 1/2^+$ and $J_r = 7/2^-$, which are used with the proton partial width to calculate the resonance strength,

$$\omega\gamma_{min} = 3.3(1) \times 10^{-5} \text{ eV}.$$

Similarly the maximum resonance strength is calculated for an $\ell = 2$ transfer with $J = \ell - S$ coupling. For an $\ell = 2$ a spectroscopic factor of $0.0081(2)$ is extracted. Using these values the below partial widths and resonance strengths are calculated.

$$P_{\ell=2} = 5.91 \times 10^{-8},$$

$$\theta_{sp} = 0.36,$$

$$\Gamma_p = 3.48 \times 10^{-4}.$$

$$J_T = 0^+, J_p = 1/2^+ \text{ and } J_r = 3/2^+$$

$$\omega\gamma_{max} = 7.0(3) \times 10^{-4} \text{ eV}.$$

The values $\omega\gamma_{min}$ and $\omega\gamma_{max}$ are then used to calculate the minimum and maximum reaction rates.

Bibliography

- [1] C. Iliadis. *Nuclear Physics of Stars*. Wiley-VCH, 1st edition, 2007.
- [2] S. Chandrasekhar. *The Astrophysical Journal*, 74(1):81, 1931.
- [3] G. Hernández *et al.* *Nature*, 489:533–536, September 2012.
- [4] V. Schoenfelder *et al.* *The Astrophysical Journal Supplement Series*, 86:657–692, June 1993.
- [5] G. Vedrenne *et al.* *A&A*, 411(1):L63–L70, 2003.
- [6] C. Iliadis *et al.* *The Astrophysical Journal Supplement Series*, 142(1):105, 2002.
- [7] C. Iliadis *et al.* *The Astrophysical Journal Supplement Series*, 193(1):16, 2011.
- [8] A. Parikh *et al.* *The Astrophysical Journal Supplement Series*, 178(1):110, 2008.
- [9] B. Lazareff *et al.* *The Astrophysical Journal*, 228(1):875, 1931.
- [10] M. Hernanz J. José. *The Astrophysical Journal*, 494(2):680, 1998.
- [11] M. Hernanz J. José, A. Coc. *The Astrophysical Journal*, 560(2):897, 2001.
- [12] S. Starrfield *et al.* 296(3):502–522, 1998.
- [13] S. Starrfield *et al.* *The Astrophysical Journal*, 692(2):1532, 2009.
- [14] S. Amari *et al.* *The Astrophysical Journal*, 551(2):1065, 2001.
- [15] S. Amari. *New Astronomy Reviews*, 46(810):519 – 524, 2002. Proceedings of the International Workshop Astronomy with radioactivities {III}.
- [16] J. José *et al.* *The Astrophysical Journal*, 612(1):414, 2004.

- [17] P. Hoppe L. R. Nittler. *The Astrophysical Journal Letters*, 631(1):L89, 2005.
- [18] M. Hernanz J. José. *Meteoritics & Planetary Science*, 42(7-8):1135–1143, 2007.
- [19] The 75th annual meeting of the meteoritical society cairns, australia, 12-17 august, 2012. *Meteoritics & Planetary Science*, 47:A35–A436, 2012.
- [20] P. Hoppe, W. Fujiya, and E Zinner. *The Astrophysical Journal Letters*, 745(2):L26, 2012.
- [21] P. Hoppe *et al.* *The Astrophysical Journal*, 719(2):1370, 2010.
- [22] A. Parikh *et al.* *Physics Letters B*, 737:314 – 319, 2014.
- [23] M. Politano *et al.* *The Astrophysical Journal*, 448:807, August 1995.
- [24] S. Starrfield *et al.* *Nuclear Physics A*, 688(1):110 – 117, 2001.
- [25] M. Hernanz J. José, A. Coc. *The Astrophysical Journal*, 520(1):347, 1999.
- [26] C. Iliadis *et al.* *The Astrophysical Journal Supplement Series*, 134(1):151, 2001.
- [27] M. Limongi A. Chieffi. *The Astrophysical Journal*, 764(1):21, 2013.
- [28] J. D. Goss *et al.* *Phys. Rev. C*, 7:1871–1877, May 1973.
- [29] M.A. Meyer *et al.* *Nuclear Physics A*, 264(1):13 – 29, 1976.
- [30] P. Hubert *et al.* *Nuclear Physics A*, 195(2):485 – 501, 1972.
- [31] R. J. Sparks. *Nuclear Physics A*, 265(3):416 – 428, 1976.
- [32] D. W. Arnett. *Annals of the New York Academy of Sciences*, 302(1):90–100, 1977.
- [33] R. E. Lingenfelter R. Ramaty. *ApJL*, 213:L5–L7, April 1977.
- [34] W. A Mahoney *et al.* *ApJ*, 286:578–585, November 1984.
- [35] J. Knödseder. *The Astrophysical Journal*, 510(2):915, 1999.
- [36] J.-P. Roques L. Bouchet, E. Jourdain. *The Astrophysical Journal*, 801(2):142, 2015.
- [37] K. Kretschmer *et al.* *A&A*, 559:A99, 2013.

- [38] G. J. Wasserburg T. Lee, D. A. Papanastassiou. *Geophysical Research Letters*, 3(1):41–44, 1976.
- [39] F.M. Richter A.M. Davis. In *Treatise on Geochemistry*, pages 1 – 31. Pergamon, Oxford, 2007.
- [40] N. de Séréville V. Tatischeff, J. Duprat. *The Astrophysical Journal Letters*, 714(1):L26, 2010.
- [41] J.W. Truran A.G.W. Cameron. *Icarus*, 30(3):447 – 461, 1977.
- [42] A. Chieffi M. Limongi. *The Astrophysical Journal*, 647(1):483, 2006.
- [43] T. Rauscher and F.-K. Thielemann. *Atomic Data and Nuclear Data Tables*, 75(12):1 – 351, 2000.
- [44] C. N. Davids D. P. Whitmire. *Phys. Rev. C*, 9:996–1001, Mar 1974.
- [45] M.J.A. De Voigt *et al.* *Nuclear Physics A*, 170(3):449 – 466, 1971.
- [46] L. de Smet *et al.* *Phys. Rev. C*, 76:045804, Oct 2007.
- [47] S. Benamara *et al.* *Phys. Rev. C*, 89:065805, Jun 2014.
- [48] H.A. Enge J.E. Spencer. *Nuclear Instruments and Methods*, 49(2):181 – 193, 1967.
- [49] G. R. Satchler. *Introduction to Nuclear Reactions*. The Macmillan Press LTD, 1st edition, 1980.
- [50] G. R. Satchler. *Direct Nuclear Reactions*. Oxford University Press, 1st edition, 1986.
- [51] M. Born. *Zeitschrift für Physik*, 38(11):803–827.
- [52] J. P. Schiffer *et al.* *Phys. Rev. C*, 87:034306, Mar 2013.
- [53] I. J. Thompson. *Nuclear Reactions for Astrophysics*. Cambridge University Press, 1st edition, 2009.
- [54] F. Ajzenberg-Selove. *Nuclear Physics A*, 281(1):1 – 148, 1977.
- [55] P. E. Hodgson. *The Optical Model of Elastic Scattering*. Clarendon, Oxford, 1st edition, 1963.
- [56] M. B. Tsang *et al.* *Phys. Rev. Lett.*, 95:222501, Nov 2005.

- [57] J. Lee *et al.* *Phys. Rev. C*, 75:064320, Jun 2007.
- [58] I. J. Thompson. *Computer Physics Reports*, 7(4):167 – 212, 1988.
- [59] R. Longland *et al.* *Nuclear Physics A*, 841(1):1 – 30, 2010.
- [60] A. R. Barnett. *Computer Physics Communications*, 27(2):147 – 166, 1982.
- [61] C. Iliadis. *Nuclear Physics A*, 618(12):166 – 175, 1997.
- [62] L. Wolfenstein. *Phys. Rev.*, 82:690–696, Jun 1951.
- [63] H. Feshbach W. Hauser. *Phys. Rev.*, 87:366–373, Jul 1952.
- [64] K.-L. Kratz T. Rauscher, F.-K. Thielemann. *Phys. Rev. C*, 56:1613–1625, Sep 1997.
- [65] W. D. Myers *et al.* *Phys. Rev. C*, 15:2032–2043, Jun 1977.
- [66] M. Arnould. *Astron. Astrophys.*, 19:92, June 1972.
- [67] H. Vonach M. Lffler, H.J. Scheerer. *Nuclear Instruments and Methods*, 111(1):1 – 12, 1973.
- [68] C.A. Wiedner *et al.* *Nuclear Instruments and Methods*, 105(2):205 – 210, 1972.
- [69] Wikipedia. Quadrupole magnet — wikipedia, the free encyclopedia, 2014. [Online; accessed February 27, 2017].
- [70] F. T. Howard, editor. *Sector-focused cyclotrons: proceedings of an informal conference.*, Sea Island, Georgia, February 1959.
- [71] H.-F. Wirth. *Maier-Leibnitz-Laboratorium Annual Report*, page 71, 2000.
- [72] G. F. Knoll. *Radiation Detection and Measurement*. John Wiley and Sons, 4th edition, 2010.
- [73] M. A. Finlayson. *RCA Photomultiplier Manual. Technical Series PT-61*. RCA Solid State Division, Electro Optics and Devices, Lancaster,PA, 1970.
- [74] D. Visser. nukesim-classes: Java classes for nuclear physics simulation, 2014. [Online; accessed February 27, 2017].
- [75] R. A. Morrison. *Nuclear Physics A*, 140(1):97 – 117, 1970.
- [76] D. H. Youngblood R. L. Kozub. *Phys. Rev. C*, 5:413–419, Feb 1972.
- [77] P.M. Endt C. Van Der Leun. *Physica*, 24(6):1095 – 1101, 1958.

- [78] M. M. Aleonard *et al.* *Nuclear Physics A*, 257(3):490 – 516, 1976.
- [79] C. Iliadis *et al.* *Nuclear Physics A*, 539(1):97 – 111, 1992.
- [80] L. Landau. *J. Phys. J (USSR)*, 8:201, 1944.
- [81] D. Radford. Radware efficiency, 2013. [Online; accessed 18-April-2016].
- [82] J. E. Gaiser. *Harmonium Spectroscopy from Radiative Decays of the J/Psi and Psi-Prime*. PhD thesis, SLAC, 1982.
- [83] C.-H. Cai C.-T. Liang, X.-H. Li. *Journal of Physics G: Nuclear and Particle Physics*, 36(8):085104, 2009.
- [84] D. Y. Pang *et al.* *Phys. Rev. C*, 79:024615, Feb 2009.
- [85] Z. Vrcelj H. W. Daehnick, J. D. Childs. *Phys. Rev. C*, 21:2253–2274, Jun 1980.
- [86] S. E. Hale *et al.* *Phys. Rev. C*, 65:015801, Dec 2001.
- [87] G. Inghima *et al.* *Nuovo Cim.*, 26A:211, 1975.
- [88] C. Van Der Leun O.P. Van Pruissen, G.J.L. Nooren. *Nuclear Physics A*, 480(1):77 – 84, 1988.
- [89] P.M. Endt. *Nuclear Physics A*, 521:1 – 400, 1990.
- [90] M. Wang *et al.* *Chinese Physics C*, 36(12):1603, 2012.
- [91] A. L. Sallaska *et al.* *The Astrophysical Journal Supplement Series*, 207(1):18, 2013.
- [92] C. Iliadis *et al.* *Nuclear Physics A*, 841(1):31 – 250, 2010.
- [93] J. Casanova *et al.* *Nature*, 478:490, 2011.
- [94] J. José. *Private Communication*.
- [95] D. A. Hutcheon *et al.* *Nuclear Instruments and Methods A*, 498:190–210.
- [96] Anuj Parikh. *Private Communication*.
- [97] F. Ajzenberg-Selove. *Nuclear Physics A*, 523(1):1 – 196, 1991.
- [98] D. R. Tilley *et al.* *Nuclear Physics A*, 595(1):1 – 170, 1995.
- [99] J. Ziegler. Srim - the stopping and range of ions in matter, 2013. [Online; accessed February 27, 2017].

- [100] Nicolas de Séréville. *Private Communication*.
- [101] T. F. Wang *et al.* *Nuclear Physics A*, 499(3):546 – 564, 1989.
- [102] R. M. Prior *et al.* *Nuclear Physics A*, 533(3):411 – 427, 1991.
- [103] R. H. Bassel. *Phys. Rev.*, 149:791–797, Sep 1966.